EVALUATION OF METHODS FOR ESTIMATING THE CROSS-CORRELATION COEFFICIENT BETWEEN CLOSELY SPACED DIVERSITY ANTENNAS

by

Christopher Gareth Hynes

B.A.Sc., University of British Columbia, 2002

A THESIS SUBMITTED IN PARTIAL FULFILMENT OF
THE REQUIREMENTS FOR THE DEGREE OF

MASTER OF APPLIED SCIENCE

in

The Faculty of Graduate Studies

(Electrical and Computer Engineering)

THE UNIVERSITY OF BRITISH COLUMBIA

August 2007

Abstract

A growing number of cellular handsets and other personal wireless communications devices use diversity combining and/or MIMO techniques in order to boost link performance and reliability and therefore must incorporate closely spaced antennas. The cross-correlation coefficient between such antennas in fading environments is a key predictor of the success of such schemes. In recent years, several methods for predicting this parameter based upon measurement or simulation of either their field or terminal characteristics have been proposed. Here, we compare the performance of such methods for the case of two closely spaced half-wavelength dipole antennas subject to the assumptions that (1) the angle of arrival distribution is uniformly distributed in three-dimensions, (2) the polarization of the incident waves are uncorrelated to each other and individually uncorrelated in different directions and (3) the cross-polarization power ratio is unity. We consider two diversity antenna configurations. In the first, one antenna is loaded while the other is terminated by an open circuit, e.g., as in the case of switched diversity schemes. In the second, both antennas are attached to matched loads, e.g., as in the case of diversity combining or MIMO schemes. The best results were obtained using isolated far-field pattern coherence when one antenna is open-circuited and both antennas have characteristics approaching those of minimal scattering antennas. However, our results also indicate that the majority of recently proposed methods for estimating the cross-correlation coefficient are surprisingly inaccurate, especially when both antennas are attached to matched loads. Furthermore, we conclude that the total efficiency of the antennas is just as important as their cross-correlation in determining the performance of a multiple antenna system.

KEYWORDS: Antenna array mutual coupling, Antenna measurements, Antenna proximity factors, Correlation, Dipole antennas

Contents

List of Tables

List of Figures

List of Acronyms

BER bit-error-rate

CDMA Code Division Multiple Access

CMS Canonical Minimum Scattering

MEG Mean Effective Gain

MIMO Multiple-Input Multiple-Output

MPS Mobile Prototype Scenario

MS Minimum Scattering

TEM Transverse Electromagnetic

WSS Wide-Sense Stationary

XPR Cross-Polarization Power Ratio

List of Symbols

$\mathbf{a}$	S-parameter incidence vector
$(\cdot)^{\dagger}$	Adjoint operator, transpose and complex conjugation matrix operator
$\mathbf{b}$	S-parameter reflection vector
$\mathbf{C_e}$	Incident electric field mutual coherence matrix
$\mathbf{C_f}$	Isolated far-field pattern coherence matrix
$\mathbf{C_h}$	Antenna array coherence matrix
$\mathbf{C_L}$	Load voltage covariance matrix
$\mathbf{C_o}$	Open-circuit voltage covariance matrix
$D_\theta(\Omega)$	Directivity pattern of the theta component
$D_\phi(\Omega)$	Directivity pattern of the phi component
$\mathbf{e}$	Incident electric field vector
$\mathbb{E}[\cdot]$	Expectation operator
$\mathbf{f}$	Normalised isolated antenna effective height vector
k	Wavenumber
G_e	Mean Effective Gain
$\mathbf{h}$	Antenna effective height vector
$\mathbf{H}$	Array effective height matrix
j	$\sqrt{-1}$
(Ω)	Short-hand notation for the polar coordinates (θ, ϕ)
$d\Omega$	Element of solid angle
$\delta(\cdot)$	Dirac delta function
$P_\theta(\Omega)$	Incident power probability density of theta component
$P_\phi(\Omega)$	Incident power probability density of phi component
ρ_z	Complex correlation coefficient

ρ_r	Envelope correlation coefficient
ρ_{r^2}	Power correlation coefficient
ρ_{11}	Auto-correlation coefficient
ρ_{Lij}	Load voltage cross-correlation coefficient between elements i and j
ρ_{oij}	Open-circuit voltage cross-correlation coefficient between elements i and j
$\mathbf{S}$	N-port scattering wave representation scattering matrix
$(\cdot)^T$	Transpose matrix operator
$Tr(\cdot)$	Trace matrix operator
$\mathbf{V_o}$	Open-circuit voltage vector
Z	Intrinsic impedance of the medium (i.e. $\sqrt{\mu/\varepsilon}$)
Z_c	Characteristic impedance of a transmission line
$Z_{12}^{(e)}$	Correction term to the zero-order approximation term for the normalised mutual impedance
$Z_{12}^{(0)}$	Zero-order approximation term for the normalised mutual impedance

Acknowledgements

Firstly, I would like to thank my supervisor Professor David G. Michelson for his efforts in arranging the joint research project with Nokia, the financial support he provided during the research project, and the freedom he allowed me in pursuing a research topic. I would also like to thank the many others involved in arranging the joint Nokia/UBC research project; most notably the Nokia Hardware Line Manager, Cristian Tabacutu, for his support in publishing the research findings. I would like to thank Jari van Wonterghem for his advice during the course of the project and for his help in familiarizing me with the 3D pattern measurement system he created and which made the experimental measurement campaigns possible. I would like to thank Professor J. Romeu and Professor M. Jensen for their considerate and helpful email replies; Professor Rodney Vaughan for kindly taking the time to meet and discuss the specifics and the generalities of antenna theory; Jueren (Steven) Ma and Alizera (Nima) Manhanfar for their omnipresent willingness to discuss research or go for stress-relieving activities; my family for their support but most notably my mother for also her living example of perseverance and strength; and finally, my co-supervisor Dr.Ping Hui for his keen interest in the research that was pursued, his many recommendations, and his sage advice.

Chapter 1

Introduction

In recent years, personal wireless communications technology has evolved at an astonishing rate. This evolution has been facilitated by a miniaturization of integrated circuits which has allowed for devices with greater functionality and improved performance. From Bluetooth to GSM, the drive to support higher data rates and provide greater reliability have forced designers to incorporate various techniques to mitigate multipath effects. Multipath effects, which are typical phenomena when systems are deployed in high scattering environments, arise when the received signals are a superposition of multiple reflected waves. Such received signals usually suffer from inter-symbol interference and signal fading that can lead to severe degradations in system performance. Practical systems usually incorporate a combination of techniques to mitigate the multipath effects; for example, including both equalization and data coding techniques. Although some of these mitigative methods have become standard implementations on many types of wireless devices, further techniques continue to be sought after to further improve system performance in multipath environments.

Antenna diversity is a well-known technique for improving wireless system performance in multipath environments [1, 2]. Originally, antenna diversity was proposed for use in the receiving mobile device to combat signal fading. The concept of antenna diversity has been extended to both transmit and receive antennas and has culminated to Multiple-Input Multiple-Output (MIMO) systems [3–5]. MIMO systems have the potential to greatly improve performance without affecting spectrum efficiency. Information-theoretic results [3] for independent channel paths indicate that capacity: (1) saturates at some finite limit when the number of transmit antennas is increased; (2) grows logarithmically when the number of receive antennas is increased; and (3) grows linearly when the number of transmit and receive antennas are increased in proportion.

The diversity gain is a function of the correlation and relative signal-to-noise ratio of the sig-

nal branches. It is intuitive that if the branches are highly correlated then deep signal fades have a higher probability of occurring simultaneously on all the branches; thus decreasing the diversity gain. However, a well known surprising result is that the diversity gain is high even with highly correlated signals. For example [2], for Rayleigh fading (special case of Nakagami-m distribution when m=1) using selection diversity with two equal mean branches, one finds the combined signal to be 9.3dB better 98% of the time with uncorrelated signals and 6.3dB for signals with 80% correlation.

The effect of correlated fading on the performance of a diversity combining receiver continues to have a great deal of research interest. For example, closed-form expressions were recently obtained for the error probability for arbitrary diversity order Nakagami fading channels with general branch correlations and average signal-to-noise ratio imbalances [6–8]. So given the branch correlations and average signal-to-noise ratios one can predict the diversity gain.

Traditionally, antenna diversity has only been deployed on the base-station side of the communication link. Although studies have shown that low branch correlations are fairly easy to obtain in designs featuring closely spaced diversity antennas [9–19], designers have hesitated to implement mobile diversity for many reasons; including the increase in design complexity and increased in cost for an uncertain improvement in performance. Because multiple antenna systems address the problems caused by multipath fading directly without affecting spectrum efficiency, it is inevitable that such technology will be incorporated into wireless devices that support high data rates in multipath environments. Some Wireless LAN and Bluetooth devices have incorporated diversity antennas from their initial designs. With the release of the 3GPP (third generation partnership project) WCDMA and CDMA 2000 standards, designers are now encouraged to incorporate antenna diversity into handsets [20, 21].

Traditionally, the cross-correlation coefficients between multiple antennas were determined by actual field measurements [2], i.e., take prototype designs in the field, measure time-series data, and then determine the cross-correlation coefficient. To avoid these arduous measurement campaigns, a theoretical method was developed to estimate the cross-correlations based on assumed incident-field distributions and antenna patterns [22, 23]. However, such a method still requires detailed amplitude and phase measurements of three-dimensional antenna patterns, and is therefore time-consuming and limited to designers that have access to the necessary antenna pattern measure-

ment facilities.

In order to further reduce the time and equipment required to predict the correlation coefficients, researchers have assumed stringent conditions on the incident field distribution in order to obtain estimates from circuit parameters alone [23–25]. These circuit parameter estimates are derived assuming an incident field distribution such that: (1) the angle of arrival distribution is uniformly distributed in three-dimensions, (2) the polarization of the incident waves are uncorrelated to each other and individually uncorrelated in different directions and (3) the cross-polarization power ratio is unity. Under these incident field assumptions, the cross-correlation can be expressed as the functional dot-product of the complex antenna patterns alone. From this expression, the two circuit parameter estimates have been formulated: (1) it was shown that this should be roughly equal to the normalized mutual resistance for antennas that approximate Minimal Scattering antennas [23] and (2) based on energy conservation principles a S-parameter estimate can be derived [24,25]. The original S-parameter estimate formulation was limited to lossless perfectly matched antennas [24]. The S-parameter estimate was then generalised [25] but the assumed expression for the total far-field electric field in terms of antenna far-field patterns seemingly does not agree with scattering theory [26].

The circuit parameter methods to estimate the correlation are attractive since they could be determined by a single terminal measurement on a network analyzer. As this could allow for fast and efficient evaluation of potential designs, the circuit parameter estimates are becoming commonly used by antenna designers. However, apparently no comparison studies have been performed to evaluate and compare their accuracy.

In this thesis, we compare and evaluate known methods for estimating the cross-correlation coefficient between closely spaced diversity antennas through numerical simulations and experimental measurements for the case of two parallel non-staggered dipoles. To obtain the simulation results, we used CST Microwave Studio, a well-known simulation tool that is based upon the Finite Integration Technique (FIT), a consistent formulation for the discrete representation of Maxwell's equations on numeric grids. To obtain the experimental results, we measured the responses of two balanced sleeve dipoles (manufactured by Satimo) within a 3-D anechoic chamber built in-house at Nokia. We compared and evaluated the estimates for the cross-correlation coefficient for the two common deployment scenarios of when the parasitic element is either open-circuited or 50-ohm

termination. Additionally, for the case when the parasitic element is terminated by 50 ohms, we performed a relative comparison between the radiation efficiency and the cross-correlation coefficient.

The remainder of this thesis is organized as follows.

In Chapter Two, we summarize the mathematical methods used to characterize incident fields and receiving antenna.

In Chapter Three, we investigate the cross-correlation coefficient estimates between switch diversity antennas based on numerical simulations. We show that only one of the estimates is accurate for the case when the antennas scattering characteristics are approximately those of Minimum Scattering (MS) antennas. We then provide closed formed expressions for the cross-correlation estimates between collinear parallel dipoles of arbitrary lengths.

In Chapter Four, we investigate the cross-correlation coefficient estimates between load-terminated antennas based on numerical simulations and experimental pattern measurements within an anechoic chamber. The results again indicated that only one of the estimates is accurate for the case when the antennas scattering characteristics approached those of MS antennas. The circuit-parameter estimates were found to poorly match the theoretical value and trend well only when the antennas approached MS. Finally, we compared the antenna total efficiencies and correlation coefficients for both the numerical simulations and the experimental results.

In Chapter Five, we summarize the major conclusions of this thesis and give recommendations for future work.

Supplementary information is presented in twelve appendices.

In Appendix A, we show the standard spherical coordinate system used throughout this thesis.

In Appendix B, we derive the relationship between transmit and receive antenna patterns near metallic scatterers. The reciprocity relation is often implicitly assumed and this appendix gives a proof and outlines the necessary assumptions.

In Appendix C, we derive the relationships between the cross-correlation coefficient of narrowband signals to their complex baseband, power, and the envelope signals. The envelope cross-correlation coefficient is often used when measuring the cross-correlation coefficient and it's important to note that it is an approximation to the signal cross-correlations.

In Appendix D, we outline the CST Microwave Studio simulation settings and show samples

of antenna models used for the numerical simulations.

In Appendix E, we give the self and mutual resistances, as a function of separation distance, for the simulated cylindrical dipoles.

In Appendix F, we show the matching and coupling frequency off-set extremes over the range of separation distances simulated.

In Appendix G, we show the equivalence of the circuit-parameter estimates based on numerical simulations and experimental measurements.

In Appendix H, we present results for correlation estimates for two different frequencies. These results show the high sensitivity of the circuit-parameter based estimates relative to the theoretical value.

In Appendix I, we evaluate the auto-correlation integral for a Hertzian dipole.

In Appendix J, we show the experimental set-up, in the anechoic chamber, of the Satimo sleeve dipoles when obtaining the S-parameters and antenna pattern measurements.

In Appendix K, we give the measured self and mutual resistances, as a function of separation distance, of the Satimo sleeve dipoles.

Finally, in Appendix L, we show the numerical simulation results for the H-plane antenna pattern variation, as a function of separation distance, for two closely spaced dipoles.

Chapter 2

Characterization of Incident Fields and Antennas

2.1 Introduction

In this chapter we describe some necessary background material related to the characterizations of incident field distributions and antenna arrays. These concepts and mathematical notations will be used in the following chapters when formulating the estimates for the cross-correlation coefficients between antenna elements. The chapter begins by characterizing incident field distributions and antenna arrays. We then present a brief summary of the network representation of antenna arrays and the concept of Minimal Scattering Antennas. Finally, we present expressions for the coupling between Minimal Scattering Antennas and the Mean Effective Gain.

This thesis uses the standard spherical coordinate system as specified in the IEEE standard test procedures for antennas [27]; as shown in Appendix A. For brevity we shall represent the spherical coordinates (θ, ϕ) by the symbol (Ω). All random processes are assumed to be ergodic, i.e., that ensemble averages can be replaced by time averages. Physical vectors will be denoted by lower case bold, e.g. $\mathbf{e}$, and matrices be upper-case bold, e.g. $\mathbf{S}$. Throughout this document we assume the voltage signals have been demeaned.

2.2 Characterization of Incident Fields

In order to estimate the signals received on an antenna it is necessary to characterize the incident field from distributed sources. In the following sections the incident field characterizations for narrowband signals will be presented for three cases: (1) the general case; (2) a simplified case using commonly used assumptions on the incident fields; and (3) the canonical case using very

stringent incident field assumptions. This last case uses appropriate assumptions for mobile devices in high scattering environments and forms the basis for all the estimation methods presented in this thesis.

2.2.1 Radiation from distributed sources

Partially polarized narrowband polychromatic electric fields from distributed sources can be characterized in terms of a mutual coherence matrix [22]. We will denote the incident electric field from sources at the direction Ω subtending a solid angle $d\Omega$ as $\mathbf{e}(\Omega, t)d\Omega$, where

$$\mathbf{e}(\Omega, t) = [E_\theta(\Omega, t) \quad E_\phi(\Omega, t)] \quad . \tag{2.1}$$

Thus, the physical vector $\mathbf{e}(\Omega, t)$ will be denoted as a row vector where the first and second column elements are the θ and ϕ polarizations components, respectively. The incident field mutual coherence matrix, $\mathbf{C_e}$, is defined as,

$$\begin{aligned}
\mathbf{C_e}(\Omega_1, \Omega_2) =& \mathbb{E}[\mathbf{e}(\Omega_1, t)^T \mathbf{e}(\Omega_2, t)^*] && (2.2)\\
=& \begin{bmatrix} \mathbb{E}[E_\theta(\Omega_1, t)E_\theta^*(\Omega_2, t)] & \mathbb{E}[E_\theta(\Omega_1, t)E_\phi^*(\Omega_2, t)] \\ \mathbb{E}[E_\phi(\Omega_1, t)E_\theta^*(\Omega_2, t)] & \mathbb{E}[E_\phi(\Omega_1, t)E_\phi^*(\Omega_2, t)] \end{bmatrix} && (2.3)\\
=& \begin{bmatrix} \mathbf{C_e}^{\theta\theta} & \mathbf{C_e}^{\theta\phi} \\ \mathbf{C_e}^{\phi\theta} & \mathbf{C_e}^{\phi\phi} \end{bmatrix} && (2.4)
\end{aligned}$$

where ^{T} is the transpose operator, * is the complex conjugate operator, and $\mathbb{E}[\cdot]$ is the expectation operator with respect to time.

2.2.2 Simplifying assumptions for incident fields

If the θ and ϕ field polarizations are uncorrelated, and are individually uncorrelated in different angular directions, then the mutual coherence matrix becomes a diagonal matrix given by,

$$\mathbf{C_e}(\Omega_1, \Omega_2) = \bar{P}_\phi \delta(\Omega_1 - \Omega_2) \begin{bmatrix} \text{XPR}\, P_\theta(\Omega_1) & 0 \\ 0 & P_\phi(\Omega_1) \end{bmatrix} \tag{2.5}$$

where $\mathbb{E}[|E_\theta(\Omega,t)|^2] = \bar{P}_\theta P_\theta(\Omega)$, $\mathbb{E}[|E_\phi(\Omega,t)|^2] = \bar{P}_\phi P_\phi(\Omega)$, $\bar{P}_\theta$ and $\bar{P}_\phi$ are proportional to the average power in the θ and ϕ component of the incident field, respectively, $P_\theta(\Omega)$ and $P_\phi(\Omega)$ are the θ and ϕ solid angle incident power probability densities, respectively, XPR$= \bar{P}_\theta/\bar{P}_\phi$ is the Cross-Polarization Power Ratio (XPR), and $\delta(\cdot)$ is the Dirac delta function.

Studies have shown that measured values for the XPR typically show large variations between -6 dB and 18 dB and is a function of the surrounding environment, separation distances, and relative polarizations of the transmit and receive antennas [2, 28–33]. For suburban outdoor environments [2] and indoor environments [29], where there is no direct line-of-sight between the transmitter and receiver, measurements indicate that the XPR is typically 0 dB. However, in urban outdoor environments and in areas where there is a strong line-of-sight signal, the XPR has been found to be in the range of 4-9 dB [30, 31, 33].

The probability distributions of incident power have been well modeled by a uniform distributions in the ϕ variable and Gaussian distributions in the θ variable [30],

$$P_\theta(\theta,\phi) = N_\theta \exp[-(\theta - \pi/2 + m_\theta)^2/2\sigma_\theta^2] \tag{2.6}$$

$$P_\phi(\theta,\phi) = N_\phi \exp[-(\theta - \pi/2 + m_\phi)^2/2\sigma_\phi^2] \tag{2.7}$$

where m_i, σ_i, and N_i are the mean, standard deviation, and is the normalization constant of the ith component respectively. Typical values for m_i and σ_i in urban outdoor environments are [30, 34] $m_\theta = 19^o$, $\sigma_\theta = 20^o$, $m_\phi = 32^o$, and $\sigma_\phi = 64^o$. Whereas for indoor non-line-of-sight environments typical values of $m_\theta = 0^o$, $\sigma_\theta = 27^o$, $m_\phi = 0^o$, and $\sigma_\phi = 58^o$ have been measured.

2.2.3 Incident field approximation suitable for prototype development

To develop mobile devices that utilize a form of antenna diversity it is critical that fast and efficient methods be available to evaluate the potential designs. A reasonable assumption for mobile scenarios is that the incident angular power density, for both polarizations, is given by the 3D uniform distribution $P_\theta(\Omega) = P_\theta(\Omega) = 1/4\pi$. The incident fields in dense urban areas or indoor environments can be well approximated by the 3D uniform distribution since the orientation of the mobile device will change frequently as the user adjusts the device's position, thereby leading to typically large standard deviations in Eqn. (2.6) and (2.7).

If, additionally, the XPR is unity, this incident field scenario is defined as the Mobile Prototype Scenario and the mutual coherence matrix reduces to,

$$\mathbf{C_e}(\Omega_1, \Omega_2) = P\delta(\Omega_1 - \Omega_2) \tag{2.8}$$

where P is proportional to the average incident power.

2.3 Characterization of Antennas

This section will outline some of the relationships between antenna array field quantities and measurable antenna circuit parameters. These relationships are used in the formulation of the estimates for the cross-correlation coefficient in terms of measurable antenna circuit parameters. It will be assumed that the antenna noise is negligible compared to the receiver noise and will be neglected.

2.3.1 Antenna effective height vector

The effective antenna height vector [22, 35], $\mathbf{h}(\Omega) = [h_\theta(\Omega) \quad h_\phi(\Omega)]$, is defined from the open circuit voltage, V_o, on a receiving antenna from an incident plane wave by the relation,

$$V_o = \mathbf{h}(\Omega)\mathbf{e}_i(\Omega)^T \tag{2.9}$$

where $\mathbf{e}_i$ (see (2.1)) is the electric field at the origin from a plane wave incident from the direction (Ω) and ^{T} denotes the matrix transpose operator. For an N element antenna array, (2.9) can be expressed in matrix form as,

$$\mathbf{V_o} = \mathbf{H}(\Omega)\mathbf{e}_i(\Omega)^T \tag{2.10}$$

where $\mathbf{V_o} = [V_{o1} \cdots V_{0N}]^T$ is the vector of open-circuit voltages, and

$$\mathbf{H}(\Omega) = [\mathbf{h}_1(\Omega) \cdots \mathbf{h}_N(\Omega)]^T \tag{2.11}$$

is the array effective height matrix which is a $N \times 2$ matrix whose j^{th} row contains the jth antenna effective height vector with respect to a common co-ordinate system. For cases of distributed sources, the open circuit voltages is expressed in terms of the effective antenna height vectors

as [22],

$$\mathbf{V_o}(t) = \oint \mathbf{H}(\Omega)\mathbf{e}_i(\Omega, t)^T \, d\Omega \tag{2.12}$$

where $\mathbf{e}_i$ is the source vector, $\mathbf{H}$ is given by (2.11), and $d\Omega = \sin\theta \, d\theta d\phi$.

2.3.2 Far-field transmission pattern

As shown in Appendix B, the far-field electric field pattern can be represented in terms of the effective antenna height vector as,

$$\mathbf{e}(\mathrm{r}) = \frac{jZkI_{in}e^{-jkr}}{4\pi r}\mathbf{h}(\Omega) \qquad \text{as } r \rightarrow \infty \tag{2.13}$$

where I_{in} is the input current to the antenna, r is the observation point in spherical coordinates (r, θ, ϕ) with respect to the origin at the antenna, $k = 2\pi/\lambda$ is the wavenumber, and $Z = \sqrt{\mu/\epsilon}$ is the intrinsic wave impedance of the medium. This relationship is proven for the case when the antenna is radiating near metallic scatters in an unbounded isotropic homogeneous medium characterized by the constitutive parameters (ϵ, μ). It is also assumed the antenna is fed from a generator which is matched to the transmission line.

2.3.3 Antenna array coherence matrix

The expressions for the correlation between antenna arrays elements can be succinctly characterized by the use of an antenna array coherence matrix. For a N element array we define a $2N \times 2N$ antenna array coherence matrix as,

$$\mathbf{C_h}(\Omega_1, \Omega_2) = \begin{bmatrix} \mathbf{C_h}^{\theta\theta} & \mathbf{C_h}^{\theta\phi} \\ \mathbf{C_h}^{\phi\theta} & \mathbf{C_h}^{\phi\phi} \end{bmatrix} \tag{2.14}$$

where,

$$\mathbf{C_h}^{\theta\theta}(\Omega_1,\Omega_2) = \mathbf{h}_\theta(\Omega_1)\mathbf{h}_\theta^\dagger(\Omega_2) \tag{2.15}$$

$$\mathbf{C_h}^{\theta\phi}(\Omega_1,\Omega_2) = \mathbf{h}_\theta(\Omega_1)\mathbf{h}_\phi^\dagger(\Omega_2) \tag{2.16}$$

$$\mathbf{C_h}^{\phi\theta}(\Omega_1,\Omega_2) = \mathbf{h}_\phi(\Omega_1)\mathbf{h}_\theta^\dagger(\Omega_2) \tag{2.17}$$

$$\mathbf{C_h}^{\phi\phi}(\Omega_1,\Omega_2) = \mathbf{h}_\phi(\Omega_1)\mathbf{h}_\phi^\dagger(\Omega_2) \quad . \tag{2.18}$$

$\mathbf{C_h}^{\theta\theta}$, $\mathbf{C_h}^{\theta\phi}$, $\mathbf{C_h}^{\phi\theta}$, and $\mathbf{C_h}^{\phi\phi}$ are $N \times N$ matrices called the theta, theta-phi, phi-theta, and phi component antenna array coherence matrix, respectively. The $N \times 1$ column vectors $\mathbf{h}_\theta$ and $\mathbf{h}_\phi$ are the θ and ϕ vector components of the effective heights; i.e. are the first and second columns, respectively, of (2.11). It should be noted that the effective antenna heights are with respect to a common coordinate system. As an example, the antenna array coherence matrix for an array with two antenna elements is given by,

$$\mathbf{C_h}(\Omega_1,\Omega_2) = \begin{bmatrix} \mathbf{C_h}^{\theta\theta} & \mathbf{C_h}^{\theta\phi} \\ \mathbf{C_h}^{\phi\theta} & \mathbf{C_h}^{\phi\phi} \end{bmatrix}$$

$$= \left[\begin{array}{cc|cc} h_{\theta1}(\Omega_1)h_{\theta1}^*(\Omega_2) & h_{\theta1}(\Omega_1)h_{\theta2}^*(\Omega_2) & h_{\theta1}(\Omega_1)h_{\phi1}^*(\Omega_2) & h_{\theta1}(\Omega_1)h_{\phi2}^*(\Omega_2) \\ h_{\theta2}(\Omega_1)h_{\theta1}^*(\Omega_2) & h_{\theta2}(\Omega_1)h_{\theta2}^*(\Omega_2) & h_{\theta2}(\Omega_1)h_{\phi1}^*(\Omega_2) & h_{\theta2}(\Omega_1)h_{\phi2}^*(\Omega_2) \\ \hline h_{\phi1}(\Omega_1)h_{\theta1}^*(\Omega_2) & h_{\phi1}(\Omega_1)h_{\theta2}^*(\Omega_2) & h_{\phi1}(\Omega_1)h_{\phi1}^*(\Omega_2) & h_{\phi1}(\Omega_1)h_{\phi2}^*(\Omega_2) \\ h_{\phi2}(\Omega_1)h_{\theta1}^*(\Omega_2) & h_{\phi2}(\Omega_1)h_{\theta2}^*(\Omega_2) & h_{\phi2}(\Omega_1)h_{\phi1}^*(\Omega_2) & h_{\phi2}(\Omega_1)h_{\phi2}^*(\Omega_2) \end{array}\right]$$

where * is the complex conjugate operator, and $h_{\theta i}$ and $h_{\phi i}$ are the theta and phi components of the effective antenna height vectors.

For an N element antenna array, a useful approximation of the antenna array coherence matrix is given by the isolated far-field pattern coherence matrix,

$$\mathbf{C_f}(\Omega_1,\Omega_2) = \begin{bmatrix} \mathbf{C_f}^{\theta\theta} & \mathbf{C_f}^{\theta\phi} \\ \mathbf{C_f}^{\phi\theta} & \mathbf{C_f}^{\phi\phi} \end{bmatrix} \tag{2.19}$$

where,

$$\mathbf{C_f}^{\theta\theta}(\Omega_1,\Omega_2) = \mathbf{f}_\theta(\Omega_1)\mathbf{f}_\theta^\dagger(\Omega_2) \tag{2.20}$$

$$\mathbf{C_f}^{\theta\phi}(\Omega_1,\Omega_2) = \mathbf{f}_\theta(\Omega_1)\mathbf{f}_\phi^\dagger(\Omega_2) \tag{2.21}$$

$$\mathbf{C_f}^{\phi\theta}(\Omega_1,\Omega_2) = \mathbf{f}_\phi(\Omega_1)\mathbf{f}_\theta^\dagger(\Omega_2) \tag{2.22}$$

$$\mathbf{C_f}^{\phi\phi}(\Omega_1,\Omega_2) = \mathbf{f}_\phi(\Omega_1)\mathbf{f}_\phi^\dagger(\Omega_2) \quad . \tag{2.23}$$

$\mathbf{C_f}^{\theta\theta}$, $\mathbf{C_f}^{\theta\phi}$, $\mathbf{C_f}^{\phi\theta}$, and $\mathbf{C_f}^{\phi\phi}$ are $N \times N$ matrices called the theta, theta-phi, phi-theta, and phi component isolated far-field pattern coherence matrix, respectively. The $N \times 1$ column vectors $\mathbf{f}_\theta$ and $\mathbf{f}_\phi$ are the vectors of the theta and phi components respectively of the isolated far-field patterns and are normalized such that,

$$\oint |\mathbf{f}|^2 \, d\Omega = 1 \quad . \tag{2.24}$$

Again, it should be noted that the isolated far-field patterns are with respect to a common coordinate system. The difference between an antenna array's coherence matrix and isolated far-field pattern coherence matrix is that the former includes the effects of scattering and mutual coupling between the antenna elements; whereas the latter excludes them. Throughout this thesis the antenna's effective height vector, $\mathbf{h}$, is differentiated symbolically from the normalized isolated effective height vector $\mathbf{f}$.

2.3.4 Network representation of antennas

The representation of a linear antenna-system with respect to N local ports and an infinite set of ports of spherical vector mode functions outside some sphere enclosing the antenna-system can be described by a scattering matrix [36–39],

$$\mathbf{b} = \mathbf{S}\mathbf{a} = \begin{bmatrix} \mathbf{b}_\alpha \\ \mathbf{b}_\beta \end{bmatrix} = \begin{bmatrix} \mathbf{S}_{\alpha\alpha} & \mathbf{S}_{\alpha\beta} \\ \mathbf{S}_{\beta\alpha} & \mathbf{S}_{\beta\beta} \end{bmatrix} \begin{bmatrix} \mathbf{a}_\alpha \\ \mathbf{a}_\beta \end{bmatrix} \tag{2.25}$$

where $\mathbf{a}_\alpha$ and $\mathbf{b}_\alpha$ are $N \times 1$ column vectors each containing, respectively, the incident and reflected waves at the N local accessible antenna ports. Similarly, $\mathbf{a}_\beta$ and $\mathbf{b}_\beta$ are infinite-dimensional column vectors denoting incident and reflected wave amplitudes of the spherical modes. The N dimensional

submatrix $\mathbf{S}_{\alpha\alpha}$ describes the mutual coupling among the accessible antenna ports, while $\mathbf{S}_{\alpha\beta}$, $\mathbf{S}_{\beta\alpha}$, and $\mathbf{S}_{\beta\beta}$ describe, respectively, the receiving, transmitting, and scattering properties of the antenna. For example, an incident wave $\mathbf{a}_\alpha$ at the local antenna ports produces the radiated wave $\mathbf{b}_\beta = \mathbf{S}_{\beta\alpha}\mathbf{a}_\alpha$ and a reflected wave $\mathbf{b}_\alpha = \mathbf{S}_{\alpha\alpha}\mathbf{a}_\alpha$ back into the antenna ports. If the N local ports are all connected to matched loads then $\mathbf{a}_\alpha = 0$ and an incident wave $\mathbf{a}_\beta$ produces a wave $\mathbf{b}_\alpha = \mathbf{S}_{\alpha\beta}\mathbf{a}_\beta$ at the antenna ports and causes a wave $\mathbf{b}_\beta = \mathbf{S}_{\beta\beta}\mathbf{a}_\beta$ to be reflected into the surrounding space. The representation (2.25) only holds for lossless antennas and thus $\mathbf{S}$ must be unitary,

$$\mathbf{S}^\dagger\mathbf{S} = \mathbf{I} \tag{2.26}$$

where $\mathbf{I}$ is the identity matrix, and † is the adjoint operator. The open-circuit impedance matrix representation, Za, at the antenna ports is related to the S-parameter matrix $\mathbf{S}_{\alpha\alpha}$ by the relation [40],

$$\mathbf{Z_a} = Z_c(\mathbf{I} - \mathbf{S}_{\alpha\alpha})^{-1}(\mathbf{I} + \mathbf{S}_{\alpha\alpha}) \tag{2.27}$$

where Z_c is the normalization impedance (usually taken as the characteristic impedance of the feed transmission line.) The voltage on and current into the nth port is given by,

$$v_n = \sqrt{Z_c}(a_n + b_n) \tag{2.28}$$

$$i_n = \frac{1}{\sqrt{Z_c}}(a_n - b_n) \tag{2.29}$$

where Z_c is the characteristic impedance of the transmission line.

2.3.4.1 Minimal scattering antennas

Minimum Scattering antennas have the property that when terminated by an appropriate reactance they do not scatter an impinging incident wave, i.e. they become electromagnetically invisible [36–39]. If the required reactance is infinite (open-circuited) then the Minimum Scattering antenna is referred to as Canonical Minimum Scattering (CMS) antenna. Minimum Scattering (MS) antennas have many tractable properties: they are lossless antennas that maximize the amount of power absorbed relative to the power scattered, when terminated in a perfectly matched load the scattered power and absorbed power are identical, for appropriate termination reactance the scattered fields

are identical to their radiated fields, and if the antenna is reciprocal the power pattern is symmetric in any plane through the origin. Most single mode antennas are approximately MS antennas [41].

2.3.5 Mutual coupling between Minimum Scattering antennas

Scattering and mutual coupling properties of arrays composed of MS antennas have been studied by Wasylkiwskyj and Kahn [42–44]. As shown in [42], the open-circuit impedance matrix parameters Z_{11}, $Z_{12} = Z_{21}$, and Z_{22} for two reciprocal antennas can be expressed as,

$$\frac{Z_{11}}{Z_1} = 1 + Z_{11}^{(e)} \tag{2.30}$$

$$\frac{Z_{22}}{Z_2} = 1 + Z_{22}^{(e)} \tag{2.31}$$

$$\frac{Z_{12}}{\sqrt{R_1 R_2}} = \frac{Z_{21}}{\sqrt{R_1 R_2}} = Z_{12}^{(0)} + Z_{12}^{(e)} \tag{2.32}$$

where Z_1, and Z_2 are the input impedances of antenna 1 and 2, respectively, when isolated in free-space, $R_1 = \text{real}\{Z_1\}$, $R_2 = \text{real}\{Z_2\}$. The normalized mutual impedance in (2.32) is comprised of the zeroth-order approximation $Z_{12}^{(0)}$ and a correction term $Z_{12}^{(e)}$ that depends on the radiation and scattering properties of the antennas. The zeroth-order approximation term can be computed from the knowledge of the radiation fields of the two antennas when isolated in space [43],

$$Z_{12}^{(0)} = 2 \int_{\phi=0}^{2\pi} \int_C \mathbf{f}_1(\theta, \phi) \hat{\mathbf{f}}_2^T(\theta, \phi) e^{j\mathbf{k}\cdot\mathbf{d}} \sin\theta \, d\theta d\phi \tag{2.33}$$

where the path C for θ is from $-\pi/2 - j\infty$ to $\pi/2 + j\infty$ in the complex θ plane, $\mathbf{k}$ is the incident wave number vector, and $\mathbf{d}$ is the vector from antenna element 1 to antenna element 2. The $\hat{}$ operator appearing in (2.33) is the vector co-ordinate inversion operator,

$$\hat{\mathbf{f}}(\theta, \phi) = -[\mathbf{f}(\pi - \theta, \phi + \pi) \cdot \mathbf{u}_\theta]\mathbf{u}_\theta + [\mathbf{f}(\pi - \theta, \phi + \pi) \cdot \mathbf{u}_\phi]\mathbf{u}_\phi \tag{2.34}$$

where $\mathbf{u}_\theta$ and $\mathbf{u}_\phi$ are the unit vectors in the θ and ϕ direction, respectively. If the isolated antenna power patterns are symmetric in any plane through the origin then [43],

$$\hat{\mathbf{f}}(\theta, \phi) = \mathbf{f}^*(\theta^*, \phi) \tag{2.35}$$

so that (2.33) can be expressed as,

$$Z_{12}^{(0)} = 2\int_{\phi=0}^{2\pi}\int_{C} \mathbf{f}_1(\theta,\phi)\mathbf{f}_2^H(\theta^*,\phi)e^{j\mathbf{k}\cdot\mathbf{d}}\sin\theta\, d\theta d\phi \quad . \tag{2.36}$$

For a MS antenna the correction terms $Z_{12}^{(e)}$, $Z_{11}^{(e)}$, and $Z_{22}^{(e)}$, from Eqn. (2.30)-(2.32), vanish identically so that impedance parameters are completely determined by the radiation fields of the isolated antennas. The relative magnitude of the correction term in (2.32) decays as $Z_{12}^{(e)}/Z_{12}^{(0)} \sim 1/(kd)^{2n}$, with $n \geq 1$, where k is the wavenumber and d is the antenna separation distance. Likewise, $Z_{11}^{(e)} = Z_{22}^{(e)} \sim 1/(kd)^{2n}$. Consequently, the normalized mutual impedance can be approximated by the zero order term when the open circuit impedances do not differ significantly from the corresponding impedances of the isolated antennas.

2.3.6 Mean Effective Gain

A measure of the average gain of an antenna can be quantified by the Mean Effective Gain (MEG) [30]. Let $\bar{P}_\theta$ and $\bar{P}_\phi$ denote the mean incident powers of the theta and phi polarizations, respectively, averaged over a random route of the environment travelled by the antenna. The total mean incident power arriving at the antenna, averaged over the same route, is $\bar{P}_\theta + \bar{P}_\phi$. The ratio between the mean received power of an antenna over the random route, P_{rec}, and the total mean incident power is denoted as the Mean Effective Gain,

$$G_e = \frac{P_{rec}}{\bar{P}_\theta + \bar{P}_\phi} \quad . \tag{2.37}$$

The MEG is also a measure of the mean branch signal strength. The mean receive power of the antenna, P_{rec}, can be expressed as [2],

$$P_{rec} = \eta \oint \left[\bar{P}_\theta D_\theta(\Omega)P_\theta(\Omega) + \bar{P}_\phi D_\phi(\Omega)P_\phi(\Omega)\right] d\Omega \tag{2.38}$$

where η is the total antenna efficiency, D_θ and D_ϕ are the theta and phi components of the antenna directivity pattern, P_θ and P_ϕ are the probability distributions of power incident on the antenna in the θ and ϕ polarizations, and $\bar{P}_\theta$ and $\bar{P}_\phi$ are respectively the mean incident power in the theta and phi directions that would be received by perfectly polarized isotropic antennas. It follows from Eqn.

(2.38) and (2.37) that the MEG can be expressed as,

$$G_e = \eta \oint \left[\frac{XPR}{1+XPR} D_\theta(\Omega) P_\theta(\Omega) + \frac{1}{1+XPR} D_\phi(\Omega) P_\phi(\Omega) \right] d\Omega \tag{2.39}$$

where the XPR $= \bar{P}_\theta / \bar{P}_\phi$.

Chapter 3

Cross-correlation coefficient estimates for switched diversity

3.1 Introduction

Switched diversity is an economical way of improving receiver performance in a multipath environment because it requires only one receiver branch. To obtain a high diversity gain the cross-correlation of the branch signals should be low and the mean branch signal levels should be similar [1]. For a particular incident field scenario, the antenna voltage cross-correlation coefficients can be predicted from the far-field patterns of the diversity antennas [5]. However, three dimensional antenna pattern measurements are time consuming and require access to an available antenna test facility. In order to evaluate potential diversity antenna designs, antenna designers require quick means of estimating the diversity antenna performance. Although there have been estimates for the open-circuit cross-correlation coefficient formulated in terms of circuit parameters [23–25] no studies have been done to compare their accuracy. This chapter will compare the known open-circuit cross-correlation coefficient circuit estimates for the case of two parallel non-staggered dipoles.

This chapter begins by presenting the open-circuit voltage covariance matrix for an antenna array in a general incident field distribution. Expressions are presented for the open-circuit voltage covariance matrix for various simplifying assumptions on the incident field. These simplifying assumptions lead to the three-dimensional canonical case, which we call the Mobile Prototype Scenario (MPS), which is an appropriate scenario to assume when developing prototypes with mobile diversity. The Mobile Prototype Scenario (MPS) is the basis from which all the known circuit parameter estimates for the correlation coefficient are derived. The estimates for the MPSs open-circuit voltage covariance matrix are then presented and compared using CST Microwave Studio

numerical simulations. The auto-correlation coefficient is shown to be a good approximation for the voltage cross-correlation coefficient when using switch combining and the antennas behave as CMS antennas. General closed form expressions for the auto-correlation coefficient of the linear standing-wave filament antennas are then presented. Finally, an application is proposed for using the auto-correlation coefficient to verify complex antenna pattern measurement systems.

3.2 Interrelations of cross-correlation coefficients for Rayleigh multipath environments

As shown in Appendix C, the cross-correlation coefficient of the complex baseband signals can be related to the more easily measured quantities of the signal envelope and power cross-correlation coefficients. For Rayleigh multipath environments the following relations hold,

$$\rho_{r^2} = |\rho_z|^2 \tag{3.1}$$

$$\rho_r \approx |\rho_z|^2 \tag{3.2}$$

where $z(t) = r(t)e^{j\theta(t)}$ is the baseband representation of the signal. The accuracy of the estimate (3.2) for zero-mean complex Gaussians is also shown in Appendix C. In this document the power correlation coefficient, ρ_{r^2}, will be used as the standard measure for the correlation coefficient.

3.3 Open-circuit voltage cross-correlation coefficient

Using Eqn. (2.12), the covariance matrix of the open-circuit voltages, for an N element array, is given by,

$$\mathbf{C_o} = \mathbb{E}[\mathbf{V_o}\mathbf{V_o}^\dagger] \tag{3.3}$$

$$= \mathbb{E}\left[\oint \mathbf{H}(\Omega_1)\mathbf{e}(t,\Omega_1)^T\, d\Omega_1 \oint \mathbf{e}^*(t,\Omega_2)\mathbf{H}(\Omega_2)^\dagger\, d\Omega_2\right] \tag{3.4}$$

$$= \mathbb{E}\left[\oint \oint \mathbf{H}(\Omega_1)\mathbf{e}(t,\Omega_1)^T\mathbf{e}^*(t,\Omega_2)\mathbf{H}(\Omega_2)^H\, d\Omega_1\, d\Omega_2\right] \tag{3.5}$$

where $\mathbf{V_o}$ is the $N \times 1$ column vector of open-circuit voltages, $\mathbf{H}$ is the $N \times 2$ array effective height matrix (see Eqn. (2.11)), $\mathbf{e}$ is the incident electric field at co-ordinate origin, $(\cdot)^\dagger$ is the adjoint operator, and $\mathbb{E}[\cdot]$ is the expectation operator. Exchanging the order of integration and expectation in (3.5) and using Eqn. (2.4) and (2.14), the open-circuit voltage covariance matrix can be expressed as,

$$\begin{aligned}
\mathbf{C_o} =& \mathbb{E}[\mathbf{V_o}\mathbf{V_o}^\dagger] && (3.6)\\
=& \oint\oint \mathbf{H}(\Omega_1)\mathbf{C_e}\mathbf{H}(\Omega_2)^H \, d\Omega_1 \, d\Omega_2 && (3.7)\\
=& \oint\oint (\mathbf{C_h}^{\theta\theta}\mathbf{C_e}^{\theta\theta} + \mathbf{C_h}^{\phi\phi}\mathbf{C_e}^{\phi\phi} + \mathbf{C_h}^{\theta\phi}\mathbf{C_e}^{\theta\phi} + \mathbf{C_h}^{\phi\theta}\mathbf{C_e}^{\phi\theta}) \, d\Omega_1 d\Omega_2 && (3.8)\\
=& \oint\oint Tr(\mathbf{C_h}\mathbf{C_e}) \, d\Omega_1 d\Omega_2 && (3.9)
\end{aligned}$$

where the matrix trace operator, $Tr(\cdot)$, and matrix multiplication in (3.9) operated on $\mathbf{C_h}$ and $\mathbf{C_e}$ such that they are regarded as 2×2 matrices given by (2.4) and (2.14). Eqn. (3.9) is the matrix form of the result presented in [23].

As an example, the cross-correlation coefficient for the open-circuit voltages on antennas j and k is given by,

$$\rho_{ojk} = \frac{\mathbf{C_o}^{(jk)}}{\sqrt{\mathbf{C_o}^{(jj)}\mathbf{C_o}^{(kk)}}} \tag{3.10}$$

where $\mathbf{C_o}^{(ij)}$ is the matrix element in the ith row and j^{th} column of $\mathbf{C_o}$.

If the antennas are Canonical Minimum Scattering, by definition $\mathbf{C_h}$ within (3.9) can be replaced by the isolated far-field pattern coherence matrix $\mathbf{C_f}$ since for switch diversity the other elements are open-circuited. If the antennas are identical CMS antennas, and are identically aligned, (3.10) is referred to as the auto-correlation coefficient ρ_{11}. The auto-correlation coefficient will be discussed further in later sections within this chapter.

3.3.1 Open-circuit voltage cross-correlation coefficient for a simplified incident field distribution

If the incident fields satisfy the conditions that the orthogonal field polarizations are uncorrelated, and are individually uncorrelated in different angular directions, then, using (2.5), the open-circuit

voltage covariance matrix reduces to,

$$\begin{aligned}\mathbf{C_o} &= \oint\oint(\mathbf{C_h}^{\theta\theta}\mathbf{C_e}^{\theta\theta} + \mathbf{C_h}^{\phi\phi}\mathbf{C_e}^{\phi\phi})\, d\Omega_1 d\Omega_2 \\ &= \oint\oint \delta(\Omega_1 - \Omega_2)(\bar{P}_\theta P_\theta\, \mathbf{C_h}^{\theta\theta} + \bar{P}_\phi P_\phi \mathbf{C_h}^{\phi\phi})\, d\Omega_1 d\Omega_2 \\ &= \bar{P}_\phi \oint(\mathrm{XPD}\, \mathbf{C_h}^{\theta\theta} P_\theta + \mathbf{C_h}^{\phi\phi} P_\phi)\, d\Omega \end{aligned} \tag{3.11}$$

where $\bar{P}_\theta$ and $\bar{P}_\phi$ are proportional to the average incident power in the θ and ϕ components respectively, XPR$= \bar{P}_\theta/\bar{P}_\phi$ is the cross-polarization power ratio, and $P_\theta(\Omega)$ and $P_\phi(\Omega)$ are the probability distributions of incident power in the θ and ϕ components, respectively. As an example, the open-circuit voltage cross-correlation coefficient for antenna element j and k, using (3.11) and (3.10), is given by,

$$\rho_{ojk} = \frac{\oint(\mathrm{XPD}\, \mathbf{C_h}^{\theta\theta jk} P_\theta + \mathbf{C_h}^{\phi\phi jk} P_\phi)\, d\Omega}{\sqrt{\oint(\mathrm{XPD}\, \mathbf{C_h}^{\theta\theta jj} P_\theta + \mathbf{C_h}^{\phi\phi jj} P_\phi)\, d\Omega \oint(\mathrm{XPD}\, \mathbf{C_h}^{\theta\theta kk} P_\theta + \mathbf{C_h}^{\phi\phi kk} P_\phi)\, d\Omega}} \quad . \tag{3.12}$$

Simulations [11, 13, 17] have been performed using (3.12) assuming the typical Gaussian incident field distributions (2.6)-(2.7). The studies performed in [11] seem to have been the only work in the literature that have investigated the sensitivity of the correlation coefficient to the parameters of the Gaussian incident field distributions (2.6)-(2.7).

3.3.2 Open-circuit voltage cross-correlation coefficient for Mobile Prototype Scenarios

In order to evaluate prototypes of mobile devices which incorporate diversity antennas it is reasonable to assume incident field distribution of the Mobile Prototype Scenarios. For MPSs, (3.12) further reduces to,

$$\begin{aligned}\mathbf{C_o} =& P \oint(\mathbf{C_h}^{\theta\theta} + \mathbf{C_h}^{\phi\phi})\, d\Omega \\ =& P \oint Tr(\mathbf{C_h})\, d\Omega \\ =& P \oint \mathbf{H}\mathbf{H}^\dagger\, d\Omega \end{aligned} \tag{3.13}$$

where P is proportional to the average incident power and again the matrix trace operator, $Tr(\cdot)$, operates on $\mathbf{C_h}$ such that it is considered the 2×2 matrix (2.14). For example, the open-circuit voltage cross-correlation coefficient for antenna element j and k in a MPS, using (3.13), is given by,

$$\rho_{ojk} = \frac{\oint \mathbf{h}_j \mathbf{h}_k^{\dagger} \, d\Omega}{\sqrt{\oint |\mathbf{h}_j|^2 \, d\Omega \oint |\mathbf{h}_k|^2 \, d\Omega}} \quad . \tag{3.14}$$

Eqn. (3.14) is almost universally used in literature to predict the cross-correlation coefficient from antenna patterns.

3.3.2.1 Open-circuit voltage cross-correlation coefficient for MPSs for CMS antennas

If the antennas under consideration are CMS antennas then their open-circuit effective heights vectors are proportional to their isolated far-field radiation patterns. Thus in (3.13) the open-circuit antenna array coherence matrix $\mathbf{C_h}$ can be replaced by the isolated far-field pattern coherence matrix,

$$\mathbf{C_o} = P \oint Tr(\mathbf{C_f}) \, d\Omega \tag{3.15}$$

where P is proportional to the average incident power and $\mathbf{C_f}$ is the isolated far-field pattern coherence matrix given in Eqn. (2.19), and matrix trace operator, $Tr(\cdot)$, operates such that $\mathbf{C_f}$ is considered the 2×2 matrix (2.19).

3.3.2.2 Antenna auto-correlation coefficient for MPSs

If, in addition to being CMS antennas, the antennas are also identical and identically aligned the elements of the open-circuit covariance matrix are spatial samples of the open-circuit voltage auto-correlation coefficient for MPSs,

$$\rho_{11} = \oint |\mathbf{f}|^2 e^{j\mathbf{k}\cdot\mathbf{d}} \, d\Omega \tag{3.16}$$

where $\mathbf{f}$ is the normalized isolated antenna pattern and $\mathbf{d}$ spatial separation distance vector. As seen from (3.16), the open-circuit voltage auto-correlation coefficient for a CMS antenna is real: a translation of the origin to the other antenna position leads to the conjugation of the auto-correlation, and since the auto-correlation is origin independent it is equal to its conjugate and hence is real.

3.3.2.3 Open-circuit voltage cross-correlation coefficient for Clarke's two dimensional scenarios

In addition to the incident field assumptions of a Mobile Prototype Scenario, Clarke's model [2,45] assumes the incident fields are confined to the $\theta = \pi/2$ plane. For example, for two polarization matched antennas with identical uniform far-field patterns in the $\theta = \pi/2$ plane, the open-circuit voltage cross-correlation in Clarke's scenario is given by (3.12) as,

$$\rho_{o12} = \frac{\oint (\mathbf{C_h}^{\theta\theta 12} P_\theta + \mathbf{C_h}^{\phi\phi 12} P_\phi)\, d\Omega}{\sqrt{\oint (\mathbf{C_h}^{\theta\theta 11} P_\theta + \mathbf{C_h}^{\phi\phi 11} P_\phi)\, d\Omega \oint (\mathbf{C_h}^{\theta\theta 22} P_\theta + \mathbf{C_h}^{\phi\phi 22} P_\phi)\, d\Omega}} \tag{3.17}$$

$$= \frac{1}{2\pi} \frac{\oint \mathbf{h}_1(\pi/2, \phi) \mathbf{h}_2(\pi/2, \phi)^\dagger\, d\phi}{\oint |\mathbf{h}(\pi/2, \phi)|^2\, d\phi} \tag{3.18}$$

$$= \frac{1}{2\pi} \oint e^{jkd\cos\phi}\, d\phi \tag{3.19}$$

$$= J_0(kd) \tag{3.20}$$

where $J_0(\cdot)$ is the zeroth order Bessel function of the first kind. A generalized Clarke's model can be obtained by assuming orthogonal polarizations are uncorrelated, individually uncorrelated in polar direction, and confined to the plane $\theta = \pi/2$. The open-circuit voltage cross-correlation coefficient for generalized Clarke's Scenario becomes,

$$\rho_{ojk} = \frac{\oint (\mathrm{XPD}\, \mathbf{C_h}^{\theta\theta jk} P_\theta(\phi) + \mathbf{C_h}^{\phi\phi jk} P_\phi(\phi))\, d\phi}{\sqrt{\oint (\mathrm{XPD}\, \mathbf{C_h}^{\theta\theta jj} P_\theta(\phi) + \mathbf{C_h}^{\phi\phi jj} P_\phi(\phi))\, d\phi \oint (\mathrm{XPD}\, \mathbf{C_h}^{\theta\theta kk} P_\theta(\phi) + \mathbf{C_h}^{\phi\phi kk} P_\phi(\phi))\, d\phi}} . \tag{3.21}$$

3.3.2.4 Comparison of MPS and Clarke's two dimensional scenario

The cross-correlation coefficients of diversity antenna prototypes are commonly evaluated using Clarke's two dimensional scenario with uniform or non-uniform azimuthal incident distributions [6, 9, 10, 46–49]. These assumed incident fields are inaccurate for most scenarios involving mobile devices and could be improved with the use of the Mobile Prototype Scenario. For example, the incident fields for the antennas on a mobile phone in a dense urban area can be well approximated by the Mobile Prototype Scenario since the elevation angle of the phone will change frequently as the user adjusts the phone position and the standard deviations in Eqn. (2.6) and (2.7) are typically large.

It is also common [50] for the auto-correlation coefficient to be compared with (3.20) however for environments with a large angular spread, such as indoor environments, a more realistic comparison should be made with (3.16) [51].

3.4 Estimation of the open-circuit cross-correlation coefficient for switch diversity

In the previous sections of this chapter, theoretical means of predicting the cross-correlation coefficient were presented for various incident field distributions. For the Mobile Prototype Scenario, it was shown that the cross-correlation coefficient can be expressed in terms of the antenna far-field patterns alone. In order to avoid measuring the antenna patterns while evaluating prototypes with diversity antennas, methods have been developed for MPSs to estimate the correlation coefficient from circuit parameters; thus possibly allowing for quick and simple means of evaluating multi-antenna designs. This section outlines the formulations for the three known methods for estimating for the cross-correlation coefficient between switch diversity elements.

3.4.1 Open-circuit voltage cross-correlation coefficient estimated from the isolated far-field patterns

Most intuitive estimate for the open-circuit voltage cross-correlation coefficient between branches of a switched combining receiver is to assume that the open-circuit elements are electrically invisible. This assumption is equivalent to assuming the elements are CMS antennas. For such an approximation the open-circuit antenna array coherence matrix is replaced by the isolated far-field pattern coherence matrix. From (3.9), the open-circuit covariance matrix can thus be approximated for the case of a general incident field by,

$$\mathbf{C_o} \approx \oint \oint Tr(\mathbf{C_f}\mathbf{C_e})\, d\Omega_1 d\Omega_2 \tag{3.22}$$

where again the matrix trace operator, $Tr(\cdot)$, and matrix multiplication operate on $\mathbf{C_h}$ and $\mathbf{C_e}$ such that they are considered the 2×2 matrices given by (2.4) and (2.14). For MPSs, the approximation

for the open-circuit covariance matrix, from (3.13), becomes proportional to,

$$\mathbf{C_o} \approx \oint Tr(\mathbf{C_f})\, d\Omega \quad . \tag{3.23}$$

The validity of assuming CMS antennas depends on the individual antennas used. The reasons for which this approximation has not yet been introduced into the general literature is that (1) it is not a circuit parameter estimate and (2) must be determined through numerical simulations for most antenna patterns. Obtaining accurate antenna pattern estimates for most mobile devices tend to be complicated since the antennas are compact and must placed near metallic objects within the devices; so the effective antenna pattern is usually difficult to predict. However, approximation (3.22) does allow for estimating the correlation coefficient for different incident field distribution; a virtue the circuit parameter estimates lack.

As an example, the isolated far-field pattern estimate for open-circuit voltage cross-correlation coefficient for a two element array, using (3.10) and (3.23), is given by

$$\rho_{o12} = \frac{\oint \mathbf{f}_1 \mathbf{f}_2^{\dagger}\, d\Omega}{\sqrt{\oint |\mathbf{f}_1|^2\, d\Omega \oint |\mathbf{f}_2|^2\, d\Omega}} \tag{3.24}$$

where $\mathbf{f}$ are the isolated far-field patterns of the respective antenna elements.

3.4.2 Open-circuit voltage cross-correlation coefficient estimated from the normalized mutual resistance

In the previous section, the first correlation coefficient estimate was presented based on approximating the antenna patterns. This section presents the first circuit parameter estimate for the correlation coefficient and it is based on expressions for the mutual coupling between antennas.

In Eqn.(2.36) for the zeroth order term of the mutual impedance, the mutual resistance corresponds to the real part of the integration over real space. This can be seen from the fact that, in a lossless environment, power transfer can only occur in real space [23]. If the antenna patterns in (2.36) are expressed with respect to a common co-ordinate datum, and each isolated antenna has symmetric power patterns in any plane through the origin, the zeroth order terms of the normalized

mutual resistance is given by,

$$r_{jk}^{(0)} = \frac{R_{jk}^{(0)}}{\sqrt{R_{jj}R_{kk}}} = \text{Re}\left[\oint \mathbf{f}_j(\Omega)\mathbf{f}_k^{\dagger}(\Omega)\, d\Omega\right] \quad . \tag{3.25}$$

Eqn. (3.25) is recognized as the real part of the open-circuit cross-correlation coefficient for the case of CMS antennas used in conjunction with switch diversity in a MPS. Thus an approximation for the real part of the open-circuit cross-correlation is given by [23],

$$\text{Re}[\rho_{ojk}] = \text{Re}\left[\oint \mathbf{f}_j\mathbf{f}_k^{\dagger}\, d\Omega\right] \approx r_{jk} \tag{3.26}$$

where the relation is an equality for CMS antennas.

3.4.2.1 Auto-correlation coefficient and normalized mutual resistance

It follows from (3.26) that the auto-correlation coefficient of a CMS antenna is equivalent to the zeroth order term of the normalized mutual resistance,

$$\rho_{11} = r_{12}^{(0)} \tag{3.27}$$

where ρ_{11} is the auto-correlation coefficient of a CMS antenna and $r_{12}^{(0)}$ is the zeroth order term of the normalized mutual resistance between the two identical antennas. As noted in previous literature [43], the assumption of CMS antennas is common to most elementary approximation techniques; this includes the "induced EMF" method [52] for mutual impedance calculations among linear filamentary antennas. Thus for normalized mutual resistance calculation based on methods such as the "induced EMF", (3.27) is a mathematical identity and proves useful for the evaluation of auto-correlation coefficient expressions.

3.4.3 Open-circuit cross-correlation coefficient estimation from *S*-parameters for MPSs

The formulation of determining the cross-correlation coefficient from *S*-parameters for lossless antennas in MPSs was first presented for the case of perfectly matched antennas [24]. The following

derivation is based on the generalization to mismatched antennas as presented in [25].

For single current mode antennas, the electric far-field of an N element array can be expressed as,

$$\mathbf{e}(\Omega) = \frac{jZke^{-jkr}}{4\pi r}\sum_{n=1}^{N}\mathbf{h}_n(\Omega)i_n \tag{3.28}$$

$$= \frac{jZke^{-jkr}}{4\pi r}\mathbf{i}^T\mathbf{H}(\Omega) \tag{3.29}$$

where i_n is the current on the nth element, $\mathbf{h}_n(\Omega)$ is the far-field radiation pattern of the nth element when all the other elements are open-circuited, $\mathbf{i}$ is the $N \times 1$ column vector of currents, $\mathbf{H}$ is the $N \times 2$ Array Effective Height Matrix as given in (2.11), k is the wavenumber, and Z is the wave impedance of the medium. The average power radiated by the array can be expressed as,

$$P_{rad} = \left(\frac{1}{2Z}\right)\oint |\mathbf{e}(\Omega)|^2\, d\Omega \tag{3.30}$$

$$= \left(\frac{Zk^2}{32\pi^2}\right)\mathbf{i}^T\left[\oint \mathbf{H}\mathbf{H}^\dagger\, d\Omega\right]\mathbf{i}^* \tag{3.31}$$

$$= \left(\frac{Z}{8\lambda^2 Z_c}\right)\mathbf{a}^T(\mathbf{I}-\mathbf{S})^T\left[\oint \mathbf{H}\mathbf{H}^\dagger\, d\Omega\right](\mathbf{I}-\mathbf{S})^*\mathbf{a}^* \tag{3.32}$$

where $\mathbf{a}$ is the incident wave vector and $\mathbf{S}$ is the scattering matrix of the antenna ports, respectively. For loseless antennas, the power lost by the antenna network can be assumed to be radiated. From network theory, the average power loss within a network is given by [40],

$$P_{loss} = \left(\frac{1}{2}\right)(|\mathbf{a}|^2 - |\mathbf{b}|^2) = \mathbf{a}^\dagger\frac{(\mathbf{I}-\mathbf{S}^\dagger\mathbf{S})}{2}\mathbf{a} \tag{3.33}$$

$$= \mathbf{a}^T\frac{(\mathbf{I}-\mathbf{S}^T\mathbf{S}^*)}{2}\mathbf{a}^* \quad . \tag{3.34}$$

Equating (3.32) and (3.34) we obtain an expression for the solid angle integration of the antenna array coherence matrix in terms of antenna S-parameters only,

$$\left[\oint \mathbf{H}\mathbf{H}^\dagger\, d\Omega\right] = \left(\frac{4\lambda^2 Z_c}{Z}\right)(\mathbf{I}-\mathbf{S}^T)^{-1}(\mathbf{I}-\mathbf{S}^T\mathbf{S}^*)(\mathbf{I}-\mathbf{S}^*)^{-1} \quad . \tag{3.35}$$

For reciprocal antenna networks, the antenna network is symmetric so that (3.35) simplifies to,

$$\left[\oint \mathbf{H}\mathbf{H}^{\dagger}\, d\Omega\right] = \left(\frac{4\lambda^2 Z_c}{Z}\right)(\mathbf{I}-\mathbf{S})^{-1}(\mathbf{I}-\mathbf{S}\mathbf{S}^{*})(\mathbf{I}-\mathbf{S}^{*})^{-1} \quad . \tag{3.36}$$

Thus for MPSs, the open-circuit voltage covariance matrix can be approximated by (see (3.13)),

$$\mathbf{C_o} = \left(\frac{4P\lambda^2 Z_c}{Z}\right)(\mathbf{I}-\mathbf{S}^{T})^{-1}(\mathbf{I}-\mathbf{S}^{T}\mathbf{S}^{*})(\mathbf{I}-\mathbf{S}^{*})^{-1} \tag{3.37}$$

where P is proportional to the average incident power.

3.5 Numerical simulation results comparing the open-circuit voltage cross-correlation coefficients estimates

In order to compare the three estimates for the cross-correlation coefficient of the open-circuit voltages, two parallel non-staggered cylindrical $\lambda/2$ dipole antennas were simulated using CST Microwave Studio. From these CST simulations we obtained the antenna effective heights, the isolated far-field patterns, and S-parameters data as a function of antenna separation distance. To determine the effective antenna height patterns for each separation distance one dipole was driven by a 50Ω source while the other dipole was open-circuited. The S-parameters were obtained for each separation distance by terminating each antenna by a 50Ω port. Finally, we obtained the isolated far-field pattern by simulating a single dipole in isolation. The data processed using MATLAB.

We performed two different simulation sets to investigate the assumptions based on the antennas being Canonical Minimum Scattering: the first simulation set used dipoles with radii $= \lambda/100$ and second set used dipoles with radii $= \lambda/1000$. Appendix D shows the figures of the simulation models and tables with the simulation settings. Plots of the self and mutual impedances are shown in Figure 3.2 for both sets dipole thicknesses. From these impedance plots, one can see that the $r = \lambda/1000$ dipole will be approximately CMS as indicated from the low fluctuation of the self-resistance, whereas the $r = \lambda/100$ dipole shows a higher fluctuation will not closely behave as a CMS.

Samples of the simulated antenna matching and coupling as a function of separation distance

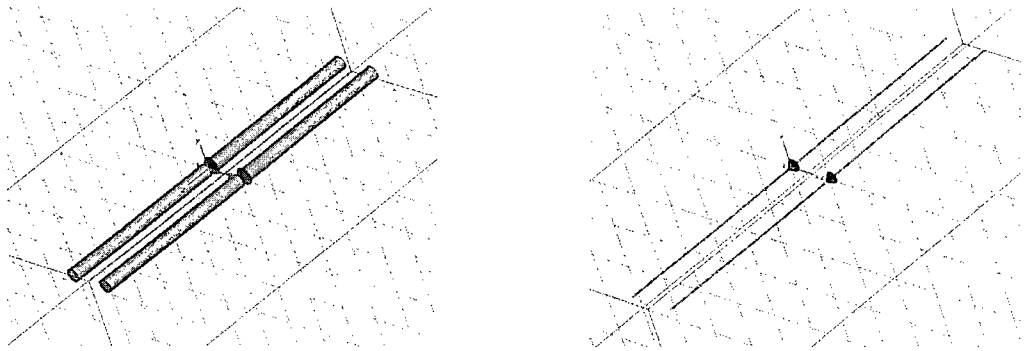

(a) $\lambda/100$ dipoles (b) $\lambda/1000$ dipoles

Figure 3.1: Two parallel non-staggered cylindrical dipoles simulated to compare the estimates for the cross-correlation coefficient of the open-circuit voltages.

are shown in Appendix F. Based on the antenna matching frequency extremes, the data sets for 808 MHz and 850 MHz were used for all the correlation calculations involving the dipoles with radii $= \lambda/100$ and $\lambda/1000$, respectively. At these frequencies, the antennas were matched better than -12dB for all separation distances; i.e. $S_{ii} < -12dB$.

The theoretical cross-correlation coefficient for the open-circuit voltages in a MPS was determined from the far-field patterns using (3.14). The normalized mutual resistance estimates were calculated using (3.26) derived from the obtained S-parameter using relation (2.27). The S-parameter estimate was calculated using (3.37) and (3.10). Finally, the auto-correlation coefficient was calculated by using (3.16) with the far-field patterns obtained from the simulations of an isolated dipole.

Figures 3.3-3.4 show the simulation results for the different correlation estimates for the two sets of dipoles thicknesses; with radii equal to $\lambda/100$ and $\lambda/1000$, respectively. These figures show that the correlation coefficient quickly decreases below a value of 0.5 for separation distances greater than $\sim 0.3\lambda$. All the estimates of the correlation coefficient were found to trend well with the theoretical value for both radii simulation sets. The auto-correlation was the only estimate which matched very closely with the theoretical value; the match worsened for small separation distances with the thicker dipoles ($r = \lambda/100$.) The S-parameter and normalized mutual resistance estimates were found to yield values lower than the theoretical curve but matched closely to each other. The discrepancy between the S-parameter and normalized mutual resistance estimates for small separation distances stems from the original definition of the normalized mutual resistance (2.32). In this

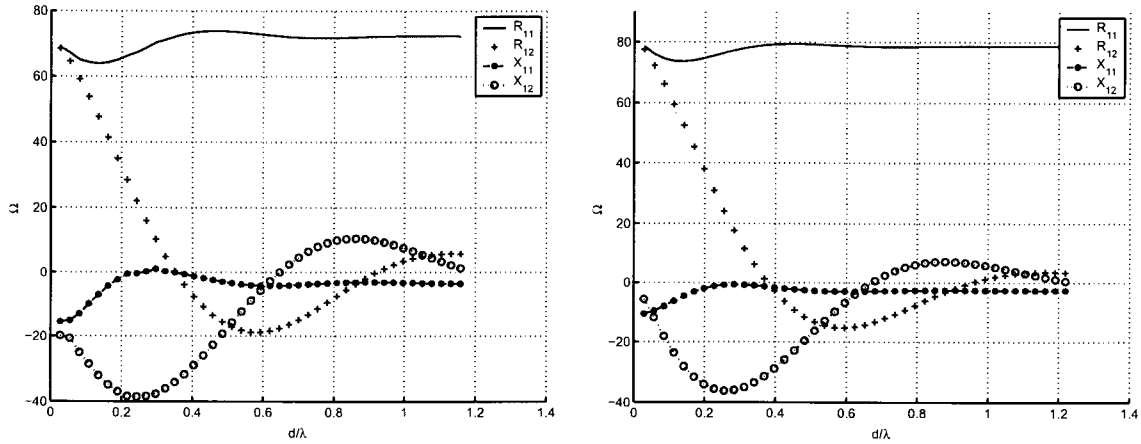

(a) $\lambda/100$ dipole impedances

(b) $\lambda/1000$ dipole impedances

Figure 3.2: Self and mutual impedances of simulated cylinder dipoles ($r = \lambda/1000$ and $r = \lambda/100$ for $\lambda = 33.9cm$) as a function of separation distance; measured at 808MHz and 850MHz, respectively.

definition, the mutual resistance is normalized by the self-impedances of the antennas in isolation. If the mutual resistance is normalized by the self-impedances of the antennas (with the other antenna present) the S-parameter and normalized mutual resistance estimates match exactly; as shown in Appendix G. The S-parameter and normalized mutual resistance estimates were found be very sensitive to antenna impedance. By calculating the correlation estimates at a different frequency, the S-parameter and normalized mutual resistance estimates were found to varying significantly; as shown in Appendix H.

These results indicate that the auto-correlation can be used to estimate the theoretical open-circuit cross-correlation coefficient between parallel non-staggered thin dipoles for switch diversity. This being the case, in the next section we derive closed-form expressions for the auto-correlation of linear filament antenna. The results also show that the known circuit-parameter based methods for estimating the cross-correlation coefficient can be inaccurate and care must be taken when using the estimates for closely spaced antennas since they seem strongly dependent of the antenna impedance.

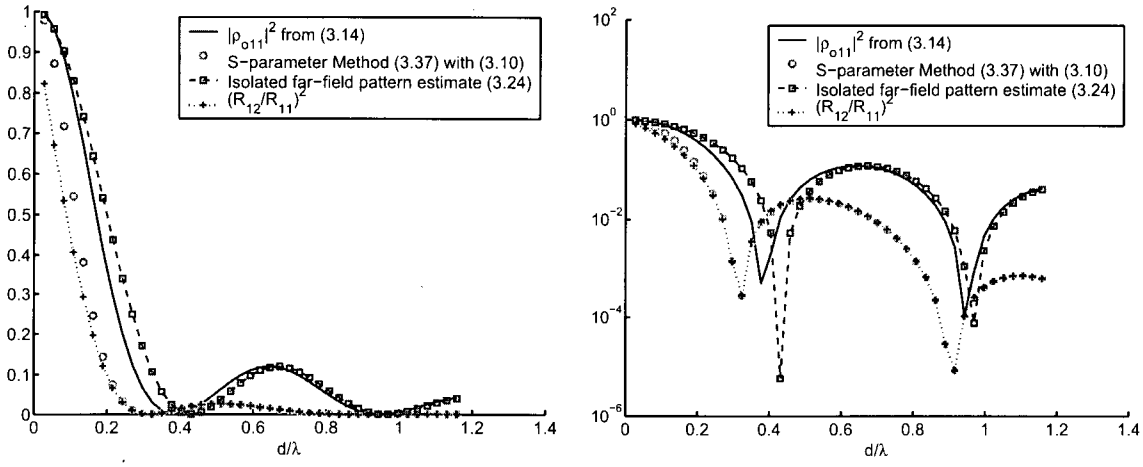

(a) Linear scale (b) Log scale

Figure 3.3: Cross-correlation coefficient of the open-circuit voltages (parasitic element open circuited), self-correlation, normalized mutual resistance, and S-parameter estimate methods for two dipoles ($r = \lambda/100$) simulated in CST Microwave Studio.

3.6 Theoretical auto-correlation coefficient for linear standing-wave antennas

The results from the previous section suggest that the cross-correlation coefficient of open-circuit voltages can be well approximated by the auto-correlation coefficient when the antennas are approximately CMS. In this section we present closed form expressions for the auto-correlation for linear standing-wave antennas. These closed form expressions allow for the easy generation of reference curves.

3.6.1 Theoretical auto-correlation coefficient of linear standing-wave antennas of length L

The current distribution on a standing-wave linear antenna of length L is given by,

$$I(z) = I_0 \sin\left(k(L/2 - |z|)\right) \tag{3.38}$$

where I_0 is the peak current amplitude, k is the wavenumber, and L is the total length of the linear antenna. The far-field pattern for a linear antenna of length L with a current distribution (3.38) is

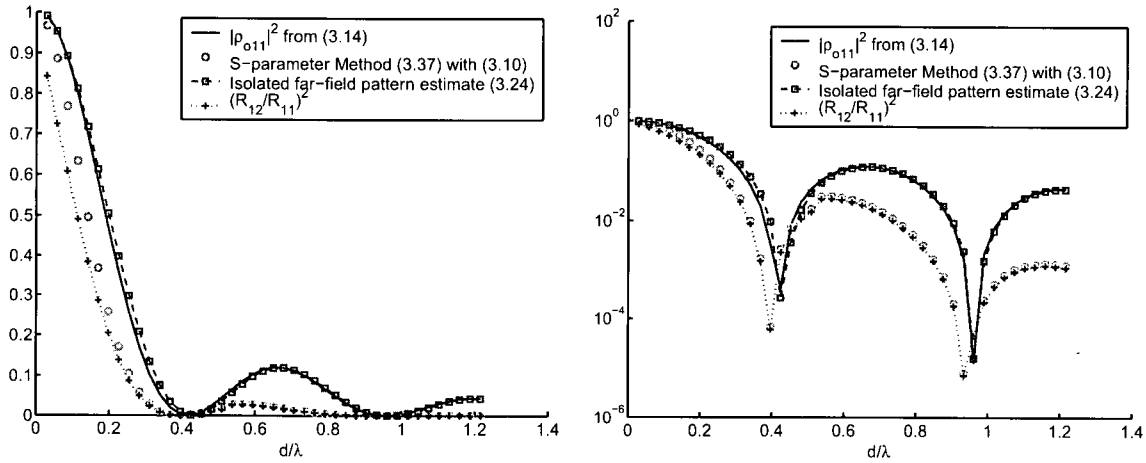

(a) Linear scale (b) Log scale

Figure 3.4: Cross-correlation coefficient of the open-circuit voltages (parasitic element open circuited), self-correlation, normalized mutual resistance, and S-parameter estimate methods for two dipoles ($r = \lambda/1000$) simulated in CST Microwave Studio.

given by [22],

$$\mathbf{h} = \left(\frac{2}{k}\right)\left(\frac{\cos(\frac{kL}{2}\cos\theta) - \cos(kL/2)}{\sin\theta}\right)\mathbf{u}_\theta \tag{3.39}$$

where k is the wavenumber, and L is the total length of the linear filament antenna. For Mobile Prototype Scenarios, the auto-correlation coefficient of (3.39) in the x-direction is given by (3.16) as,

$$\rho_{11} = \frac{\oint\left(\frac{\cos(\frac{kL}{2}\cos\theta)-\cos(kL/2)}{\sin\theta}\right)^2 e^{j\mathbf{k}\cdot\mathbf{d}}\,d\Omega}{\oint\left(\frac{\cos(\frac{kL}{2}\cos\theta)-\cos(kL/2)}{\sin\theta}\right)^2 d\Omega} \tag{3.40}$$

$$= \frac{\int_0^{2\pi}\int_0^{\pi}\left(\frac{\left(\cos(\frac{kL}{2}\cos\theta)-\cos(kL/2)\right)^2}{\sin\theta}\right) e^{j\frac{2\pi}{\lambda}d\cos\phi\sin\theta}\,d\theta\,d\phi}{\int_0^{2\pi}\int_0^{\pi}\left(\frac{\left(\cos(\frac{kL}{2}\cos\theta)-\cos(kL/2)\right)^2}{\sin\theta}\right) d\theta\,d\phi} \tag{3.41}$$

$$= \frac{\int_0^{\pi}\left[\cos^2\left(\frac{kL}{2}\cos\theta\right) - 2\cos\left(\frac{kL}{2}\cos\theta\right)\cos(kL/2) + \cos^2(kL/2)\right]\frac{J_0(kd\sin\theta)}{\sin\theta}\,d\theta}{\int_0^{\pi}\frac{\cos^2\left(\frac{kL}{2}\cos\theta\right)-2\cos\left(\frac{kL}{2}\cos\theta\right)\cos(kL/2)+\cos^2(kL/2)}{\sin\theta}\,d\theta} \tag{3.42}$$

where $J_0(\cdot)$ is the zeroth order Bessel function of the first kind. From (3.27), it follows that this expression is equivalent to [53],

$$\begin{aligned}\rho_{11} = \left(\frac{1}{\sin^2(kL/2)\Gamma}\right) \Bigg\{ & 2(2+\cos(kL))\mathrm{Ci}\,(kd) \\ & - 4\cos^2\left(\frac{kL}{2}\right)\left[\mathrm{Ci}\,(k(\sqrt{4d^2+L^2}-L)/2) + \mathrm{Ci}\,(k(\sqrt{4d^2+L^2}+L)/2)\right] \\ & + \cos(kL)\left[\mathrm{Ci}\,(k(\sqrt{d^2+L^2}-L)) + \mathrm{Ci}\,(k(\sqrt{d^2+L^2}+L))\right] \\ & + \sin(kL)\Big[\mathrm{Si}\,(k(\sqrt{d^2+L^2}+L)) - \mathrm{Si}\,(k(\sqrt{d^2+L^2}-L)) \\ & -2\mathrm{Si}\,(k(\sqrt{4d^2+L^2}+L)/2) + 2\mathrm{Si}\,(k(\sqrt{4d^2+L^2}-L)/2)\Big]\Bigg\} \end{aligned} \tag{3.43}$$

where $\gamma = 0.57721566490153...$ is Euler's constant,

$$\mathrm{Si}(x) = \int_0^x \frac{\sin x}{x}\,dx \tag{3.44}$$

$$\mathrm{Ci}(x) = -\int_x^\infty \frac{\cos x}{x}\,dx \tag{3.45}$$

$$\begin{aligned}\Gamma =& 2(\gamma + \ln(kL) - \mathrm{Ci}\,(kL)) + \sin(kL)(\mathrm{Si}\,(2kL) - 2\mathrm{Si}\,(kL)) \\ & + \cos(kL)(\gamma + \ln(kL/2) + \mathrm{Ci}\,(2kL) - 2\mathrm{Ci}\,(kL)) \quad .\end{aligned} \tag{3.46}$$

The auto-correlation coefficient of linear standing-wave antennas, for different lengths L, can be seen in Figure 3.5. It can be seen from these figure that there is very little variation in the auto-correlation coefficient of linear standing-wave antennas for lengths less than 0.6λ. This result is expected since the antenna patterns are very similar for this range of antenna lengths.

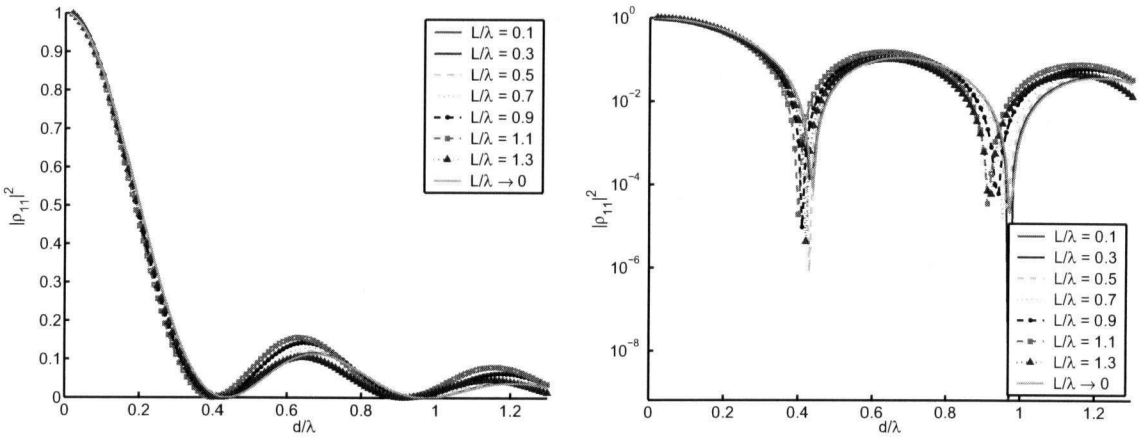

(a) Linear scale (b) Log scale

Figure 3.5: Auto-correlation for infinitely thin linear standing-wave antenna for varying lengths.

3.6.2 Theoretical auto-correlation coefficient of a $\lambda/2$ linear standing-wave antenna

For the special case of a linear antenna of length $L = \lambda/2$, the auto-correlation coefficients (3.42) and (3.43) reduce to,

$$\begin{aligned}
\rho_{11} =& \frac{\oint \frac{\cos^2(\frac{\pi}{2}\cos\theta)}{\sin^2\theta} e^{j\mathbf{k}\cdot\mathbf{d}}\, d\Omega}{\oint \frac{\cos^2(\frac{\pi}{2}\cos\theta)}{\sin^2\theta}\, d\Omega} \\
=& \frac{\int_0^{2\pi}\int_0^{\pi} \frac{\cos^2(\frac{\pi}{2}\cos\theta)}{\sin\theta} e^{j\frac{2\pi}{\lambda}d\cos\phi\sin\theta}\, d\theta\, d\phi}{\int_0^{2\pi}\int_0^{\pi} \frac{\cos^2(\frac{\pi}{2}\cos\theta)}{\sin\theta}\, d\theta\, d\phi} \\
=& \frac{2}{\mathrm{Cin}(2\pi)} \int_0^{\pi} \frac{\cos^2(\frac{\pi}{2}\cos\theta)}{\sin\theta} J_0(kd\sin\theta)\, d\theta \qquad (3.47) \\
=& \frac{1}{\mathrm{Cin}(2\pi)} \left\{ 2\mathrm{Ci}(kd) - \mathrm{Ci}\left[k(\sqrt{d^2+L^2}+L)\right] - \mathrm{Ci}\left[k(\sqrt{d^2+L^2}-L)\right] \right\} \qquad (3.48)
\end{aligned}$$

where $J_0(\cdot)$ is the zero order Bessel function of the first kind, k is the wavenumber, $L = \lambda/2$, and $\mathrm{Cin}(\cdot)$ is related to the cosine integral,

$$\begin{aligned}
\mathrm{Cin}(x) =& \int_0^x \frac{1-\cos\tau}{\tau}\, d\tau \qquad (3.49) \\
=& \gamma + \ln(x) - \mathrm{Ci}(x) \qquad (3.50)
\end{aligned}$$

where γ is Euler's constant, and $\mathrm{Ci}(\cdot)$ is given by (3.45). The denominator of (3.47) was simplified by the well known relation [54],

$$D = \int_0^{2\pi} \int_0^{\pi} \frac{\cos^2(\frac{\pi}{2}\cos\theta)}{\sin\theta}\, d\theta\, d\phi \tag{3.51}$$

$$= \pi \mathrm{Cin}(2\pi) \quad . \tag{3.52}$$

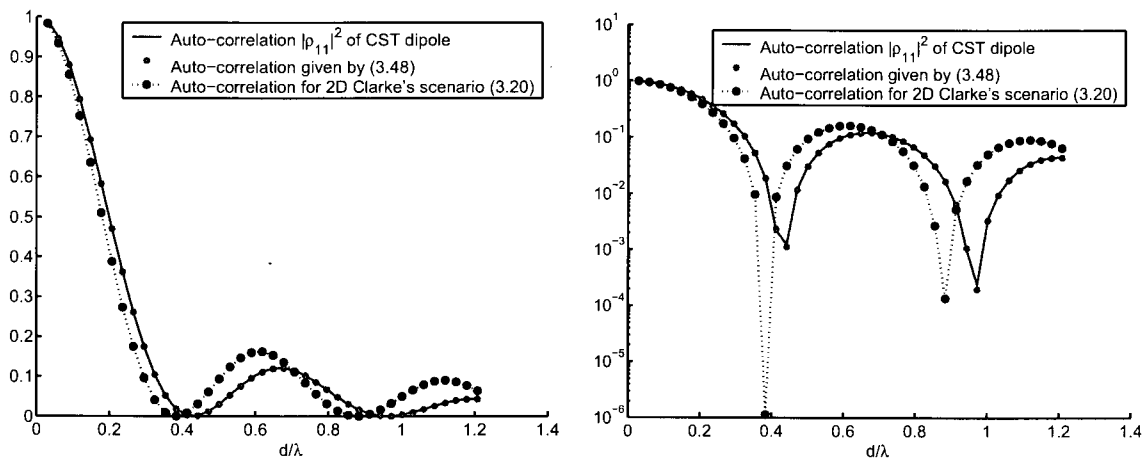

(a) Linear scale (b) Logarithmic scale

Figure 3.6: Auto-correlation of a $\lambda/2$ dipole determined from the field pattern obtained from CST Microwave Studio, Eqn.3.48, and 2D Clarke's Scenario. The CST dipole has a radius of $\lambda/100$, $\lambda = 33.9$ cm, and the field pattern was obtained at 884 MHz.

Figure 3.6 shows the auto-correlation calculated based on the field pattern obtained from CST of $\lambda/2$ dipole, a plot of Eqn.(3.48), and a plot of the auto-correlation of a dipole in 2D Clarke's scenario. It can be seen from the figure that formula (3.48) matches almost exactly with the values calculated based on the field pattern.

3.6.3 Theoretical auto-correlation coefficient of a Hertzian dipole

For the special case of a linear antenna with length $L \to 0$, the normalized field patterns reduces to,

$$\mathbf{h} = \sin\theta \mathbf{u}_\theta \quad . \tag{3.53}$$

The auto-correlation coefficient for a Hertian dipole in a MPS is given by,

$$\rho_{11} = \frac{\oint \sin^2\theta e^{j\mathbf{k}\cdot\mathbf{d}}\, d\Omega}{\oint \sin^2\theta\, d\Omega} \tag{3.54}$$

$$= \frac{\int_0^{2\pi}\int_0^{\pi} \sin^3\theta e^{j\frac{2\pi}{\lambda}d\cos\phi\sin\theta}\, d\theta\, d\phi}{\int_0^{2\pi}\int_0^{\pi} \sin^3\theta\, d\theta\, d\phi} \tag{3.55}$$

$$= \frac{3}{4}\int_0^{\pi} \sin^3\theta J_0(kd\sin\theta)\, d\theta \tag{3.56}$$

$$= \frac{3}{2kd}\left[\sin(kd) + \frac{\cos(kd)}{kd} - \frac{\sin(kd)}{(kd)^2}\right] \tag{3.57}$$

where the last equality is shown in Appendix I. As shown in Appendix I, Eqn. (3.57) is derived from the auto-correlation coefficient of the Hertzian dipole field patterns and agrees with the known result for the normalized mutual resistance [38]; as it must from the mathematical identity (3.27).

3.6.4 Application of the auto-correlation coefficient for antenna measurement system verification

Equation (3.43), or more specifically Eqn. (3.48) or (3.57), can be used to quickly verify of the magnitude and phase measurement accuracy of an antenna pattern measurement system. By comparing the auto-correlation coefficients of the measured complex antenna patterns of a single linear dipole antenna as a function of perpendicular translation distance with those obtained from Eqn. (3.43) one can verify that the magnitude and phase measurements are not incorrect. It should be noted that the dipole should be fed from a null in its pattern so as to minimize the affects of the feeding cable on its far-field radiation pattern.

Using an antenna pattern measurement system, build in-house at Nokia, the auto-correlation coefficient were measured using reference sleeve $\lambda/2$ dipoles over three different frequency bands [51]. The reference dipoles were designed by Satimo (Courtaboeuf, France) for use as a precision gain reference measurements. The low loss end-fed sleeve dipole technology minimizes cable and feed point interaction. An innovative choke design further reduces cable interaction by attenuating the natural return currents from the dipole. Measurement results are shown in Fig.3.7 along with the theoretical auto-correlation coefficient for MPSs (Eqn (3.48)) and Clarke's two dimensional uniform scenario for comparison.

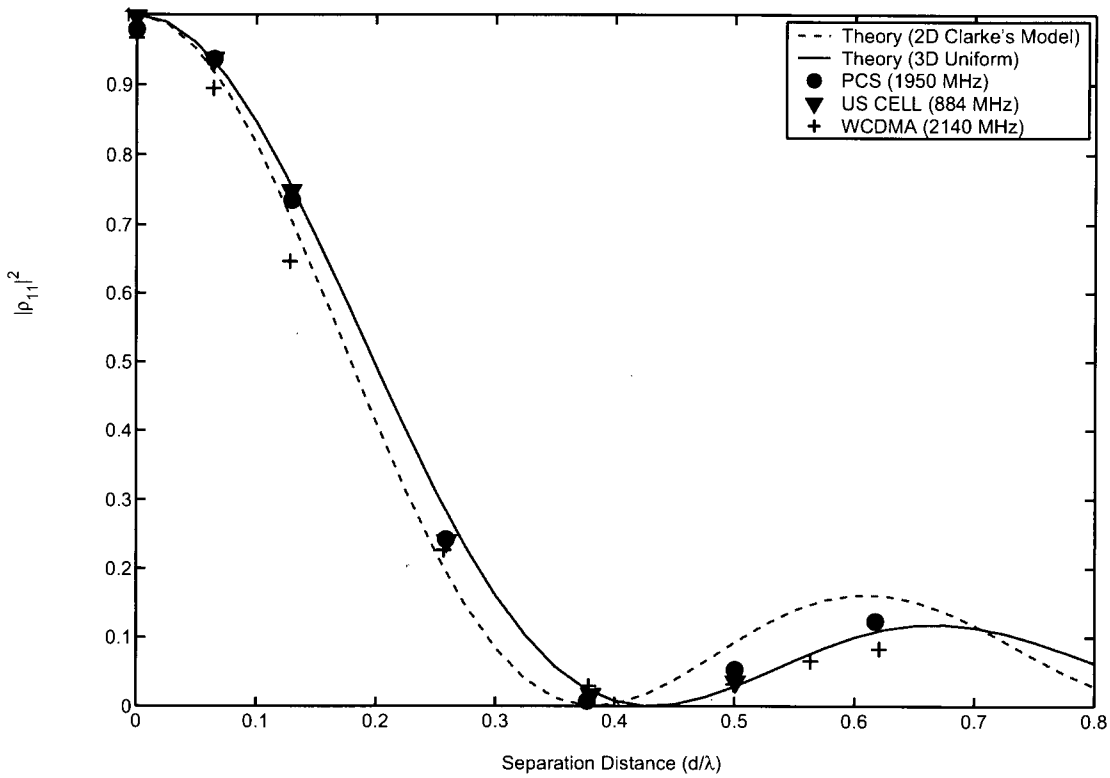

Figure 3.7: Measured auto-correlation coefficient of Satimo $\lambda/2$ sleeve dipoles (884 MHz, 1900 MHz, and 2050 MHz) and theoretical two and three dimensional uniform incident auto-correlation coefficient. (linear scale)

3.7 Discussion

Within this chapter, we presented a formulation for the open-circuit voltage cross-correlation coefficients and its estimates in a general matrix form. This improves tractability in formulations and theoretical pursuits.

We have shown by numerical simulations that all three of the known methods of estimating the cross-correlation coefficient trended well with the theoretical value. However, only the isolated far-field pattern coherence matrix estimate agreed well in magnitude and only when the antennas were approximately CMS antennas. If the antennas were not CMS, the matching of the isolated far-field estimate converged as the separation distance increased ($> 0.4\lambda$ for the $\lambda/100$ dipoles investigated.) The other two circuit-parameter estimates were found to decay in magnitude more rapidly than that of the theoretical cross-correlation coefficient. Additionally, the two circuit-parameter estimates were found to depend on the antenna impedance. These results suggest that, as

formulated, the circuit parameter estimates for the correlation coefficient are inaccurate and can not be used during prototype development.

We also showed by simulation in this chapter that if the antenna mutual resistance estimate for the correlation is normalized by the self-resistances with the other antenna present (in contrast to the original definition which normalizes by self-resistances when the antennas are in isolation) the two circuit-parameter estimates are then equivalent.

For theoretical considerations, and since it was found to yield the best correlation estimate, a closed-form expression for the isolated far-field pattern coherence matrix for the particular case of two parallel non-staggered cylindrical dipoles of arbitrary lengths was also given in this chapter. As an example for the use of these closed-form expressions, it was proposed that they can be used to easily generate reference curves to compare against when measuring correlation results with parallel non-staggered dipoles.

Chapter 4

Cross-correlation coefficient estimates between loaded antennas

4.1 Introduction

For diversity systems employing selection, equal-gain, or maximal-ratio combining schemes, as well as Multiple-Input Multiple-Output (MIMO) systems, the voltages across the individual antenna loads depends on the load terminations of all the antenna elements. This dependency complicates designing compact arrays since the cross-correlation of load voltages is then also sensitive to the load terminations. As these systems become more prevalent, it is critical to have simple and accurate means of estimating the load voltage correlations in order to be able to quickly evaluate potential designs. However, in addition to low branch correlations, the mean branch signal strengths should be similar for high diversity gains and each antenna should also have sufficiently high total efficiency.

This chapter begins by presenting a formulation of the cross-correlation coefficient of the antenna terminal load voltages expressed in terms of the open-circuit voltage covariance matrix. This is followed sequentially by the formulations of the three load voltage correlation estimates. We then describe the procedure that was used to evaluate and compare the estimates; firstly describing the numerical simulations of two parallel non-staggered linear dipole antennas, and secondly describing the experimental measurements that were performed using two identical reference sleeve dipoles. The simulation and measurement results for the estimates are then presented; from which it can be seen that estimates trended poorly with the theoretical value. The final sections of the chapter then focus on the mean branch signal strengths and antenna efficiencies. We present results comparing the correlations and total efficiencies for two parallel non-staggered dipoles obtained from both numerical simulations and experimental measurements. From these results we show that the antenna

total efficiencies, and not the correlation coefficient, can become the critical diversity performance metric.

4.2 Theoretical cross-correlation coefficient between loaded antennas

In this section we present a formulation for the theoretical load voltage cross-correlation coefficient based on the formulation in [5]. In the following, it is assumed that the antennas are reciprocal and in a linear reciprocal environment so that relation (2.13) holds between the effective antenna height vector and the far-field transmission pattern of an antenna.

4.2.1 Open-circuit impedance network representation of the load voltage cross-correlation coefficient between loaded antennas

The circuit relations for loaded receive antennas, as shown for antenna element i of an array of N element in Figure 4.1, are given by [23],

$$\mathbf{V_o} = (\mathbf{Z_a} + \mathbf{Z_L})\mathbf{I} \tag{4.1}$$

$$\mathbf{V_L} = \mathbf{Z_L}\mathbf{I} \tag{4.2}$$

where $\mathbf{I}$is the vector of antenna terminal currents, $\mathbf{Z_a}$ is the antenna open-circuit impedance matrix, $\mathbf{Z_L}$ is the load impedance matrix, and $\mathbf{V_o}$and $\mathbf{V_L}$are the vectors of antenna open-circuit voltages and terminal load voltages, respectively. The maximum power transfer theorem [55] implies that for maximum received power,

$$\mathbf{Z_L} = \mathbf{Z_a}^* \quad , \tag{4.3}$$

where $(\cdot)^*$ is the complex conjugate operator. The load voltage covariance matrix, assuming zero mean voltages, is given by,

$$\mathbf{C_L} = \mathbb{E}[\mathbf{V_L}\mathbf{V_L}^\dagger] \quad , \tag{4.4}$$

where $\mathbb{E}[\cdot]$ is the expectation operator and $(\cdot)^\dagger$ is the adjoint operator. From (4.1) and (4.2), the load voltage covariance matrix can be expressed in terms of the impedance networks and the open-circuit

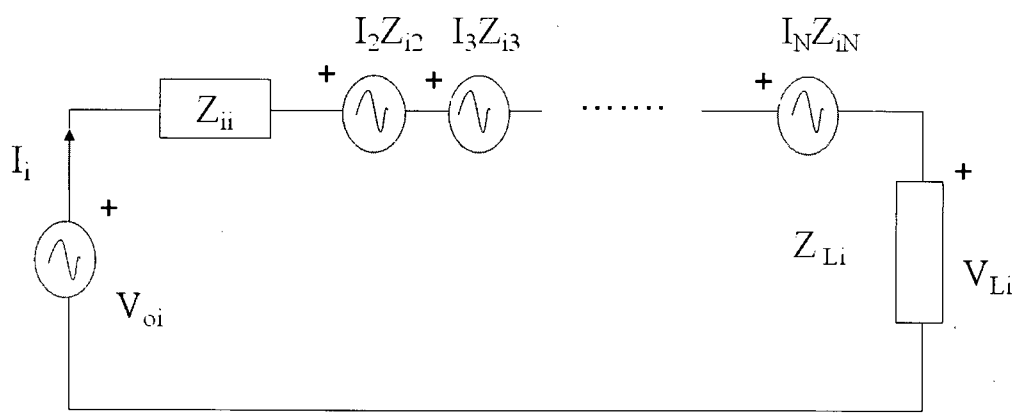

Figure 4.1: The equivalent circuit for antenna i of a N element array which has a diagonal load impedance matrix.

voltage covariance matrix as,

$$\mathbf{C_L} = \mathbb{E}[\mathbf{Z_L}(\mathbf{Z_a}+\mathbf{Z_L})^{-1}\mathbf{V_o}(\mathbf{Z_L}(\mathbf{Z_a}+\mathbf{Z_L})^{-1}\mathbf{V_o})^{\dagger}] \tag{4.5}$$

$$= \mathbf{Z_T}\mathbf{C_o}\mathbf{Z_T}^{\dagger} \tag{4.6}$$

where $\mathbf{Z_T} = \mathbf{Z_L}(\mathbf{Z_a}+\mathbf{Z_L})^{-1}$, and $\mathbf{C_o}$ can be determined from (3.9). The load voltage cross-correlation coefficient between the receiving antennas j and k is then expressed as,

$$\rho_{Ljk} = \frac{\mathbf{C_L}^{(jk)}}{\sqrt{\mathbf{C_L}^{(jj)}\mathbf{C_L}^{(kk)}}} \tag{4.7}$$

where $\mathbf{C_L}^{(ij)}$ is the matrix element in the ith row and j^{th} column of $\mathbf{C_L}$.

4.2.1.1 Impedance representation of loaded-circuit cross-correlation coefficient for Mobile Prototype Scenarios

For MPSs, the loaded-circuit correlation matrix (4.6), using (3.13), reduces to,

$$\mathbf{C_L} = P \oint \mathbf{Z_T} Tr(\mathbf{C_h}) \mathbf{Z_T}^{\dagger}\, d\Omega \tag{4.8}$$

where P is proportional to the incident power, $\mathbf{C_h}$ is the antenna array coherence matrix (2.14), and the matrix trace operator, $Tr(\cdot)$ operates such that $\mathbf{C_h}$ is considered a 2×2 matrices given by (2.14).

Eqn. (4.8) is taken as the theoretical value to which the correlation estimates will be compared against.

4.2.2 *S*-parameter representation of the load voltage cross-correlation coefficient for loaded antennas

As the operation frequencies increases into the microwave range, network representations in terms of S-parameters are better suited for analysis [40]. Recently, a formulation of load voltage cross-correlation coefficients in terms of S-parameters of the antennas, matching network, and loads has been derived [25,56]. Figure 4.2 shows a configuration of an antenna array, with matching, in terms

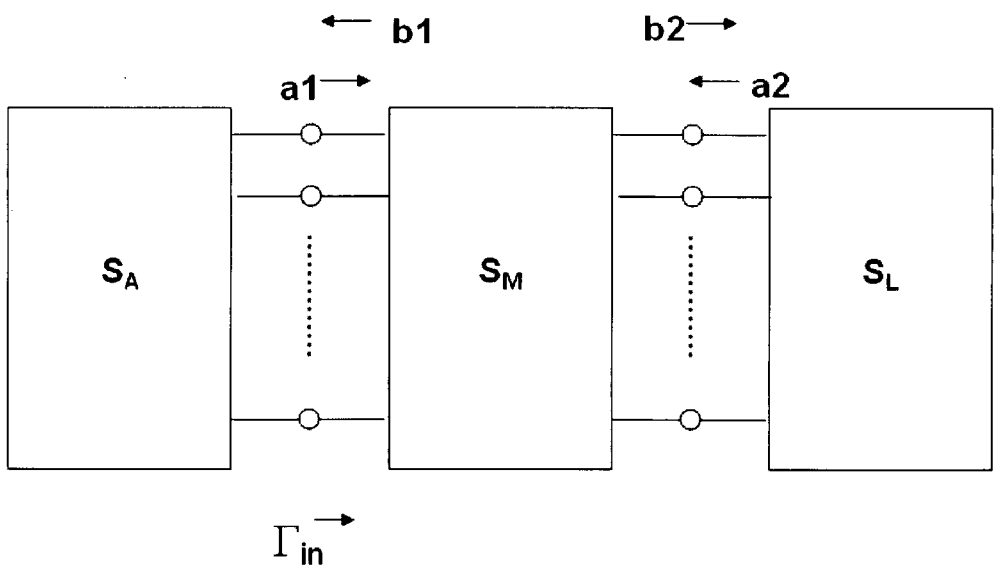

Figure 4.2: S-parameter system model of coupled diversity antenna array connected to a multiport matching network and load network.

of S-parameters. $\mathbf{S}_A$ is antenna array scattering matrix given by (2.25) and $\mathbf{S}_L$ is the terminal load S-parameters. The matching network S-parameters, for the configuration shown in Figure 4.2, can be expressed as,

$$\mathbf{S}_M = \begin{bmatrix} \mathbf{S}_{11} & \mathbf{S}_{12} \\ \mathbf{S}_{21} & \mathbf{S}_{22} \end{bmatrix} . \tag{4.9}$$

The voltage over the loads are given by,

$$\mathbf{V_L} = \sqrt{Z_c}(\mathbf{I} + \mathbf{S}_L)(\mathbf{I} - \mathbf{S}_{22}\mathbf{S}_L)^{-1}\mathbf{S}_{21}(\mathbf{I} - \mathbf{S}_{\alpha\alpha}\mathbf{\Gamma}_{in})^{-1}\mathbf{b}_S \tag{4.10}$$

where $\mathbf{I}$ is the identity matrix, $\mathbf{S}_{\alpha\alpha}$ is given within (2.25) and describes the mutual coupling among the accessible antenna ports, $\mathbf{b}_S = \mathbf{S}_{\alpha\beta}\mathbf{a}_\beta$ also obtained from relation (2.25), Z_c normalization impedance (usually taken as the characteristic impedance of the feed transmission line,) and

$$\mathbf{\Gamma}_{in} = \mathbf{S}_{11} + \mathbf{S}_{12}(\mathbf{I} - \mathbf{S}_L\mathbf{S}_{22})^{-1}\mathbf{S}_L\mathbf{S}_{21} \quad . \tag{4.11}$$

The condition for maximizing received power, equivalent to (4.3), is given by [25],

$$\mathbf{S}_{11} = \mathbf{S}_{\alpha\alpha}^{\dagger} \quad . \tag{4.12}$$

The load voltage covariance matrix is given by,

$$\mathbf{C_L} = \mathbb{E}[\mathbf{V_L}\mathbf{V_L}^{\dagger}] = \mathbf{Q}\mathbf{R}_S\mathbf{Q}^{\dagger} \tag{4.13}$$

where $\mathbf{R}_S = \mathbb{E}[\mathbf{b}_S\mathbf{b}_S^{\dagger}]$ is the covariance matrix of $\mathbf{b}_S$, and

$$\mathbf{Q} = \sqrt{Z_c}(\mathbf{I} + \mathbf{S}_L)(\mathbf{I} - \mathbf{S}_{22}\mathbf{S}_L)^{-1}\mathbf{S}_{21}(\mathbf{I} - \mathbf{S}_{\alpha\alpha}\mathbf{\Gamma}_{in})^{-1} \quad . \tag{4.14}$$

We can express $\mathbf{R}_S$ in terms of the open-circuit voltage covariance matrix in order directly use the approximations derived in Chapter 3. For a receiving antenna array, (2.25) implies,

$$\mathbf{b}_\alpha = \mathbf{S}_{\alpha\alpha}\mathbf{a}_\alpha + \mathbf{S}_{\alpha\beta}\mathbf{a}_\beta \tag{4.15}$$

$$= \mathbf{S}_{\alpha\alpha}\mathbf{a}_\alpha + \mathbf{b}_S \quad . \tag{4.16}$$

When the antenna ports are open-circuited, $\mathbf{a}_\alpha = \mathbf{b}_\alpha$, so (4.16) becomes,

$$\mathbf{a}_\alpha = (\mathbf{I} - \mathbf{S}_{\alpha\alpha})^{-1}\mathbf{b}_S \quad . \tag{4.17}$$

The open-circuit voltage vector can be expressed, using (2.12), (2.28), and (4.17), as,

$$\mathbf{V_o} = 2\sqrt{Z_c}\mathbf{a}_\alpha = 2\sqrt{Z_c}(\mathbf{I} - \mathbf{S}_{\alpha\alpha})^{-1}\mathbf{b}_S \tag{4.18}$$

$$= \oint \mathbf{H}(\Omega)\mathbf{e}_i(\Omega, t)^T \, d\Omega \quad , \tag{4.19}$$

where $(\cdot)^T$ is the transpose operator. From (4.19) we find the expression relating the source wave vector to the vector of effective antenna height vectors,

$$\mathbf{b}_S = \frac{1}{2\sqrt{Z_c}}(\mathbf{I} - \mathbf{S}_{\alpha\alpha}) \oint \mathbf{H}(\Omega)\mathbf{e}_i(\Omega, t)^T \, d\Omega \quad . \tag{4.20}$$

Thus $\mathbf{R}_S$ can be expressed in terms of the open-circuit covariance matrix using (4.18) as,

$$\mathbf{R}_S = \mathbb{E}[\mathbf{b}_S\mathbf{b}_S^\dagger] \tag{4.21}$$

$$= \frac{1}{4Z_c}(\mathbf{I} - \mathbf{S}_{\alpha\alpha})\mathbb{E}[\mathbf{V_o}\mathbf{V_o}^\dagger](\mathbf{I} - \mathbf{S}_{\alpha\alpha})^\dagger \tag{4.22}$$

$$= \frac{1}{4Z_c}(\mathbf{I} - \mathbf{S}_{\alpha\alpha})\mathbf{C_o}(\mathbf{I} - \mathbf{S}_{\alpha\alpha})^\dagger \quad . \tag{4.23}$$

From (4.13) and (4.23), the load voltage covariance matrix can be expressed in terms of the open-circuit voltage covariance matrix and the S-parameters of the antenna array, matching network and load network as,

$$\mathbf{C_L} = \frac{1}{4Z_c}\mathbf{Q}(\mathbf{I} - \mathbf{S}_{\alpha\alpha})\mathbf{C_o}(\mathbf{I} - \mathbf{S}_{\alpha\alpha})^\dagger\mathbf{Q}^\dagger \tag{4.24}$$

where $\mathbf{C_o}$ can be predicted by Eqn. (3.9).

4.2.2.1 *S*-parameter representation of loaded-circuit cross-correlation coefficient for Mobile Prototype Scenarios

For MPSs, the load voltage covariance matrix can be expressed in terms of S-parameters and antenna array coherence matrix by using (3.13) as,

$$\mathbf{C_L} = \frac{P}{4Z_c}\mathbf{Q}(\mathbf{I} - \mathbf{S}_{\alpha\alpha}) \left[\oint Tr(\mathbf{C_h})d\Omega \right] (\mathbf{I} - \mathbf{S}_{\alpha\alpha})^\dagger\mathbf{Q}^\dagger \tag{4.25}$$

where P is proportional to the average incident power, $\mathbf{C_h}$ is the antenna array coherence matrix, and the matrix trace operator, $Tr(\cdot)$ operates such that $\mathbf{C_h}$ is considered a 2×2 matrices given by (2.14).

4.3 Estimations for the load voltage cross-correlation coefficient

In order to avoid time-consuming and expensive field testing or antenna patterns measurements to determine the correlation coefficient, it is imperative that quick and accurate methods be available to estimate the correlation. This section outlines the estimates for the cross-correlation coefficient of the load voltages for Mobile Prototype Scenarios. As seen from (4.8) and (4.25), the methods of estimating the load voltage cross-correlation for MPSs involve the estimation techniques of Chapter 3 for the antenna array coherence matrix $\mathbf{C_h}$; using namely the isolated far-field pattern coherence matrix, the normalized mutual impedance, and the S-parameter estimate.

4.3.1 Isolated far-field pattern estimate for the load voltage cross-correlation covariance matrix

The results from Chapter 3 imply that the array coherence matrix can be estimated by the isolated far-field pattern coherence matrix when the antennas are approximately CMS. Thus, from (4.8), it would then follow that the load voltage covariance matrix can be approximated as,

$$\mathbf{C_L} \approx P\,\mathbf{Z_T}\left[\oint Tr(\mathbf{C_f})d\Omega\right]\mathbf{Z_T}^{\dagger} \tag{4.26}$$

where $\mathbf{Z_T} = \mathbf{Z_L}(\mathbf{Z_a}+\mathbf{Z_L})^{-1}$, and the matrix trace operator, $Tr(\cdot)$ operates such that $\mathbf{C_f}$ is considered a 2×2 matrices given by (2.19).

4.3.1.1 Isolated far-field pattern covariance matrix estimate for $50\,\Omega$ terminated antennas

For antennas terminated to $50\,\Omega$, $\mathbf{Z_L} = 50\,\mathbf{I}$ and the estimate (4.26) becomes proportional to,

$$\mathbf{C_L} \approx (\mathbf{I}+\mathbf{Z_a}')^{-1}\left[\oint Tr(\mathbf{C_f})d\Omega\right]((\mathbf{I}+\mathbf{Z_a}')^{-1})^{\dagger} \tag{4.27}$$

where $\mathbf{Z_a}' = \mathbf{Z_a}/50$.

4.3.2 Normalized mutual impedance estimate for the load voltage cross-correlation coefficient

From (4.8) and (3.26) it follows that the load voltage covariance matrix can be approximated in terms of impedance network parameters for the antennas and the load circuit as

$$\mathbf{C_L} \approx P\,\mathbf{Z_T}\mathbf{R_a}\mathbf{Z_T}^{\dagger} \tag{4.28}$$

where $\mathbf{R_a}$ =Re($\mathbf{Z_a}$) except that R_{ii} is the real part of the self-resistance of antenna i when it is in isolation; again this condition on the self-resistances R_{ii} stems from Eq.(2.32).

4.3.2.1 Normalized mutual resistance estimate for $50\,\Omega$ terminated antennas

The normalized mutual impedance estimate (4.28) for identical $50\,\Omega$ terminated antennas is proportional to,

$$\mathbf{C_L} \approx (\mathbf{I} + \mathbf{Z_a}')^{-1}\,\mathbf{R_a}\,((\mathbf{I} + \mathbf{Z_a}')^{-1})^{\dagger} \quad . \tag{4.29}$$

4.3.3 *S*-parameter estimation for the load voltage cross-correlation coefficient

From Eqn. (4.25) and (3.35), the loaded voltage covariance matrix is expressed in terms of only the *S*-parameters of the antenna array, the matching network, and load network as,

$$\mathbf{C_L} \approx P\mathbf{Q}(\mathbf{I} - \mathbf{S}_{\alpha\alpha})(\mathbf{I} - \mathbf{S}_{\alpha\alpha}^{T})^{-1}(\mathbf{I} - \mathbf{S}_{\alpha\alpha}^{T}\mathbf{S}_{\alpha\alpha}^{*})(\mathbf{I} - \mathbf{S}_{\alpha\alpha}^{*})^{-1}(\mathbf{I} - \mathbf{S}_{\alpha\alpha})^{\dagger}\mathbf{Q}^{\dagger} \quad . \tag{4.30}$$

This estimate [25] is more general than the previous works [24,57,58] which have presented (4.30) in the less general case of matched antennas. For reciprocal networks, (4.30) simplifies to,

$$\mathbf{C_L} \approx P\mathbf{Q}(\mathbf{I} - \mathbf{S}_{\alpha\alpha}\mathbf{S}_{\alpha\alpha}^{*})\mathbf{Q}^{\dagger} \tag{4.31}$$

4.3.3.1 S-parameter estimate for $50\,\Omega$ terminated antennas

For $50\,\Omega$ load terminations, the S-parameter method estimate for the load voltage covariance matrix, using $\mathbf{\Gamma}_{in} = \mathbf{0}$ from (4.11) and $\mathbf{Q} = \mathbf{I}$ from (4.14), is given by (4.30) as,

$$\mathbf{C_L} = \left(\frac{\lambda^2 P}{Z}\right)(\mathbf{I} - \mathbf{S}_{\alpha\alpha})(\mathbf{I} - \mathbf{S}_{\alpha\alpha}^T)^{-1}(\mathbf{I} - \mathbf{S}_{\alpha\alpha}^T\mathbf{S}_{\alpha\alpha}^*)(\mathbf{I} - \mathbf{S}_{\alpha\alpha}^*)^{-1}(\mathbf{I} - \mathbf{S}_{\alpha\alpha})^\dagger \quad . \tag{4.32}$$

For example, for two element reciprocal antenna array, using (4.7) and (4.32), the S-parameter estimate for the load voltage cross-correlation coefficient becomes the commonly used expression,

$$\rho_{L12} \approx \frac{|s_{11}^* s_{12} + s_{21}^* s_{22}|^2}{(1 - |s_{11}|^2 - |s_{21}|^2)(1 - |s_{22}|^2 - |s_{12}|^2)} \quad . \tag{4.33}$$

4.4 Comparison of the estimates for the load voltage cross-correlation coefficient

In order to compare the estimates for the cross-correlation coefficient between the antenna terminal load voltages we performed numerical simulations and experimental measurements with parallel non-staggered dipole antennas. A similar procedure to that was used in the investigation of open-circuit voltage correlation was performed: for each separation distance we obtained the effective antenna heights and S-parameters for two $50\,\Omega$ terminated $\lambda/2$ dipole antennas, and the isolated far-field patterns were obtained by exciting an isolated dipole by a $50\,\Omega$ source. The open-circuit impedance matrices used to determine the theoretical and the estimates correlations were derived from S-parameters using relation (2.27). The theoretical value of the correlation between the load voltage were determined using Eqn.(4.7) and (4.8). The isolated far-field pattern, normalized mutual impedance, and S-parameter estimates for the load covariance matrix were determined using Eqns.(4.27),(4.29), and (4.32), respectively.

4.4.1 Numerical simulations

To compare the estimates for the cross-correlation coefficient of antenna load voltages under ideal conditions two identical parallel side-by-side cylindrical $\lambda/2$ dipoles were simulated using CST Microwave Studio. We performed two different simulation sets to investigate the assumptions based

on the antennas being Canonical Minimum Scattering: the first simulation set used dipoles with radii $= \lambda/100$ and second set used dipoles with radii $= \lambda/1000$. Appendix D shows the figures of the simulation models and tables with the simulation settings. Plots of the self and mutual impedances are shown in Appendix E for both sets dipole thicknesses. From these impedance plots, one can see that the $r = \lambda/1000$ dipole will be approximately CMS as indicated from the low fluctuation of the self-resistance. The data was processed using MATLAB.

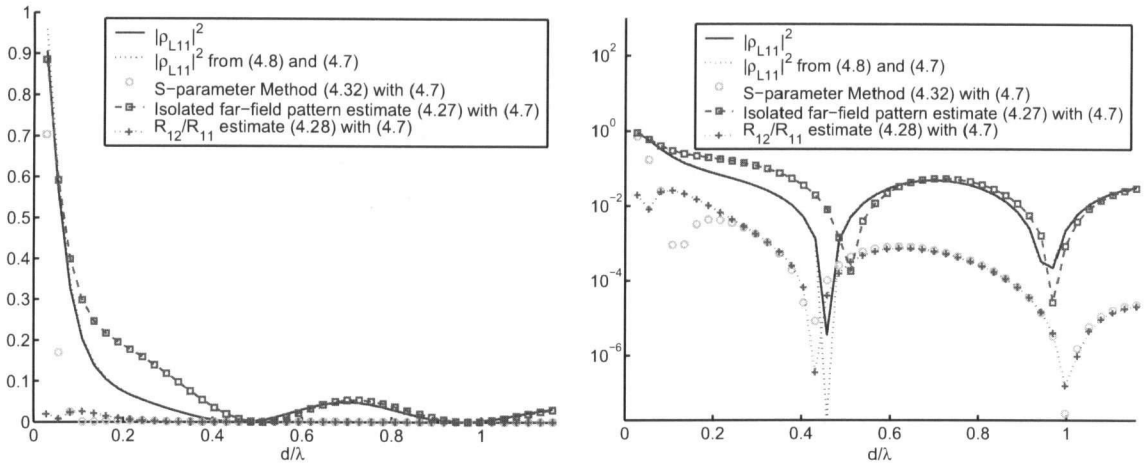

(a) Linear scale (b) Log scale

Figure 4.3: Load voltage cross-correlation coefficient predictions methods from CST simulation for 50 Ω load terminated cylindrical dipoles of radii $\lambda/100$

The simulation results for the different estimates of the load voltage cross-correlation coefficient for dipoles of radii of $\lambda/100$ and $\lambda/1000$ can be seen in Figures 4.3 and 4.4, respectively. From these figures it can be seen that the cross-correlation coefficient of the load voltages quickly decreases below a value of 0.5 for separation distances greater than 0.1λ. This would imply that it should be fairly easy to design load terminated antennas which have low signal correlation when they are deployed in high scattering environments. It can also be seen that how well the two circuit-parameter estimates trended with the theoretical value was dependent on the antenna thicknesses and on the antenna relative effective lengths. By calculating the correlation estimates at a different frequency, the S-parameter and normalized mutual resistance estimates were found to varying significantly. Figure 4.5 shows sample results for the $\lambda/100$ dipoles simulated at 808 MHz and 884 MHz and illustrates the sensitivity of the circuit-parameters to antenna impedances. Further simulation results comparing the estimates at different frequencies are shown in Appendix H. The isolated

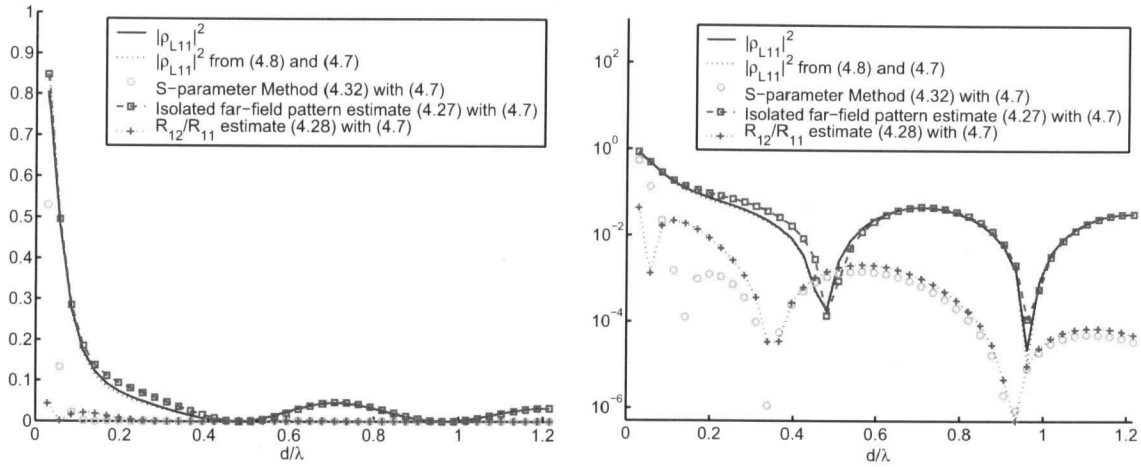

(a) Linear scale

(b) Log scale

Figure 4.4: Load voltage cross-correlation coefficient predictions methods from CST simulation for 50 Ω load terminated cylindrical dipoles of radii $\lambda/1000$

far-field patterns coherence estimate was found to trends well with the theoretical value. The match between the isolated far-field pattern estimate and the theoretical value was found to converge as the separation distance increased. The convergence was in a function of how well the antennas approximate MS. This can be inferred by comparing the convergence between the thick and thin dipoles simulations: estimate for the thin dipoles matched for essentially all separation distances whereas the dipoles were found to converged for separation distance $d/\lambda > 0.6$.

As seen in Chapter 3, the S-parameter and normalized mutual resistance estimates match closely to each other. The discrepancy between the S-parameter and normalized mutual resistance estimates for small separation distances stems from the original definition of the normalized mutual resistance (2.32). In this definition, the mutual resistance is normalized by the self-impedances of the antennas in isolation. If the mutual resistance is normalized by the self-impedances of the antennas (with the other antenna present) the S-parameter and normalized mutual resistance estimates match exactly; as shown in Appendix G.

These simulation results indicate that the isolated far-field patterns coherence matrix can be used to estimate the theoretical load voltage cross-correlation coefficient between thin dipoles or likely antennas that well approximate MS antennas. Our results also show that the known circuit-parameter estimates for the cross-correlation coefficient are inaccurate and are very sensitive to antenna impedance.

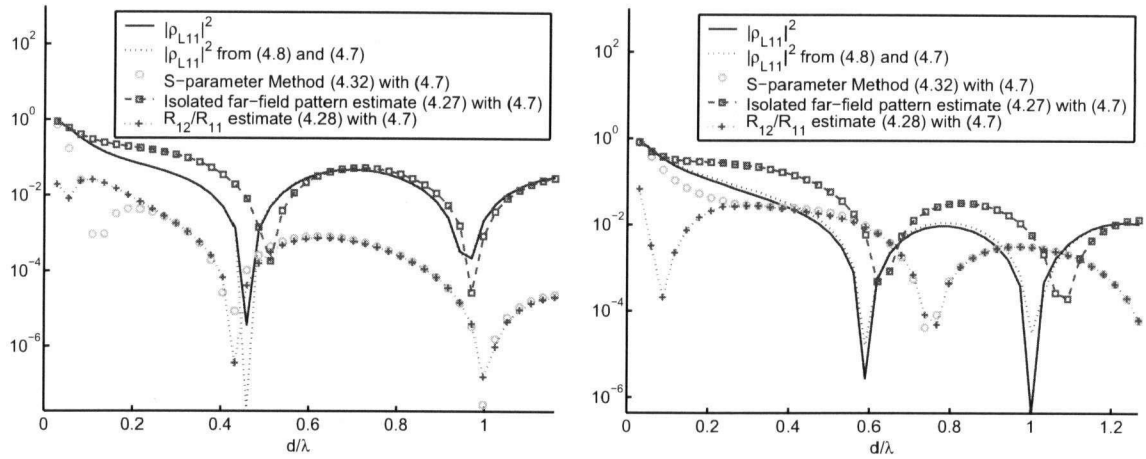

(a) $\lambda/100$ dipole calculated at 808 MHz.

(b) $\lambda/100$ dipole calculated at 884 MHz.

Figure 4.5: Effect of evaluating the load voltage correlation coefficient estimates for different frequencies (808 MHz and 884 MHz) for $r = \lambda/100$ dipoles. Results based on numerical simulations using CST (log scale.) The circuit-parameter estimates are seen to vary greatly as a function of evaluation frequency; in contrast to the field pattern correlations.

4.4.2 Experimental measurements

The correlation estimates for the antenna terminal load voltages were also compared from data collected by experimental measurements. We obtained the S-parameters and three dimensional complex antenna patterns for two identical parallel side-by-side Satimo reference sleeve dipoles. The Satimo reference sleeve dipoles were designed by Satimo for use as a precision gain reference for low-gain antenna measurements and chamber reflectivity evaluation. The end-fed sleeve dipole technology minimizes cable and feed point interaction. The integrated choke design further reduces cable interaction by attenuating the natural return currents from the dipole. The highly symmetric design meets and exceeds the 0.1 dB azimuth variation specified by the CTIA. The Satimo sleeve dipoles had centre frequencies at 945 MHz and had an input impedance of 50 Ω when in isolation. The antenna pattern measurement system was built in-house at NOKIA, and its accuracy was verified using the auto-correlation coefficients of dipole antennas [51]. A sample of the experimental arrangement of the dipoles can be seen in Appendix J.

We measured the 3D complex antenna patterns, as a function of separation distance, by driving one dipole while the other was terminated with a 50 Ω load. The S-parameters of the Satimo dipoles, as a function of separation distance, was also measured within the anechoic chamber. The

raw antenna pattern and S-parameter data were processed using MATLAB. Plots of the measured self and mutual impedances, as a function of separation distance, for the Satimo sleeve dipoles are shown in Appendix K. One can predict from these impedance plots that the dipoles will poorly approximate CMS antennas; as indicated from the high fluctuations of the self-resistance as discussed in Section 2.3.5.

The derived cross-correlation coefficients estimates for the antenna terminal load voltages based on the experimental measurement can be seen in Figure 4.6. This figure shows that the cross-correlation coefficient was found to be practically negligible for all separation distances. These low values can be accounted for by the large pattern deformations as shown in Appendix L.

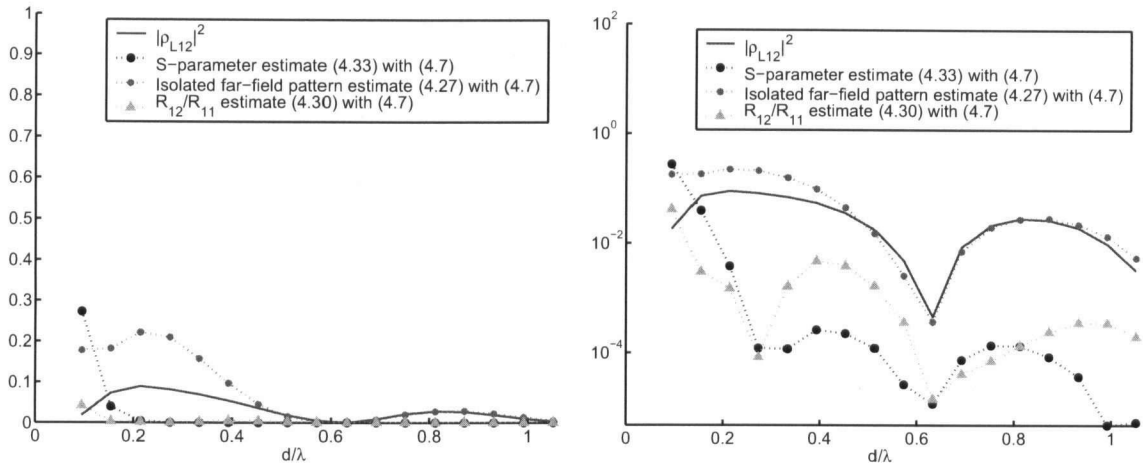

(a) Linear scale (b) Log scale

Figure 4.6: Load voltage cross-correlation coefficient predictions methods obatined from measurement of Satimo sleeve dipoles for 50 Ω load termination.

Figure 4.6 also shows that the S-parameter and normalized mutual resistance estimates derived from experimental measurements trend poorly with the theoretical estimate for separation distances less than 0.4λ. This result agrees with the results obtained from the numerical simulations as shown in Section 4.4.1. The experimental measurement results also agree the simulation results on the good trend and matching of the isolated far-field pattern coherence estimate with the theoretical value. The matching of the isolated far-field pattern estimate was worse than the simulation results for separation distance less than 0.4λ; this result can be account for by recognizing the Satimo dipoles scatter more as inferred from the fluctuation in the self-resistance. These results again suggest that only the isolated far-field pattern coherence matrix can be used to estimate the

load-voltage cross-correlation coefficient when the antennas are approximately Minimum Scattering antennas.

4.5 Other performance factors for multiple antenna systems in Mobile Prototype Scenarios

In this section we consider two additional important performance factors for multiple antenna systems: (1) the relative mean branch signal-to-noise levels should be similar for high diversity gains [1] and (2) the total efficiency of antennas used should be sufficiently high for mobile devices. We show that for MPSs these two performance metrics converge to antenna total efficiency. We compare the efficiencies and cross-correlation coefficients for two parallel non-staggered dipoles obtained from numerical simulation and experimental measurements and show that the antenna efficiencies will likely be the design challenge for multiple antenna designs. This result is in contrast to the disproportionate emphasis in the literature on the cross-correlation coefficient rather than the efficiency when investigating multiple antenna designs.

4.5.1 Estimates of mean branch signal strength for MPSs

As the Mean Effective Gain is a measure for the mean branch signal level, antenna designers should ensure that the MEG are roughly similar and maximized for each diversity antenna. Under conditions of the Mobile Prototype Scenario, a simple expression for the MEG of lossless antennas can be obtained from S-parameters alone. For MPSs, Eqn. (2.39) for the MEG reduces to,

$$G_e = \eta/2 \quad , \tag{4.34}$$

where η_T is the total antenna efficiency. Thus, for Mobile Prototype Scenarios, to ensure similar branch signal strengths the total efficiency of each antennas should be similar.

4.5.1.1 Mean Effective Gain estimates for MPSs from S-parameters

For scenarios were the antennas can be considered lossless and are operated in a lossless environment the total and radiation efficiencies can be estimated from S-parameters,

$$\eta_T = \frac{P_{rad}}{P_{inc}} \cong 1 - |S_{11}|^2 - |S_{21}|^2 \tag{4.35}$$

$$\eta_{rad} = \frac{P_{rad}}{P_{in}} = \frac{\eta_T}{1 - |S_{11}|^2} \tag{4.36}$$

where η_{rad} is the radiation efficiency, P_{rad} is the radiated power, P_{inc} is the incident power, P_{in} is the power accepted by antenna 1, and S_{ij} are the scattering parameters. For practical designs of handheld devices, the antennas are always lossy and operate in lossy environments so the estimates (4.35) and (4.36) should not be used if accurate performance gauge is sought.

4.5.2 Total efficiencies of closely spaced antennas

Although the condition of having similar mean signal strengths is necessary for optimizing multiple antenna systems, it is also essential to have high total efficiencies; for example, battery lifetime is a critical performance factor for mobile devices. Typically, as antennas move closer in proximity, their coupling increases and thereby yields lower radiative performance. To compare the total efficiencies and the cross-correlation between the load voltages, experimental measurements and numerical simulations were performed for parallel non-stagger $\lambda/2$ dipoles as a function of separation distance.

4.5.2.1 Simulation and measured total efficiencies for $\lambda/2$ dipoles

The total and radiation efficiencies for two parallel side-by-side Satimo sleeve $\lambda/2$ dipoles (centre frequency at 884 MHz and matched to 50 Ω when in isolation) as function of separation distance were determined by CST simulation and experimental measurement [59]. Figures of the CST models of the Satimo sleeve dipoles can be seen in Fig. D.3 and D.4 in Appendix D. The total and radiated efficiencies can be seen in Fig. 4.7.

As shown in Fig. 4.7, there is a large decrease in total efficiency as the separation distance decreases. A comparison between radiation and total efficiencies indicate that the losses are primar-

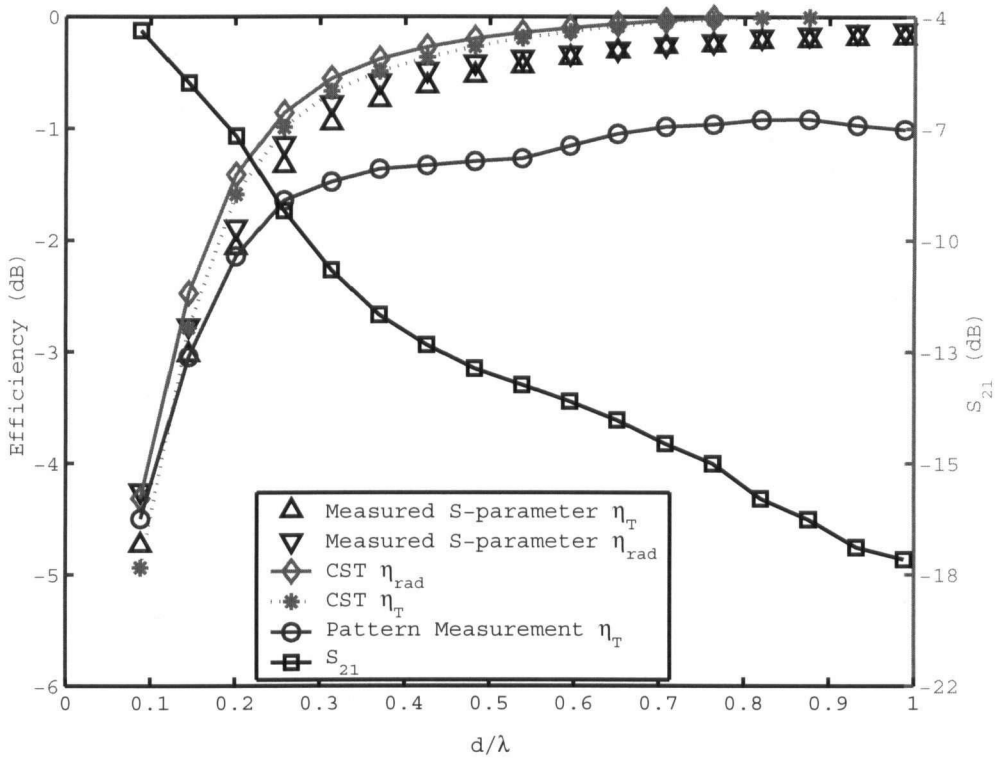

Figure 4.7: Measured and simulation results for the total and radiation efficiencies of 884 MHz Satimo sleeve dipoles.

ily within the parasitic 50 Ω load and not due to detuning. In this case, since the loss in efficiency is due primarily to coupling, the coupling S-parameters can be used as a design measure for efficiency. For example, as shown in Fig. 4.7, for $S_{21} < -10$ dB the efficiency is found to be within 10-15% of its peak value.

Upon comparing the load voltage cross-correlation coefficients from Fig. 4.6 and the total efficiencies from Fig. 4.7 the results indicate that the loss of efficiency, rather than the cross-correlation coefficient, can be the critical performance measure for multiple antenna systems. When antennas are closely spaced, one cannot design only for the standard low cross-correlation measure of $\rho < 0.7$ alone, as the total efficiency may be the detrimental performance factor.

4.6 Discussion

Unlike the results presented in Chapter 3 for estimating the open-circuit voltage correlation, numerical simulation showed that only the isolated far-field pattern coherence estimate trended well with

the theoretical values for the cross-correlation coefficient between 50Ω terminated dipole antennas. By comparing the numerical simulation results for the different dipole radii of $\lambda/1000$ and $\lambda/100$, it was found that the isolated far-field pattern coherence estimate improved in accuracy as the antennas better approximated the MS condition. How well an antenna approximates the MS condition can be inferred from the fluctuation in the self-resistance; the lower the relative fluctuation the better the MS approximation.

It was showed by simulation and experiment results that if the antenna mutual resistance estimate for the correlation is normalized by the self-resistances with the other antenna present (in contrast to the original definition which normalizes by self-resistances when the antennas are in isolation) the two circuit-parameter estimates are then equivalent. These circuit-parameter estimates were found to poorly match the theoretical load voltage correlation and were very sensitive to the antenna impedance (see Appendix H). It should be noted that both the theoretical and estimates of the measured load voltage coefficient were practically insignificant for all separation distances.

These results suggest that the known circuit-parameter estimates are inaccurate for the correlation between load voltages and that only the isolated far-field pattern coherence estimates can be used when estimating approximately MS antennas. However, as the isolated far-field pattern coherence estimate is not a circuit parameter estimate, it is of little value for quickly evaluating potential multi-antenna designs. The isolated far-field pattern coherence estimate does have the virtue of applicability for arbitrary incident field distributions; thus allowing for rough performance estimates via quick non-electromagnetic simulations.

Although the cross-correlation coefficient is heavily emphasized in the literature on multiple antenna systems, it was shown that the antenna total efficiencies can be the critical performance factor of multiple antenna systems. From both the numerical simulations and experimental measurements using two $50\,\Omega$ terminated $\lambda/2$ dipoles, the cross-correlation coefficient was found to be practically insignificant for separation distances greater than 0.1λ whereas the total efficiencies decrease by as much as 4 dB due to coupling into the parasitic element. These results suggest that the likely challenge of design compact multiple antenna devices will be to place the antennas so that they similar and maximized MEG.

Chapter 5

Conclusions and Recommendations

5.1 Conclusion

The goal of this thesis was to evaluate and compare known methods for estimating the cross-correlation coefficient for closely spaced antennas. Sufficiently low branch cross-correlation is necessary to maximize the potential gains of diversity/MIMO antenna systems. Fast and efficient means are thus required to estimate the cross-correlation coefficients in order to evaluate potential antenna designs. Establishing the limitations of the known cross-correlation coefficient estimates is crucial for antenna designers who are designing diversity/MIMO antennas. Although the estimates for the cross-correlation coefficient have been established prior to this work, no inter-comparisons and very few measurement-based comparisons of the estimates have been made [57, 58].

In Chapter 3, we compared the estimates for the cross-correlation coefficient between the open-circuit voltages by numerical simulations. Although all three of the known estimates trended well with the theoretical value, only the isolated far-field pattern coherence matrix estimate agreed well in magnitude. As the separation distance increased the other two estimates were found to decay in magnitude more rapidly than that of the theoretical cross-correlation coefficient. A comparison between the two sets of simulations with dipoles of different radii ($\lambda/1000$ and $\lambda/100$) indicated that the isolated far-field pattern estimate improved in accuracy as the radii decreased; as expected as the antennas better approximated CMS antennas for smaller radii. These results suggest that all three estimates can be used to predict the open-circuit voltage correlation during prototype development; when using these estimates one can simply set a more stringent design threshold for the cross-correlation rather than targeting the usual measure of below 0.5. As the isolated far-field pattern coherence was shown be to the most accurate estimate, it should be mentioned that the method is not based on circuit parameters and would work best for antennas whose patterns are easy to

predict; an unlikely scenario for most mobile devices. For theoretical considerations, and due to its canonical nature in applications, we derived a closed-form expression for two parallel non-staggered linear filament dipoles of arbitrary lengths. These closed-form expressions potentially facilitate further tractability in theoretical formulations and also simplify the generation of correlation reference curves.

In Chapter 4, we compared the estimates for the correlation between antenna load voltages by numerical simulations and experimental measurements using 50 Ω terminated dipole antennas. The numerical simulation results revealed that the isolated far-field pattern coherence was the only estimate that trended the theoretical values for all cases and matched well when the antennas were approximately MS. Through numerical simulations and experimental measurements, we showed that the two circuit-parameter estimates are equivalent. These circuit-parameter estimates were found to poorly match the theoretical values for all the cases investigated and poorly trended for most separation distances. These results suggest that no accurate circuit-parameter estimate exists for the correlation between load voltages between non-MS antennas and that only the isolated far-field pattern coherence estimates can be used when the antennas are approximately MS. However, it is not likely that antenna designers can estimate diversity antenna performance without the use of a three dimensional complex antenna pattern measurement system since the isolated far-field pattern coherence is not based on circuit parameter measurements.

Additionally in Chapter 4, we showed that for Mobile Prototype Scenarios the Mean Effective Gain is equivalent to the antenna total efficiency. This is an important consideration as the MPS is the incident field scenario assumed when formulating the circuit parameter estimates for the correlation. Although the cross-correlation coefficient is heavily emphasized in the literature on diversity/MIMO systems, it was shown that the antenna total efficiencies can be the critical performance factor. From both the numerical simulations and experimental measurements of two 50 Ω terminated $\lambda/2$ dipoles, the correlation was found to be practically insignificant for separation distances greater than 0.1λ whereas at that separation distance the total efficiencies decrease by 4 dB due to coupling into the parasitic element. These results suggest that the likely challenge of designing compact multiple antenna devices will be to obtain sufficient total antenna efficiencies.

5.2 Recommendations

The findings from this thesis suggest that the estimates for the cross-correlation coefficient, specifically the correlation between the load voltages, are imprecise. As such, antenna designers will likely require making three dimensional complex antenna pattern measurements to completely evaluate potential diversity/MIMO antenna designs. However, as it was shown that the total efficiencies, rather than the correlations, can be the limiting performance metric, it is recommended that antenna designers first optimize the total efficiency of each antenna and, once sufficiently high, then verify that the correlation is sufficiently low.

Our results reveal the need for a more accurate estimate for the correlation between antenna load voltages. This finding is in agreement with recent publications that have tried to improve the circuit-based estimates for the correlation [48, 60, 61]. The discrepancies of the cross-correlation coefficient estimates indicate that (1) the performance of the normalized mutual resistance estimate is sensitive to it's assumption of requiring Minimal Scattering antennas and (2) there seems to be inaccuracies in the assumption of the S-parameter formulation; likely stemming from their expressions for the total radiated field in terms of the antenna parameters and implicitly assuming single current mode antennas. Our results showed that the trends of the circuit parameter estimates to the theoretical values has large variation when evaluated at different frequencies. Future work could determine the cause of this trending variation and this could lead to further improvements to the circuit parameter estimates. However, as it was shown that the efficiencies could be more critical then the cross-correlation coefficient, it would be prudent not only to improve the cross-correlation coefficient estimates but to develop a composite metric incorporating both correlation and mean signal strengths, for example those shown in [1], and the corresponding associated practical estimates for this composite metric.

Future work could also include an investigation into the accuracy of the correlation estimates for realistic incident field distributions. However, it would be a challenging design task to compare the correlation estimates obtained by experimental measurements for different realistic incident field distributions. One would be required to first accurately characterize the incident field distribution, measure the signal correlations, and finally obtain and compare the estimates. It is interesting, and important to emphasize, that the isolated far-field pattern coherence is the only correlation estimate

which applies to general incident field distributions.

Lastly, the concept of using the auto-correlation to evaluate and diagnose an antenna measurement system could be pursued. The auto-correlation of a dipole could be measured and compared against the closed-form expression presented in Chapter 3. One could then introduce known errors into the system to determine their effect on the measured auto-correlation curve.

Bibliography

[1] M. Schwartz, W. R. Bennett, and S. Stein, *Communication Systems and Techniques*. New York: IEEE Press, 1996.

[2] W.C. Jakes Jr., *Microwave Mobile Communications*. New York: Wiley, 1974.

[3] G. Foschini and M. Gans, "On limits of wireless communications in a fading environment when using multiple antennas," *Wireless Personal Commun.*, vol. 6, pp. 311–335, 1998.

[4] J. K. Cavers, *Mobile Channel Characteristics*. Boston, MA : Kluwer Academic, 2000.

[5] R. Vaughan and J. B. Andersen, *Channels, Propagation and Antennas for Mobile Communications*. London: IEE, 2003, ch. 2,6, and 8.

[6] J. Luo, J. R. Zeidler, and S. McLaughlin, "Performance analysis of compact antenna arrays with MRC in correlated Nakagami fading channels," *IEEE Trans. Veh. Technol.*, vol. 50, no. 1, pp. 267–277, Jan. 2001.

[7] P. Lombardo, D. Fedele, and M. M. Rao, "MRC performance for binary signals in Nakagami fading with general branch correlation," *IEEE Trans. Commun.*, vol. 47, pp. 44–52, Jan. 1999.

[8] Q. T. Zhang, "Maximal-ratio combining over Nakagami fading channels with an arbitrary branch covariance matrix," *IEEE Trans. Veh. Technol.*, vol. 48, pp. 1141–1150, July 1999.

[9] S. Ko and R. Murch, "A diversity antenna for external mounting on wireless handsets," *IEEE Trans. Antennas Propag.*, vol. 49, no. 5, pp. 840–842, May 2001.

[10] ——, "Compact integrated diversity antenna for wireless communications," *IEEE Trans. Antennas Propag.*, vol. 49, no. 6, pp. 954–960, June 2001.

[11] K. Ogawa, T. Matsuyoshi, and K. Monma, "An analysis of the performance of a handset diversity antenna influenced by head, hand, and shoulder effects at 900 MHz: Part II - Correlation characteristics," *IEEE Trans. Veh. Technol.*, vol. 50, no. 3, pp. 845–853, May 2001.

[12] B. Green and M. Jensen, "Diversity performance of dual-antenna handsets near operator tissue," *IEEE Trans. Antennas Propag.*, vol. 48, no. 7, pp. 1017–1024, July 2000.

[13] C. Braun, G. Engblom, and C. Beckman, "Evaluation of antenna diversity performance for mobile handsets using 3-D measurement data," *IEEE Trans. Antennas Propag.*, vol. 47, no. 11, pp. 1736–1738, Nov. 1999.

[14] C. Braun, M. Nilsson, and R. Murch, "Measurement of the interference rejection capability of smart antennas on mobile telephones," in *Proc. IEEE VTC*, vol. 2, May 1999, pp. 1068–1073.

[15] J. Colburn, Y. Rahmat-Samii, M. Jensen, and G. Pottie, "Evaluation of personal communications dual-antenna handset diversity performance," *IEEE Trans. Veh. Technol.*, vol. 47, no. 3, pp. 737–746, Aug. 1998.

[16] M. LeFevre, M. Jensen, and M. Rice, "Indoor measurement of handset dual-antenna diversity performance," in *Proc. IEEE VTC*, vol. 3, May 1997, pp. 1763–1767.

[17] M. Douglas, M. Okoniewski, and M. Stuchly, "A planar diversity antenna for handheld PCS devices," *IEEE Trans. Veh. Technol.*, vol. 47, no. 3, pp. 747–754, Aug. 1998.

[18] N. Scott, M. Leonard-Taylor, and R. Vaughan, "Diversity gain from a single-port adaptive antenna using switched parasitic elements illustrated with a wire and monopole prototype," *IEEE Trans. Antennas Propag.*, vol. 47, no. 2, pp. 1066–1070, June 1999.

[19] R. Vaughan, "Switched parasitic elements for antenna diversity," *IEEE Trans. Antennas Propag.*, vol. 47, no. 2, pp. 399–405, Feb. 1999.

[20] 3GPP (Third Generatio Partnership Project) Home Page, http://www.3gpp.org/.

[21] CDMA Development Group - Technology, http://www.cdg.org/technology/.

[22] R. E. Collin and F. Zucker, *Antenna Theory: Part 1*. New York: McGraw-Hill, 1969, ch. 4.

[23] R. Vaughan and J. Andersen, "Antenna diversity in mobile communications," *IEEE Trans. Veh. Technol.*, vol. 36, no. 4, pp. 149–172, Nov. 1987.

[24] S. Blanch, J. Romeu, and I. Corbella, "Exact representation of antenna system diversity performance from input parameter description," *Elec. Lett.*, vol. 39, no. 9, pp. 705–707, May 2003.

[25] J. W. Wallace and M. A. Jensen, "Termination-dependent diversity performance of coupled antennas: Network theory analysis," *IEEE Trans. Antennas Propag.*, vol. 52, no. 1, pp. 98–105, Jan. 2004.

[26] R. E. Collin and F. Zucker, *Antenna Theory: Part 1*. New York: McGraw-Hill, 1969, p. 130.

[27] *IEEE Standard Test Procedures for Antennas*. New York: IEEE, 1979.

[28] S. Kozono, H. Tsuruhata, and M. Sakamoto, "Base station polarization diversity reception for mobile radio," *IEEE Trans. Veh. Technol.*, vol. 33, no. 4, pp. 301–306, 1984.

[29] S. A. Bergmann and H. W. Arnold, "Polarization diversity in portable communications environment," *Elec. Lett.*, vol. 22, no. 11, pp. 609–610, 1986.

[30] T. Taga, "Analysis for mean effective gain of mobile antennas in land mobile radio environments," *IEEE Trans. Veh. Technol.*, vol. 39, no. 2, pp. 117–131, May 1990.

[31] W. C. Y. Lee and Y. S. Yeh, "Polarization diversity system for mobile radio," *IEEE Trans. Commun.*, vol. 20, no. 5, pp. 912–923, 1972.

[32] K. Ogawa and T. Matsuyoshi, "An analysis of the performance of a handset diversity antenna influenced by head, hand, and shoulder effects at 900 MHz:part I - Effective gain characteristics," *IEEE Trans. Veh. Technol.*, vol. 50, no. 3, pp. 830–844, May 2001.

[33] R. Vaughan, "Polarization diversity in mobile communications," *IEEE Trans. Veh. Technol.*, vol. 39, no. 3, pp. 177–186, Aug. 1990.

[34] W. C. Y. Lee and R. H. Brandt, "The elevation angle of mobile radio signal arrival," *IEEE Trans. Commun.*, vol. 21, no. 11, pp. 1194–1197, 1973.

[35] G. Sinclair, "The transmission and reception of elliptically polarized antennas," *Proc. IRE*, vol. 38, pp. 148–151, Feb. 1950.

[36] C. Montgomery, R. Dicke, and E. Purcell, *Principles of Microwave Circuits*. New York: McGraw-Hill, 1948, pp. 317–333.

[37] W. K. Kahn and H. Kurss, "Minimum-scattering antennas," *IEEE Trans. Antennas Propag.*, vol. 13, pp. 671–675, Sept. 1965.

[38] W. K. Kahn and W. Wasylkiwskyj, "Theory of coupling, radiation, and scattering by antennas," in *Proc. Symp. Generalized Networks*, vol. 16, 1966, pp. 83–114.

[39] A. G. J. Gately, D. J. R. Stock, and B. Ru-Schao Cheo, "A network description for antenna problems," *Proc. IEEE*, vol. 56, no. 7, pp. 1181–1193, July 1968.

[40] D. M. Pozar, *Microwave Engineering*, 3rd ed. Hoboken, NJ: Wiley, 2005.

[41] J. Bach Andersen, H. A. Lessow, and H. Schjaer-Jacobsen, "Coupling between minimum scattering antennas," *IEEE Trans. Antennas Propag.*, vol. 22, no. 6, pp. 832–835, Nov. 1974.

[42] W. Wasylkiwskyj and W. K. Kahn, "Scattering properties and mutual coupling of antennas with prescribed radiation pattern," *IEEE Trans. Antennas Propag.*, vol. 18, no. 6, pp. 741–752, Nov. 1970.

[43] ——, "Theory of mutual coupling among minimum-scattering antennas," *IEEE Trans. Antennas Propag.*, vol. 18, no. 2, pp. 204–216, Mar. 1970.

[44] ——, "Mutual coupling and element efficiency for infinite linear arrays," *Proc. IEEE*, vol. 56, pp. 1901–1907, Nov. 1968.

[45] R. H. Clarke, "A statistical theory of mobile-radio reception," *Bell Sys. Tech. J.*, vol. 47, pp. 957–1000, July 1968.

[46] X. Li and Z.-P. Nie, "Mutual coupling effects on the performance of MIMO wireless channels," *IEEE Antennas Wireless Propag. Lett.*, vol. 3, pp. 344–347, 2004.

[47] ——, "Effect of array orientation on performance of MIMO wireless channels," *IEEE Antennas Wireless Propag. Lett.*, vol. 3, pp. 368–371, 2004.

[48] H. T. Hui, W. Yong, and K. Toh, "Signal correlation between two normal-mode helical antennas for diversity reception in a multipath environment," *IEEE Trans. Antennas Propag.*, vol. 52, no. 2, pp. 572–577, Feb. 2004.

[49] M. Jensen and Y. Rahmat-Samii, "Performance analysis of antennas for hand-held transceivers using FDTD," *IEEE Trans. Antennas Propag.*, vol. 42, no. 8, pp. 1106–1113, Aug. 1994.

[50] O. Norklit, P. Teal, and R. Vaughan, "Measurement and evaluation of multi-antenna handsets in indoor mobile communication," *IEEE Trans. Antennas Propag.*, vol. 49, no. 3, pp. 429–437, Mar. 2001.

[51] P. Hui, C. G. Hynes, J. van Wonterghem, and D. G. Michelson, "Measurements of correlation coefficients of closely spaced dipoles," *IEEE Int. Workshop on Antenna Tech.*, Singapore, Mar. 7-9, 2005.

[52] J. Kraus and R. J. Marhefka, *Antennas*. New York: McGraw-Hill, 2001, pp. 441–453.

[53] G. H. Brown and R. King, "High frequency models in antenna investigations," *Proc. IRE*, vol. 22, pp. 457–480, Apr. 1934.

[54] P. S. Carter, "Circuit relations in radiating systems and applications to antenna problems," *Proc. IRE*, vol. 20, no. 6, June 1932.

[55] H. A. Haus and R. B. Adler, *Circuit Theory of Linear Noise Networks*. New York: Wiley, 1959.

[56] J. W. Wallace and M. A. Jensen, "Mutual coupling in MIMO wireless systems: A rigorous network theory analysis," *IEEE Trans. Wireless Commun.*, vol. 3, no. 4, pp. 1317–1325, July 2004.

[57] S. Dossche, J. Romeu, and S. Blanch, "Representation of the envelope correlation as a function of distance and frequency for a two-port antenna system," in *IEEE AP-S Int. Symp. Dig.*, vol. 2, June 2004, pp. 1728–1731.

[58] ——, "Matching network for a spatial diversity antenna system," in *Proc. IEEE PIMRC*, vol. 1, Sept. 2004, pp. 427–431.

[59] C. G. Hynes, P. Hui, J. van Wonterghem, and D. G. Michelson, "Cross-correlation and total efficiencies of two closely spaced sleeve dipole antennas," *IEEE AP-S Int. Symp. Dig.*, Washington, DC, USA, July 3-8 2005.

[60] P. Hallbjörner, "The significance of radiation efficiencies when using S-parameters to calculate the received signal correlation from two antennas," *IEEE Antennas Wireless Propag. Lett.*, vol. 4, pp. 97–99, 2005.

[61] P. Hui and C. G. Hynes, "Correlation coefficients and radiation efficiencies of two parallel dipoles," *Asia Pacific Microwave Conference*, pp. 3031–3033, Dec. 3-7 2005.

[62] R. E. Collin, *Antennas and Radiowave Propagation*. New York: McGraw-Hill, 1985.

[63] D. Middleton, *An Introduction to Statistical Communication Theory*. New York: McGraw-Hill, 1960.

[64] I. S. Gradshteyn and I. M. Ryzhik, *Table of Integrals, Series, and Products*, 5th ed., A. Jeffery, Ed. San Diego: Academic Press, 1994.

Appendix A

Standard spherical coordinate system

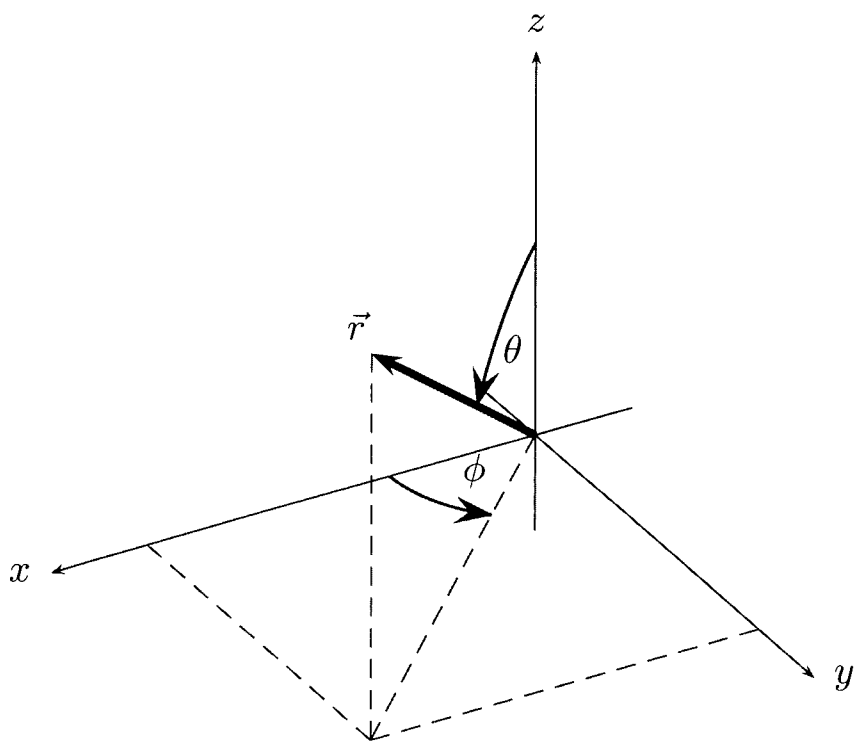

Figure A.1: The standard spherical coordinate system

Appendix B

Antenna reception and transmission relations near open-circuited parasitic antennas

This appendix details the standard proof relating the receive and transmit patterns of an antenna near scatterers. It is included in order to outline the standard assumptions made during the proof as well as give the closed form expression relating the effective antenna height and the far-field radiation pattern of an antenna.

We consider the antenna 1 is connected to a signal generator by a coaxial transmission line near the open-circuited parasitic antennas which can be viewed as a metallic scatterers[1]. When antenna 1 is first considered as a transmitting antenna the fields produced by the sources are $\mathbf{E}_1$ and $\mathbf{H}_1$. We assume two orthogonal collocated ideal Hertzian dipoles are aligned with the θ and ϕ co-ordinates located at a distance r with respect to the origin at antenna 1. The Hertzian dipoles have current elements $I_\theta \Delta l$ and $I_\phi \Delta l$, respectively, and provide the source for the fields $\mathbf{E}_2$ and $\mathbf{H}_2$. For this receive case, the open-circuit load condition at the reference plane of antenna 1 is established by placing a short circuit $\lambda/4$ away toward the generator. When antenna 1 is transmitting, the fields in the coaxial transmission line, at the reference plane, will be

$$\mathbf{E}_1 = \frac{V}{\rho \ln(b/a)} \mathbf{u}_\rho \qquad \mathbf{H}_1 = \frac{Y_{in} V}{2\pi\rho} \mathbf{u}_\phi \tag{B.1}$$

where V is the voltage, Y_{in} is the admittance looking toward the antenna, and a, b are the inner and outer radii of the coaxial transmission line conductors. Under open-circuit receiving conditions,

[1]The following is modification of the work presented in chapter 5 of [62].

there will be a current node at the reference plane and a voltage maximum equal to the open-circuit received voltage V_{oc}. The fields on the reference plane for the receiving conditions are,

$$\mathbf{E}_2 = \frac{V_{oc}}{\rho \ln(b/a)} \mathbf{u}_\rho \qquad \mathbf{H}_2 = 0 \quad . \tag{B.2}$$

The reciprocity theorem states that,

$$\oint_{\partial V} (\mathbf{E}_1 \times \mathbf{H}_2 - \mathbf{E}_1 \times \mathbf{H}_2) \cdot d\mathbf{S} = \int_V (\mathbf{E}_2 \cdot \mathbf{J}_1 - \mathbf{E}_1 \cdot \mathbf{J}_2 - \mathbf{H}_2 \cdot \mathbf{J}_{m1} + \mathbf{H}_1 \cdot \mathbf{J}_{m2})\, dV \tag{B.3}$$

where, $\mathbf{J}_i$, $\mathbf{J}_{m\,i}$ are the sources of the fields $\mathbf{E}_i$, $\mathbf{H}_i$.

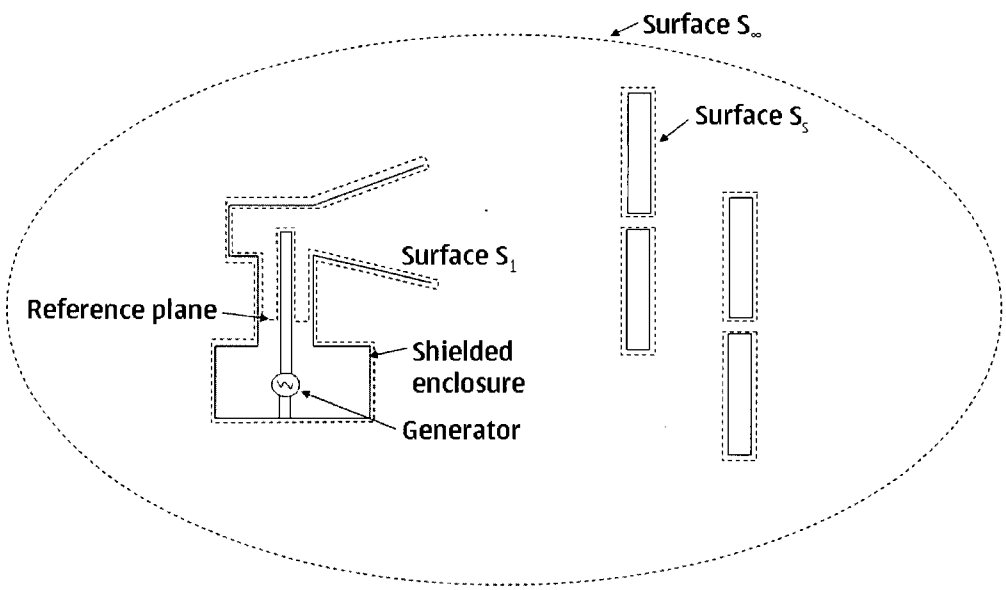

Figure B.1: Transmitting antenna configuration.

As shown in Figure B.1, the boundary of volume of the integrating in taken as S_1, S_s, and S_∞ where S_1 is around antenna 1, S_s is around the each element of open-circuited parasitic antennas, and S_∞ is a sphere of infinite radius. At infinity, the fields are spherical TEM waves for which $\mathbf{H} = Y_0\, \mathbf{u}_r \times \mathbf{E}$. Hence on S_∞ we have

$$\begin{aligned} \mathbf{E}_1 \times \mathbf{H}_2 \cdot \mathbf{u}_r - \mathbf{E}_2 \times \mathbf{H}_1 \cdot \mathbf{u}_r &= \mathbf{u}_r \times \mathbf{E}_1 \cdot \mathbf{H}_2 - \mathbf{u}_r \times \mathbf{E}_2 \cdot \mathbf{H}_1 \\ &= Z_0 \mathbf{H}_1 \cdot \mathbf{H}_2 - Z_0 \mathbf{H}_2 \cdot \mathbf{H}_1 = 0 \quad . \end{aligned} \tag{B.4}$$

For the boundaries of V which run tangent to a conductor we have,

$$\mathbf{E} = Z_s \mathbf{n} \times \mathbf{H} = \frac{1+j}{\sigma \delta_s} \mathbf{n} \times \mathbf{H} \tag{B.5}$$

where Z_s is the surface impedance of the conductor, σ is the conductivity, and δ_s is the skin depth given by

$$\delta_s = \sqrt{\frac{2}{\omega \mu_0 \sigma}} \quad . \tag{B.6}$$

Hence on the surfaces of S_s and S_1 (except on the reference plane) we have

$$\begin{aligned} \mathbf{E}_1 \times \mathbf{H}_2 \cdot \mathbf{n} - \mathbf{E}_2 \times \mathbf{H}_1 \cdot \mathbf{n} &= -\mathbf{n} \times \mathbf{H}_2 \cdot \mathbf{E}_1 + \mathbf{n} \times \mathbf{H}_1 \cdot \mathbf{E}_2 \\ &= -Z_s \mathbf{E}_2 \cdot \mathbf{E}_1 + Z_s \mathbf{E}_1 \cdot \mathbf{E}_2 = 0 \quad . \end{aligned} \tag{B.7}$$

Within the volume integral of (B.3) we have $\mathbf{J}_1 = 0$ when antenna 1 is used in the transmitting condition, while $\mathbf{J}_2$ is the current density associated with the current elements $I_\theta \Delta l$ and $I_\phi \Delta l$ when antenna 1 is in the receiving conditions.

From (B.3), we find

$$\begin{aligned} \int_a^b \int_0^{2\pi} \left[-\frac{V_{oc}}{\rho \ln(b/a)} \mathbf{u}_\rho \times \frac{V Y_{in}}{2\pi\rho} \mathbf{u}_\phi \right] (-\mathbf{u}_z \rho \, d\phi d\rho) &= V V_{oc} Y_{in} \\ &= -\int_V \mathbf{J}_2 \cdot \mathbf{E}_1 \, dV \\ &= -I_\theta \Delta l E_{1\theta} - I_\phi \Delta l E_{1\phi} \quad . \end{aligned} \tag{B.8}$$

Solving for the open-circuit voltage we find,

$$V_{oc} = -\frac{1}{I_{in}} (I_\theta \Delta l \, E_{1\theta}(\mathbf{r}) + I_\phi \Delta l \, E_{1\phi}(\mathbf{r})) \tag{B.9}$$

since $I_{in} = V Y_{in}$. The far-field electric field for a Hertzian dipole at antenna 1 is given by,

$$\mathbf{E}_2(\mathbf{r}) = -jkZ \frac{e^{-jkr}}{4\pi r} (I_\theta \Delta l \mathbf{u}_\theta + I_\phi \Delta l \mathbf{u}_\phi) \tag{B.10}$$

$$= E_\theta \mathbf{u}_\theta + E_\phi \mathbf{u}_\phi \tag{B.11}$$

where k is the wavenumber, Z is the wave impedance of the medium, and the negative sign is due to current orientations. Using (B.10) and (B.11), the open-circuit voltage (B.9) can be expressed in terms of the incident plane wave and far-field transmission patterns of the receive antenna as,

$$V_{oc} = -\frac{j4\pi r e^{jkr}}{I_{in} k Z}(E_{\theta in} E_{1\theta} + E_{\phi in} E_{1\phi}) \tag{B.12}$$

$$= \mathbf{E}_{in} \cdot \mathbf{h}_1 \tag{B.13}$$

where,

$$\mathbf{E}_1(\mathbf{r}) = \frac{jZkI_{in}e^{-jkr}}{4\pi r}\mathbf{h}_1(\Omega) \tag{B.14}$$

and I_{in} is the input current to the antenna, r is the observation point in spherical coordinates (r, θ, ϕ) with respect the origin at the antenna, $k = 2\pi/\lambda$ is the wavenumber, and $Z = \sqrt{\mu/\epsilon}$ is the intrinsic wave impedance of the medium.

Appendix C

Cross-correlation coefficient interrelations

In the following we assume all random processes involved are ergodic in the first and second order statistics. A narrow-band signal, $n(t)$, can be represented by its equivalent baseband representation, $z(t)$,

$$n(t) = Re\{z(t)e^{j\omega_c t}\} \tag{C.1}$$

where,

$$z(t) = I(t) + jQ(t) = r(t)e^{j\theta(t)} \tag{C.2}$$

$$n(t) = I(t)\cos\omega_c t - Q(t)\sin\omega_c t \tag{C.3}$$

$$= Re\{r(t)e^{j\theta(t)}e^{j\omega_c t}\} \tag{C.4}$$

$$= r(t)\cos(\omega_c t + \theta(t)) \tag{C.5}$$

and $r(t)$ is known are the signal envelope. For a narrowband signal transmitted in a Rayleigh multipath environment it can be shown [2] that the equivalent baseband signal, $z(t) = I(t) + jQ(t)$, can be modelled as a complex Gaussian process where the in-phase and quadrature-phase components satisfy:

$$\mathbb{E}[I] = \mathbb{E}[Q] = \mathbb{E}[IQ] = 0 \tag{C.6}$$

$$\mathbb{E}[I^2] = \mathbb{E}[Q^2] = \sigma^2 \quad . \tag{C.7}$$

The correlation coefficient for two baseband sample functions is given by,

$$\rho_z(\tau) = \frac{R_z(\tau)}{\sigma_1\sigma_2} = \frac{\mathbb{E}[z_1(t)z_2^*(t+\tau)]}{2\sigma^2} \tag{C.8}$$

$$= \frac{2\mathbb{E}[I_1I_2] - j2\mathbb{E}[I_1Q_2]}{2\sigma^2} \tag{C.9}$$

$$= \rho_{I_1I_2}(\tau) - j\rho_{I_1Q_2}(\tau) \quad . \tag{C.10}$$

This implies,

$$|\rho_z|^2 = \rho_{I_1I_2}^2 + \rho_{I_1Q_2}^2 \quad . \tag{C.11}$$

The correlation coefficient for two narrowband sample functions is given by,

$$\rho_n(\tau) = \frac{R_n(\tau)}{\sigma_1\sigma_2} = \frac{\mathbb{E}[n_1(t)n_2(t+\tau)]}{2\sigma^2} \tag{C.12}$$

$$= \frac{\mathbb{E}[(I_1\cos(\omega_c t) - Q_1\sin(\omega_c t))\,(I_2\cos(\omega_c(t+\tau)) - Q_2\sin(\omega_c(t+\tau)))]}{2\sigma^2} \tag{C.13}$$

$$= \frac{1}{2\sigma^2}\mathbb{E}[I_1I_2\cos(\omega_c t)\cos(\omega_c(t+\tau)) - I_1Q_2\sin(\omega_c(t+\tau))\cos(\omega_c t)$$
$$- Q_1I_2\sin(\omega_c t)\cos(\omega_c(t+\tau)) + Q_1Q_2\sin(\omega_c t)\sin(\omega_c(t+\tau))] \quad . \tag{C.14}$$

After re-expressing the sinusoid terms we find,

$$\rho_n(\tau) = \frac{1}{2\sigma^2}[\mathbb{E}[I_1I_2 - Q_1Q_2]\cos(2\omega_c t + \omega_c\tau) - \mathbb{E}[I_1Q_2 - Q_1I_2]\sin(2\omega_c t + \omega_c\tau)$$
$$+ \mathbb{E}[I_1I_2 + Q_1Q_2]\cos(\omega_c\tau) + \mathbb{E}[Q_1I_2 - I_1Q_2]\sin(\omega_c\tau)] \quad . \tag{C.15}$$

If n_1 and n_2 are jointly Wide-Sense Stationary (WSS) then,

$$\rho_n(\tau) = \frac{1}{\sigma^2}[\mathbb{E}[I_1I_2]\cos(\omega_c\tau) - \mathbb{E}[I_1Q_2]\sin(\omega_c\tau)] \tag{C.16}$$

$$= \rho_{I_1I_2}(\tau)\cos(\omega_c\tau) - \rho_{I_1Q_2}(\tau)\sin(\omega_c\tau) \quad . \tag{C.17}$$

Therefore we have established,

$$\rho_n(\tau) = Re\{\rho_z(\tau)e^{j\omega_c\tau}\} \quad . \tag{C.18}$$

Given the narrowband process, $n(t) = r(t)\cos(\omega_c t + \theta(t))$, the power correlation is given by,

$$R_{r^2} = \mathbb{E}[r_1^2 r_2^2] = \mathbb{E}\left[(I_1^2 + Q_1^2)(I_2^2 + Q_2^2)\right] = 4\sigma^4(1 + \rho_{II}^2 + \rho_{IQ}^2) \tag{C.19}$$

where we have used result for zero mean Gaussians a, b, c, d:

$$\mathbb{E}[abcd] = \mathbb{E}[ab]\mathbb{E}[cd] + \mathbb{E}[ac]\mathbb{E}[bd] + \mathbb{E}[ad]\mathbb{E}[bc] \quad . \tag{C.20}$$

Thus the power correlation coefficient is given by,

$$\rho_{r^2} = \frac{R_{r^2} - \mu_{r_1 2}\mu_{r_2 2}}{\sigma_{r^2}^2} \tag{C.21}$$

$$= \frac{4\sigma^4(1 + \rho_{II}^2 + \rho_{IQ}^2) - 4\sigma^4}{4\sigma^4} \tag{C.22}$$

$$= \rho_{II}^2 + \rho_{IQ}^2 \quad . \tag{C.23}$$

Therefore we find the power correlation coefficient is the magnitude squared complex correlation coefficient,

$$\rho_{r^2} = |\rho_z|^2 \quad . \tag{C.24}$$

Uhlenbeck [63] has shown that the envelope correlation for narrowband WSS zero-mean complex Gaussian processes is given by,

$$\rho_r(\tau) = \frac{2E(|\rho(\tau)|) - (1 - \rho^2(\tau))K(|\rho(\tau)|) - \pi/2}{2 - \pi/2} \tag{C.25}$$

where K and E are the complete elliptic integral of the first and second kind respectively and ρ is the complex Gaussian correlation coefficient. From this expression, and seen in the figure below, we find:

$$\rho_r \approx |\rho_z|^2 \tag{C.26}$$

within 10 per cent maximum relative error.

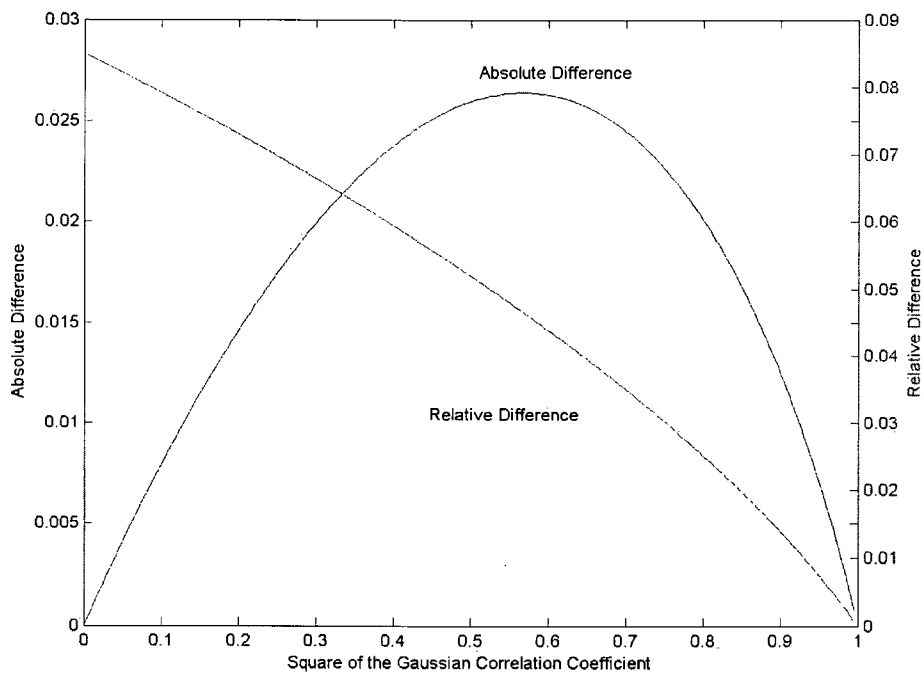

Figure C.1: The absolute error, $|\rho_z|^2 - \rho_r$, and the relative error, $(|\rho_z|^2 - \rho_r)/|\rho_z|^2$, between the magnitude squared complex correlation coefficient and the envelope correlation coefficient for narrowband normal noise.

Appendix D

CST Microwave Studio Dipole models

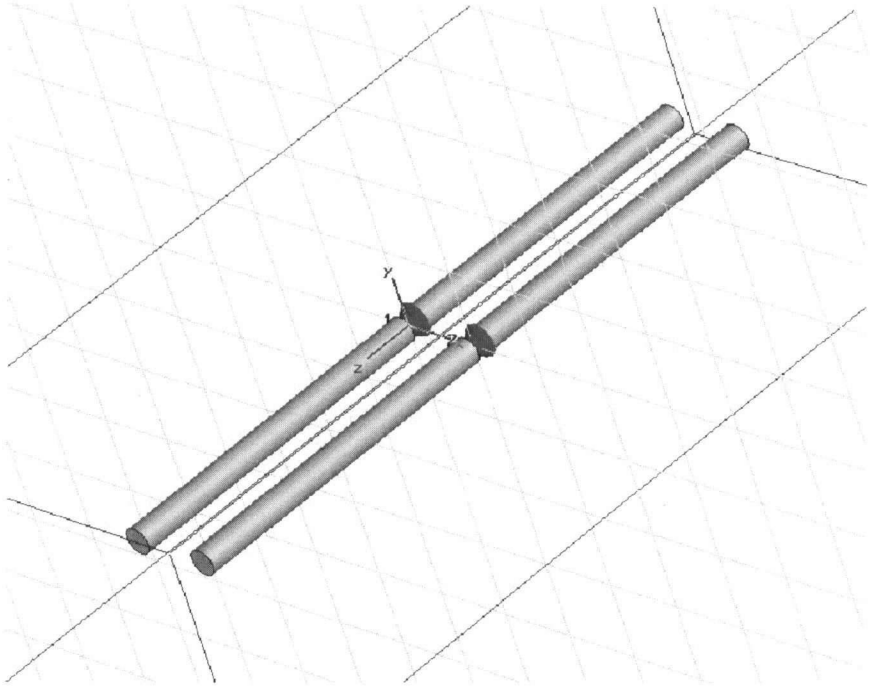

Figure D.1: CST Microwave Studio cylinder dipole model for radius of $\lambda/100$.

Table D.1: Parameter setting for the cylinder dipole CST model with radius = $\lambda/100$.

Parameter	Setting
Lines per wavelength	50
Refinement at PEC	15
Accuracy	-50dB
Radius	$\lambda/100$
Total length	$\lambda/2$
Centre gap length	$\lambda/100$
λ	33.9 cm

Table D.2: Parameter setting for the cylinder dipole CST model with radius = $\lambda/1000$.

Parameter	Setting
Lines per wavelength	50
Refinement at PEC	50
Accuracy	-60dB
Radius	$\lambda/1000$
Total length	$\lambda/2$
Centre gap length	$\lambda/100$
λ	33.9 cm

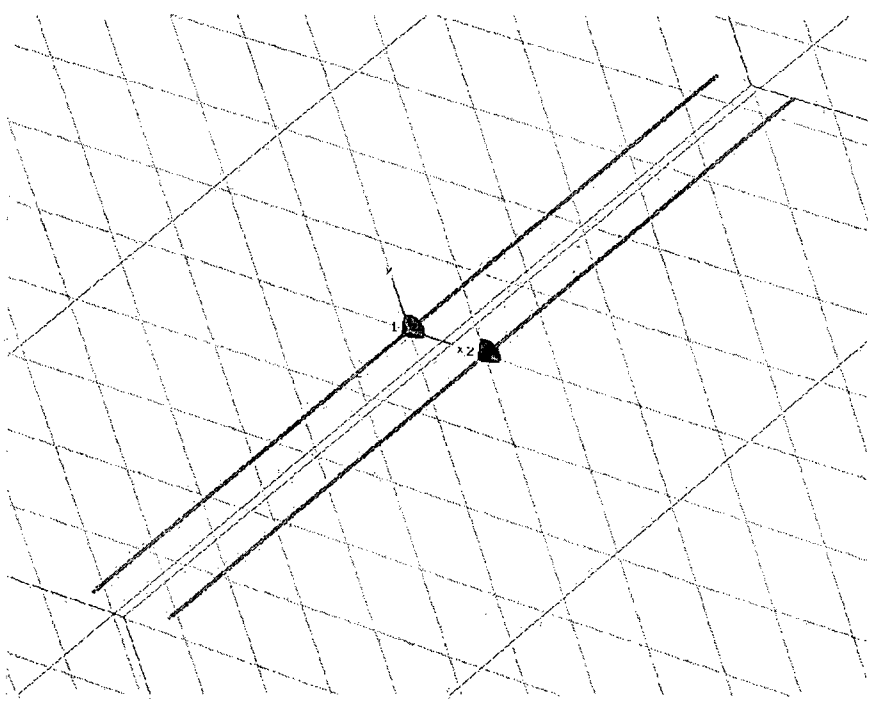

Figure D.2: CST Microwave Studio cylinder dipole model for radius of $\lambda/1000$.

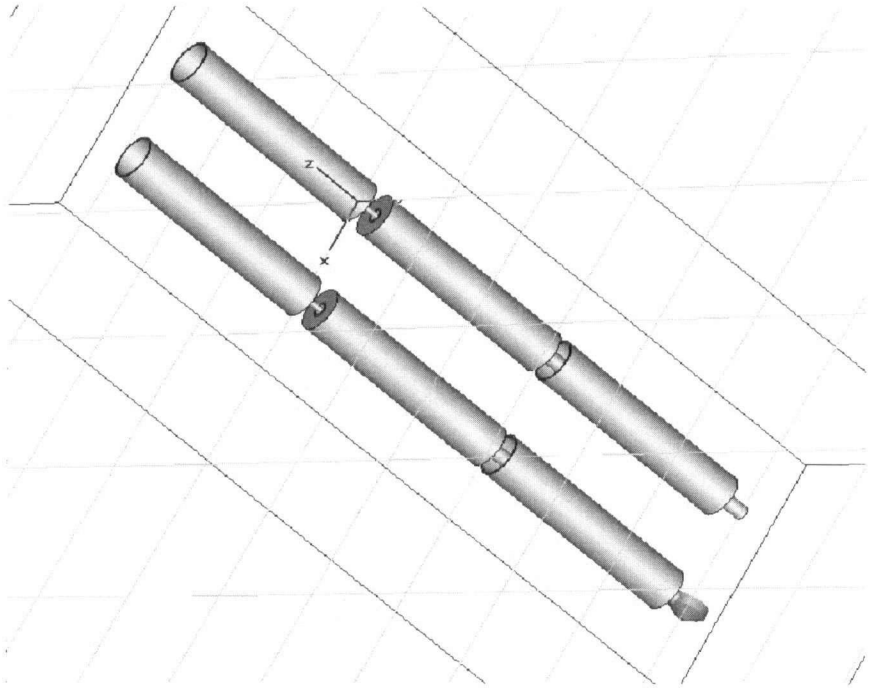

Figure D.3: CST Microwave Studio Sleeve dipole model (view 1.)

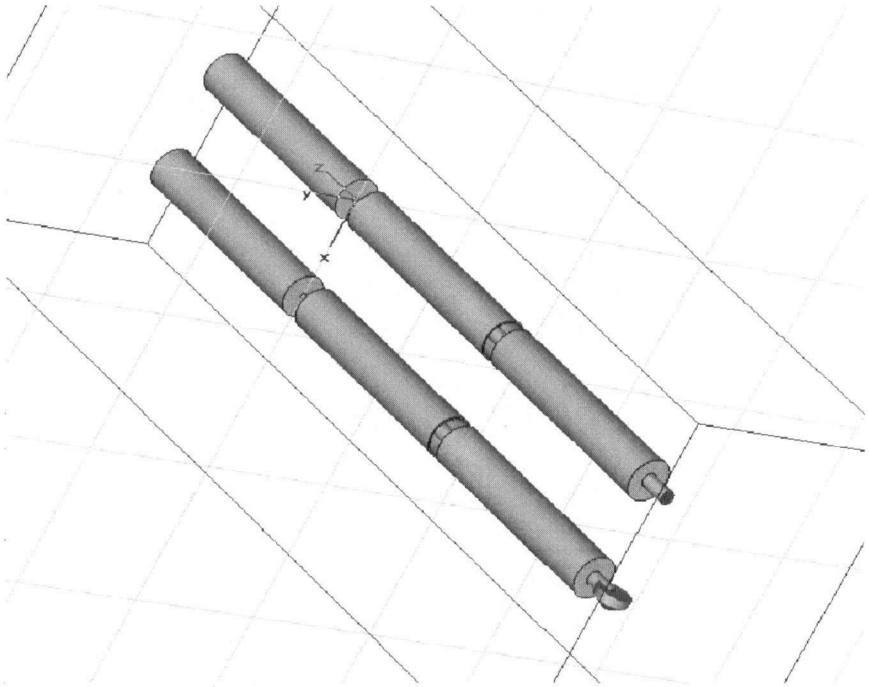

Figure D.4: CST Microwave Studio Sleeve dipole model (view 2.)

Appendix E

Self and mutual impedances for simulated cylinder $\lambda/2$ dipole antennas

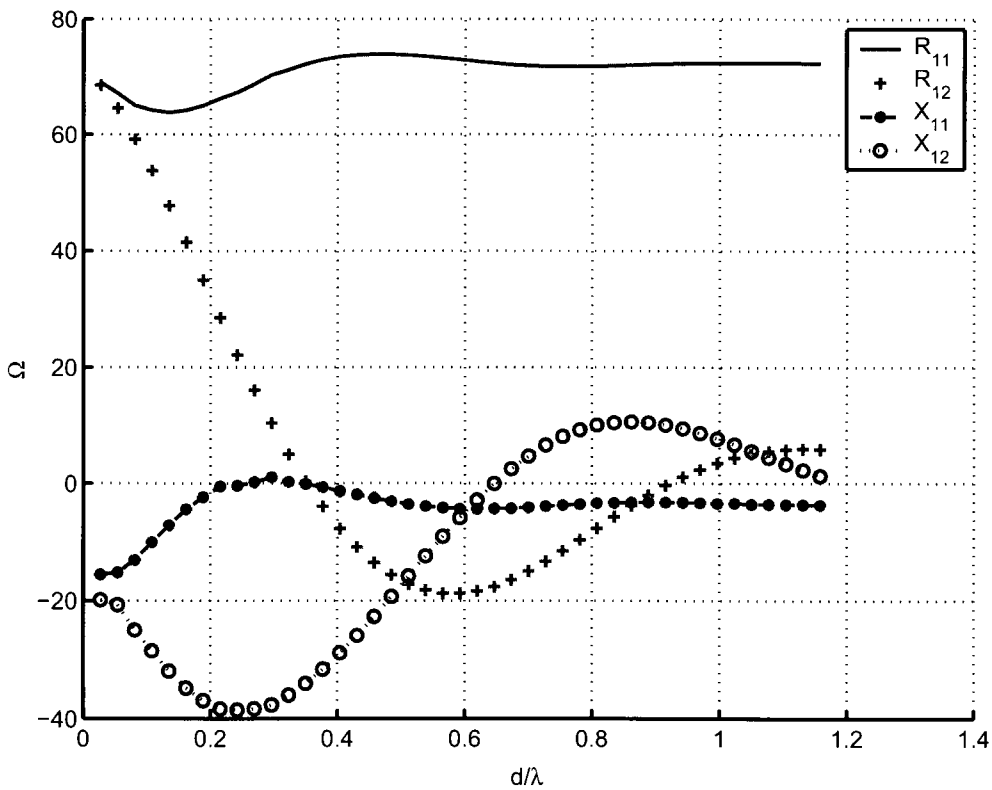

Figure E.1: Self and mutual impedances of simulated cylinder dipoles ($r = \lambda/100$, $\lambda = 33.9cm$) as a function of separation distance; measured at 808MHz.

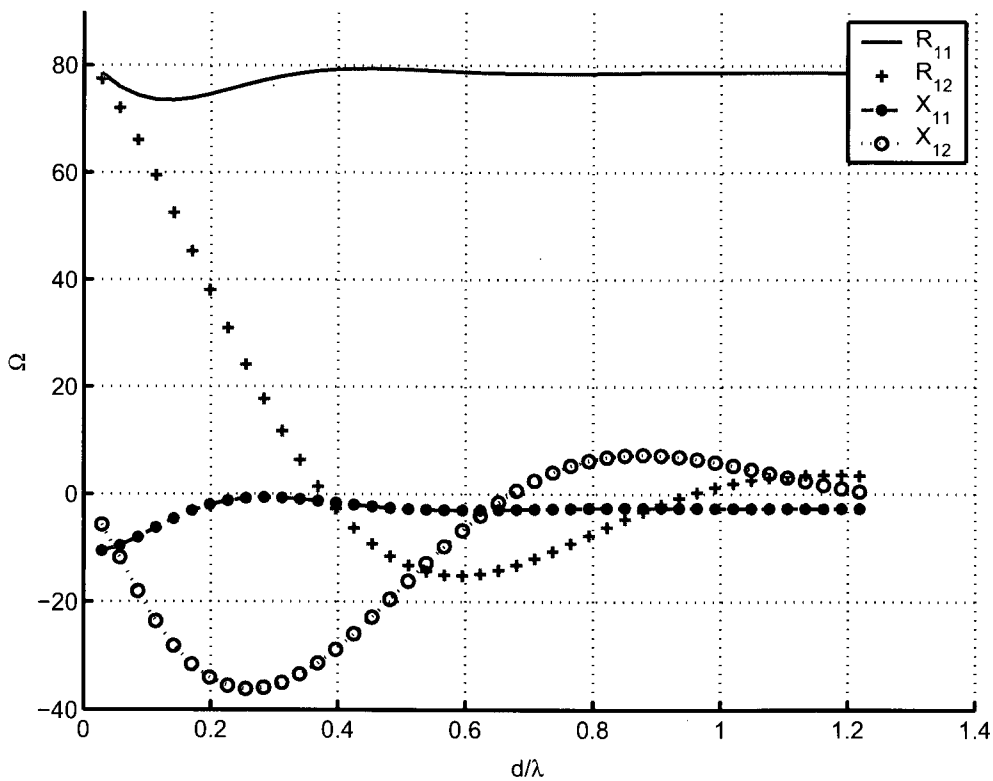

Figure E.2: Self and mutual impedances of simulated cylinder dipoles ($r = \lambda/1000$, $\lambda = 33.9cm$) as a function of separation distance; measured at 850MHz.

Appendix F

Antenna matching and coupling for the simulated cylinder dipole antennas

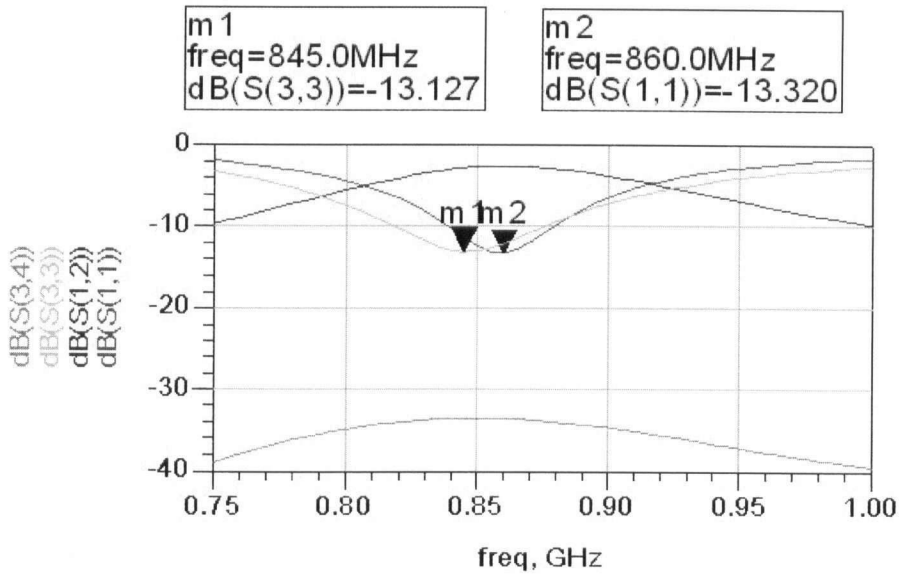

Figure F.1: Antenna matching and coupling frequency off-set extremes for the simulated cylinder dipoles ($r = \lambda/1000$, $\lambda = 33.9cm$). The measurements sets shown for ports 1 and 2 were when the antennas (attached to ports 1 and 2, respectively) had the smallest separation distance ($\approx 0.03\lambda$). The measurements sets shown for ports 3 and 4 were when the antennas (attached to ports 3 and 4, respectively) had the largest separation distance ($\approx 1.2\lambda$). The frequency 850 MHz was used for the correlation calculations.

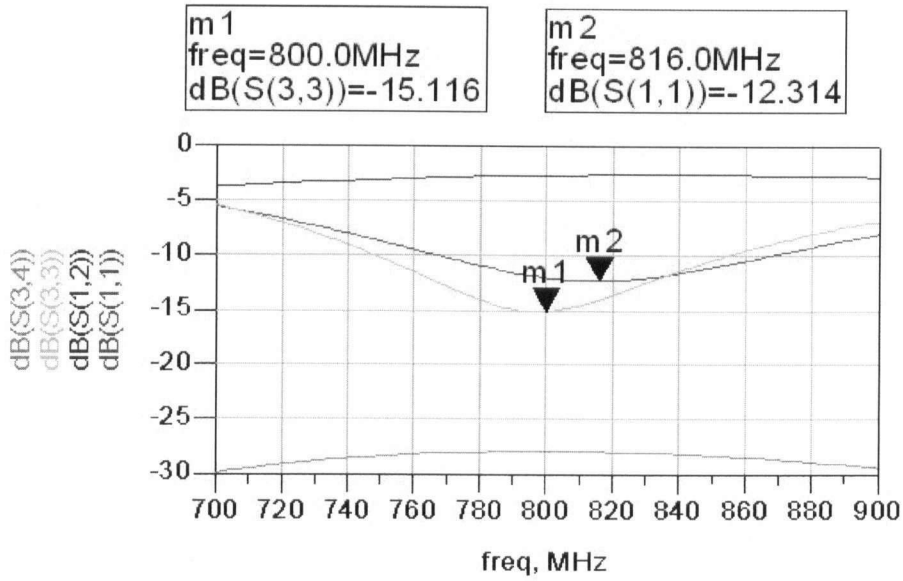

Figure F.2: Antenna matching and coupling frequency off-set extremes for the simulated cylinder dipoles ($r = \lambda/100$, $\lambda = 33.9cm$). The measurements sets shown for ports 1 and 2 were when the antennas (attached to ports 1 and 2, respectively) had the smallest separation distance ($\approx 0.03\lambda$). The measurements sets shown for ports 3 and 4 were when the antennas (attached to ports 3 and 4, respectively) had the largest separation distance ($\approx 1.1\lambda$). The frequency 808 MHz was used for the correlation calculations.

Appendix G

Mutual impedance estimate normalized by the antenna self-impedance when not in isolation

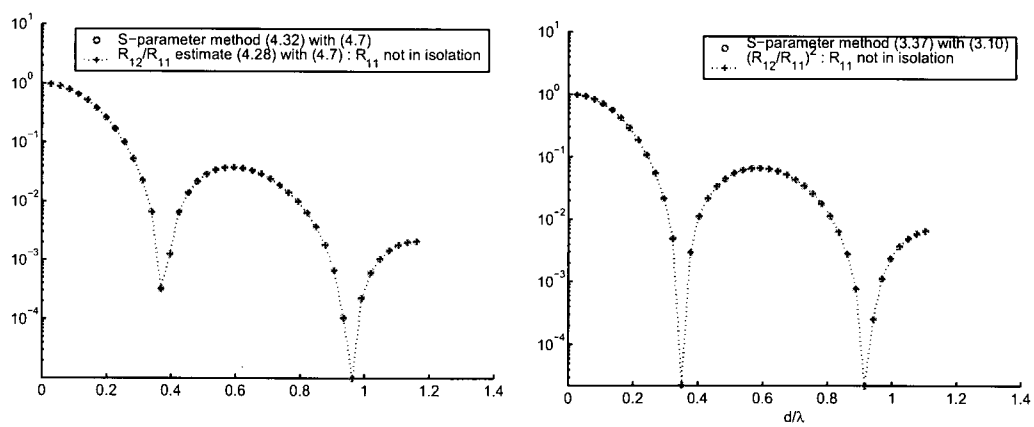

(a) Simulated $\lambda/1000$ dipoles (850 MHz)

(b) Simulated $\lambda/100$ dipoles (808 MHz)

Figure G.1: CST simulation results showing equivalence of open-circuit correlation circuit-parameters estimates (normalized mutual resistance and S-parameter estimate methods) for two dipoles. Normalization of mutual resistance is done by self-impedance with the other antenna present.

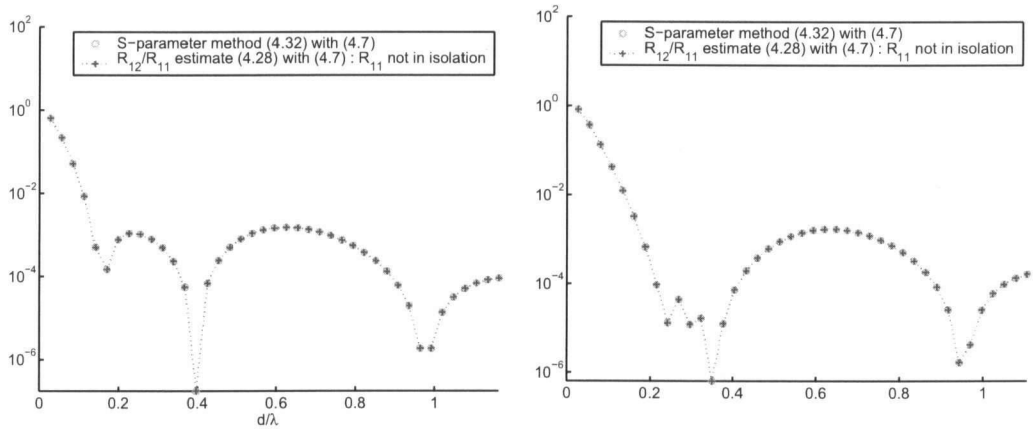

(a) Simulated $\lambda/1000$ dipoles (850 MHz)

(b) Simulated $\lambda/100$ dipoles (808 MHz)

Figure G.2: CST simulation results showing equivalence of load-voltage correlation circuit-parameters estimates (normalized mutual resistance and S-parameter estimate methods) for two dipoles. Normalization of mutual resistance is done by self-impedance with the other antenna present.

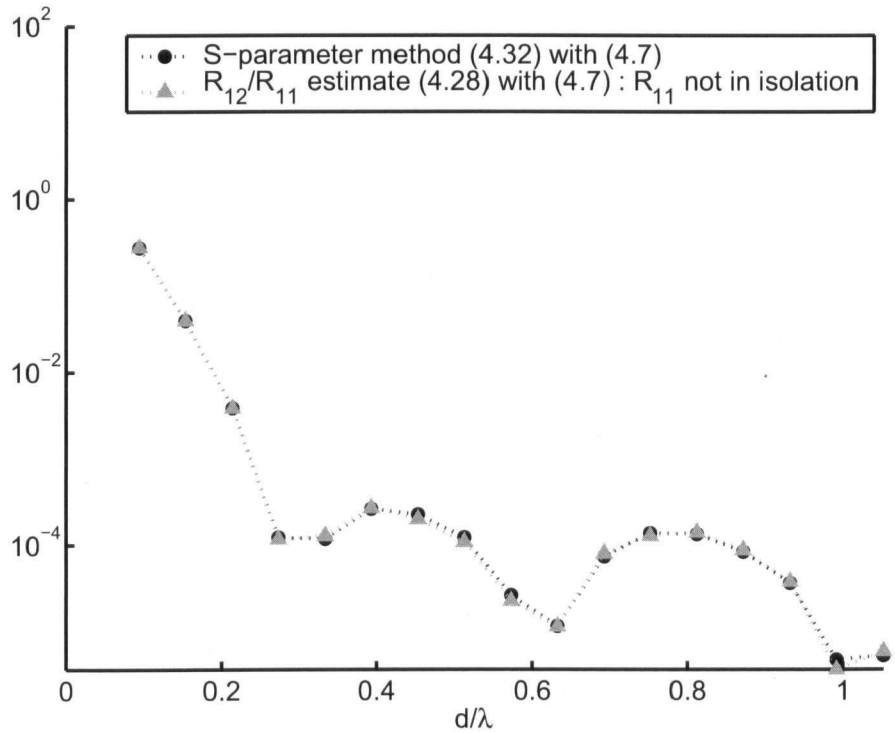

Figure G.3: Load voltage cross-correlation coefficient predictions methods obtained from measurement of Satimo sleeve dipoles for 50 Ω load termination. Note that normalized mutual resistance and S-parameter estimates match exactly.

Appendix H

Effect of evaluating the correlation estimates for different frequencies

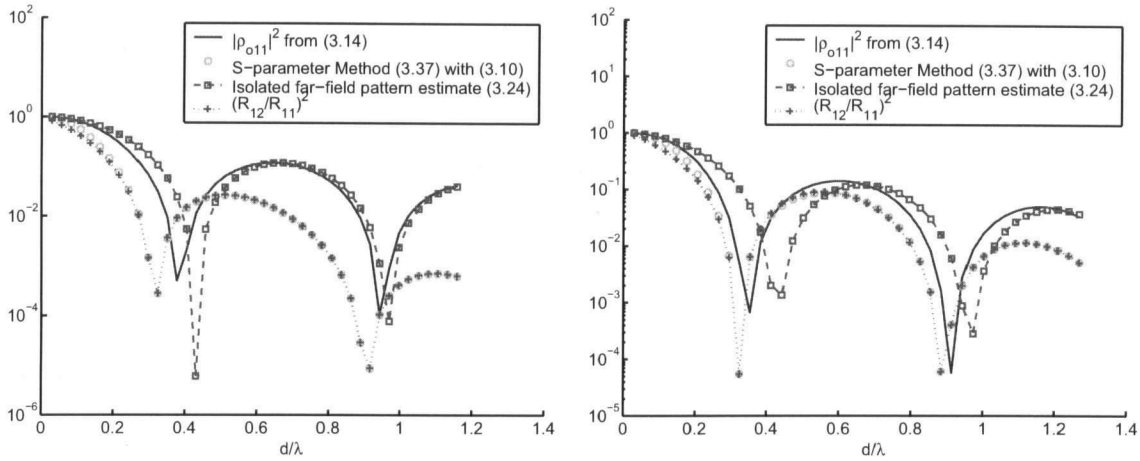

(a) $\lambda/100$ dipole calculated at 808 MHz.

(b) $\lambda/100$ dipole calculated at 884 MHz.

Figure H.1: Effect of evaluating the open-circuit voltage correlation coefficient estimates for different frequencies (808 MHz and 884 MHz) for $r = \lambda/100$ dipoles. Results based on numerical simulations using CST (log scale.)

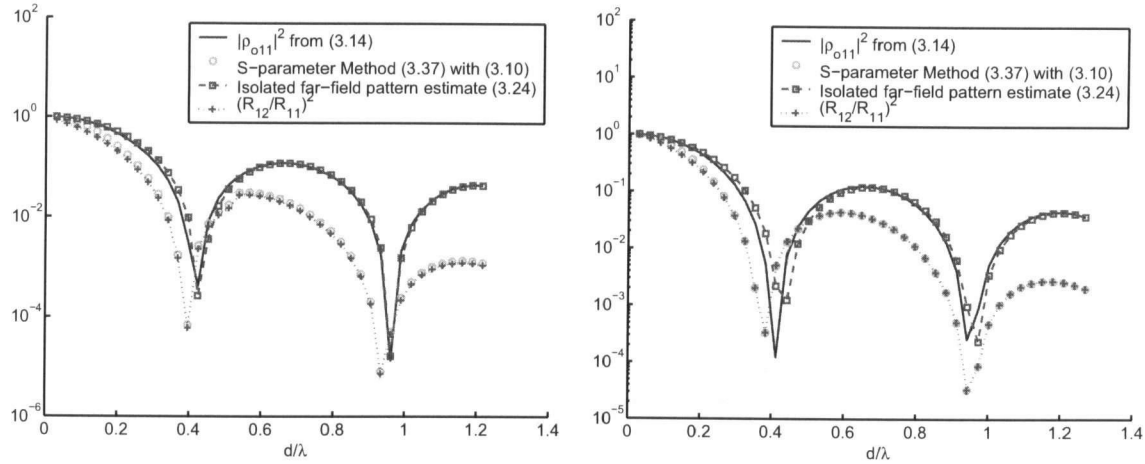

(a) $\lambda/1000$ dipole calculated at 850 MHz.

(b) $\lambda/1000$ dipole calculated at 884 MHz.

Figure H.2: Effect of evaluating the open-circuit voltage correlation coefficient estimates for different frequencies (850 MHz and 884 MHz) for $r = \lambda/1000$ dipoles. Results based on numerical simulations using CST (log scale.)

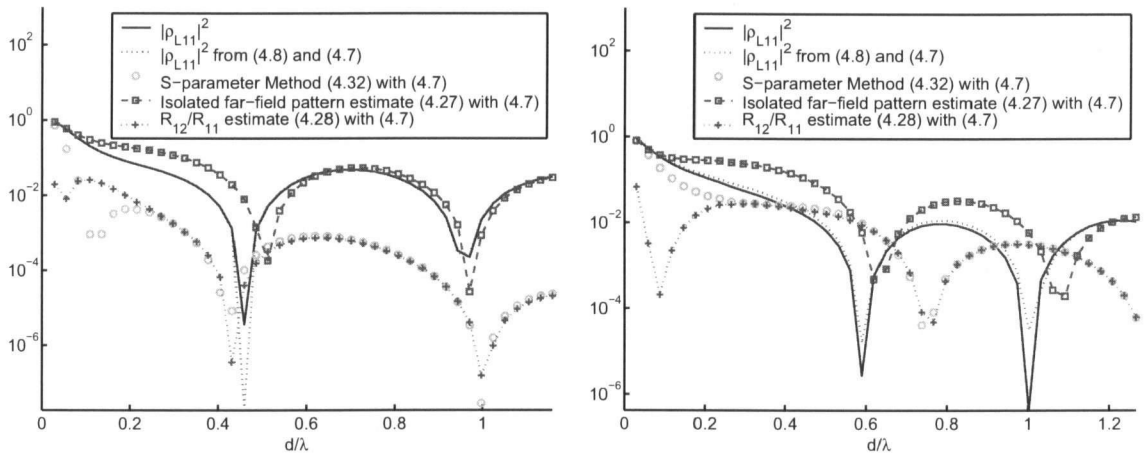

(a) $\lambda/100$ dipole calculated at 808 MHz.

(b) $\lambda/100$ dipole calculated at 884 MHz.

Figure H.3: Effect of evaluating the load voltage correlation coefficient estimates for different frequencies (808 MHz and 884 MHz) for $r = \lambda/100$ dipoles. Results based on numerical simulations using CST (log scale.) The circuit-parameter estimates are seen to vary greatly as a function of evaluation frequency; in contrast to the field pattern correlations.

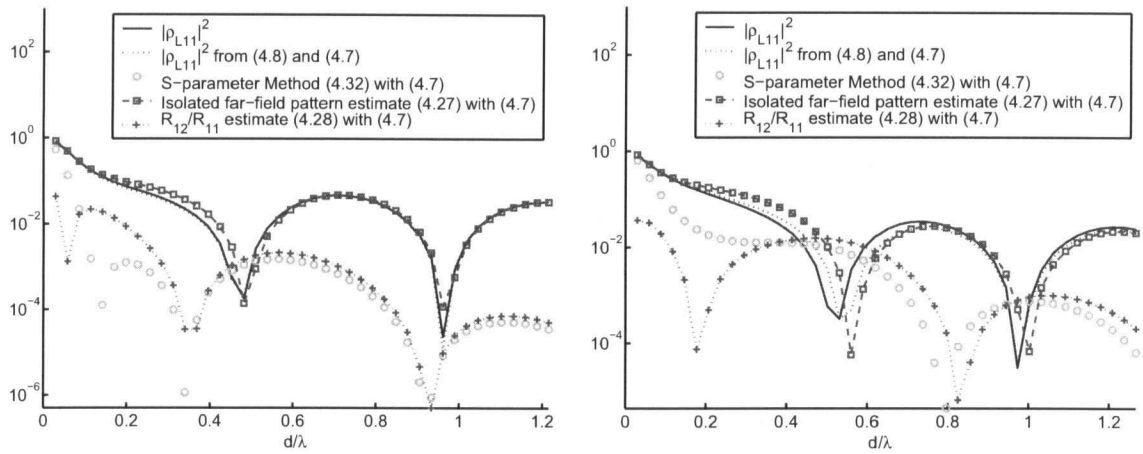

(a) $\lambda/1000$ dipole calculated at 850 MHz.

(b) $\lambda/1000$ dipole calculated at 884 MHz.

Figure H.4: Effect of evaluating the load voltage correlation coefficient estimates for different frequencies (850 MHz and 884 MHz) for $r = \lambda/1000$ dipoles. Results based on numerical simulations using CST (log scale.) The circuit-parameter estimates are seen to vary greatly as a function of evaluation frequency; in contrast to the field pattern correlations.

Appendix I

Evaluation of Hertzian dipole auto-correlation integral

In order to obtain (3.57), the auto-correlation of a Hertzian dipole in a Mobile Prototype Scenario, it is necessary to evaluate the following integral,

$$A = \int_0^{\pi} \sin^3\theta J_0(kd\sin\theta)\, d\theta \quad . \tag{I.1}$$

From the trigonometric identity,

$$\sin^3\theta = \frac{3\sin\theta - \sin 3\theta}{4} \quad . \tag{I.2}$$

Equation (I.1) becomes,

$$A = \frac{1}{4}\left[3\int_0^{\pi} \sin\theta J_0(kd\sin\theta)\, d\theta - \int_0^{\pi} \sin 3\theta J_0(kd\sin\theta)\, d\theta\right] \quad . \tag{I.3}$$

From the integral relations [64],

$$\int_0^{\pi} \sin(x) J_0(2a\sin x)\, dx = \pi J_{-1/2}(a) J_{1/2}(a) \tag{I.4}$$

$$\int_0^{\pi} \sin(3x) J_0(2a\sin x)\, dx = -\pi J_{-3/2}(a) J_{3/2}(a) \quad . \tag{I.5}$$

Equation (I.1) becomes,

$$A = \frac{\pi}{4}\left[3J_{-1/2}(kd/2)J_{1/2}(kd/2) + J_{-3/2}(kd/2)J_{3/2}(kd/2)\right] \quad . \tag{I.6}$$

Using the Bessel function relations,

$$J_{1/2}(a) = \sqrt{\frac{2}{\pi a}} \sin a \tag{I.7}$$

$$J_{-1/2}(a) = \sqrt{\frac{2}{\pi a}} \cos a \tag{I.8}$$

$$J_{3/2}(a) = \sqrt{\frac{2}{\pi a}} \left(\frac{\sin a}{a} - \cos a \right) \tag{I.9}$$

$$J_{-3/2}(a) = -\sqrt{\frac{2}{\pi a}} \left(\sin a + \frac{\cos a}{a} \right) \quad . \tag{I.10}$$

Equation (I.1) simplifies to,

$$A = \frac{3}{2kd} \left[\sin(kd) + \frac{\cos(kd)}{kd} - \frac{\sin(kd)}{(kd)^2} \right] \quad . \tag{I.11}$$

Appendix J

Antenna arrangement for experimental measurements

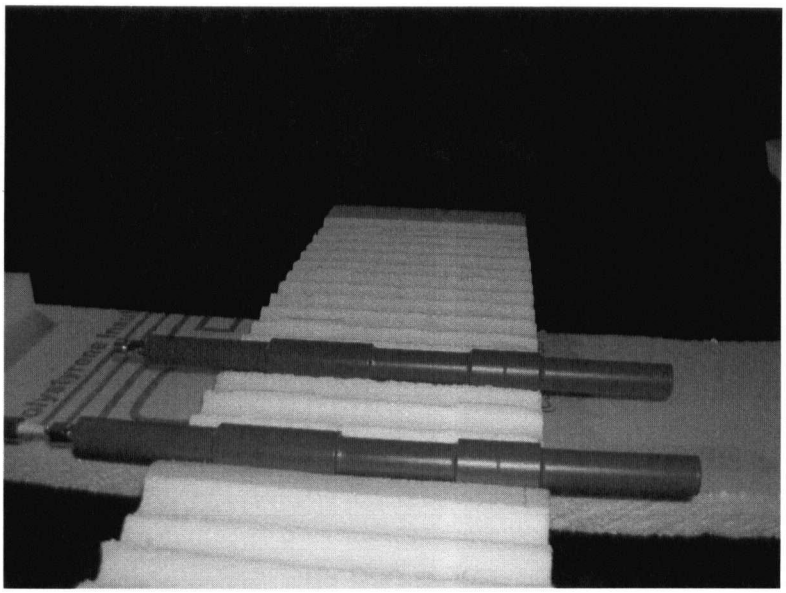

Figure J.1: Typical arrangement of the 945 MHz Satimo sleeve dipoles (without top cover) during experimental measurements.

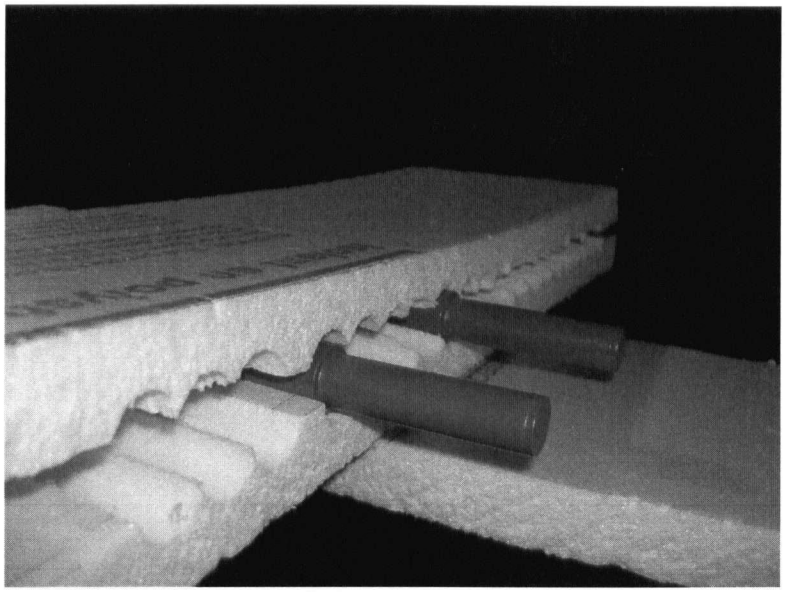

Figure J.2: Typical arrangement of the 945 MHz Satimo sleeve dipoles (with top cover) during experimental measurements.

Appendix K

Measured self and mutual impedances for Satimo sleeve dipole antennas

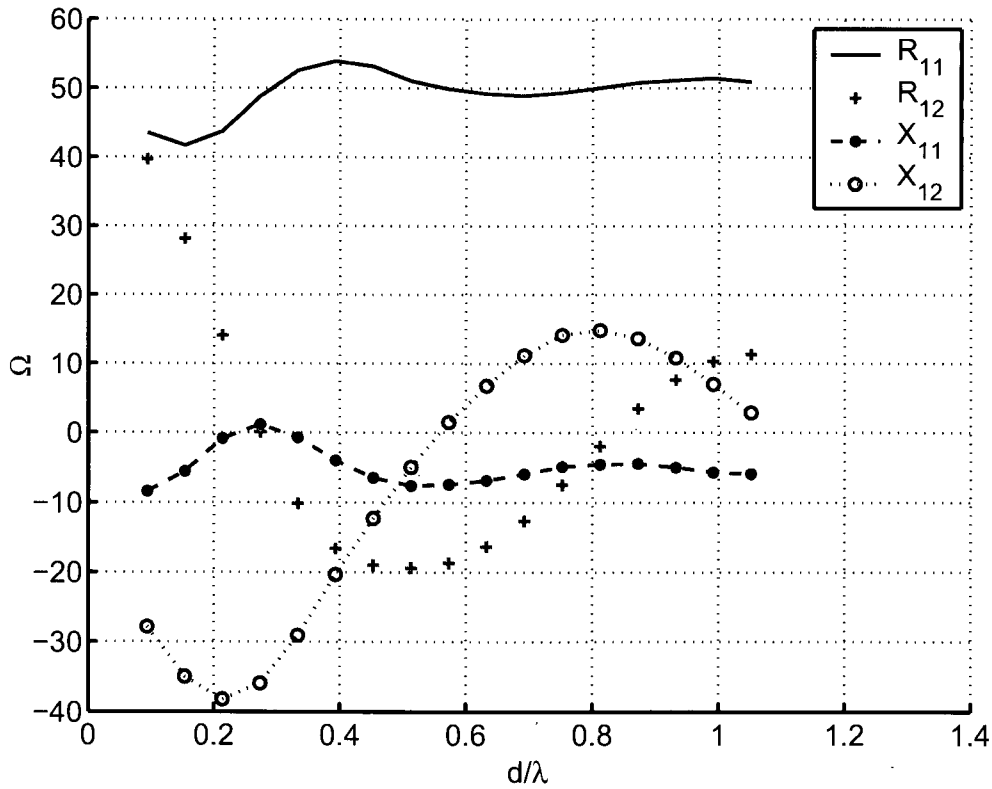

Figure K.1: Measured self and mutual impedances of Satimo (945 MHz centre frequency) sleeve dipoles as a function of separation distance.

Appendix L

H-plane pattern variations as a function of separation distance for closely spaced dipoles

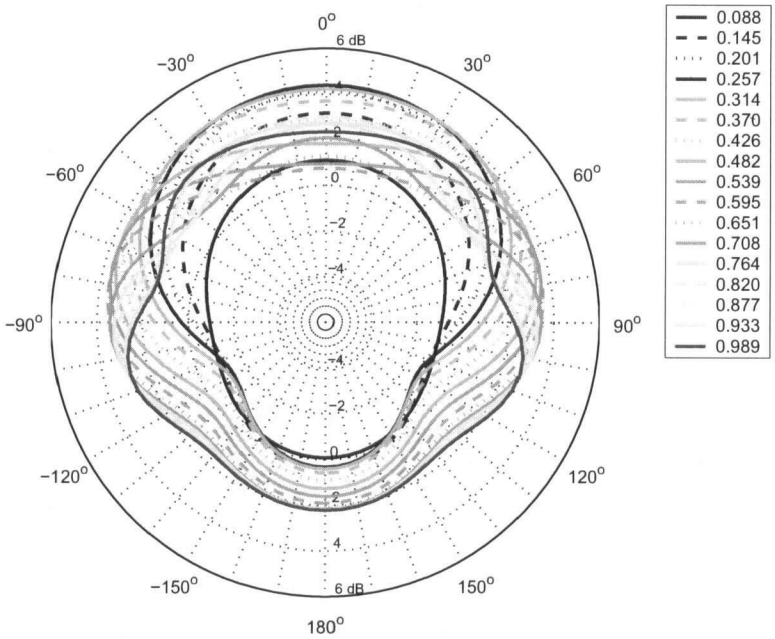

Figure L.1: The H-plane pattern variations as a function of separation distance (d/λ) for closely spaced dipoles simulated with CST Microwave Studio